Telecommunications and Information Technology

Alberto Paradisi
Alan Godoy Souza Mello
Fabrício Lira Figueiredo
Rafael Carvalho Figueiredo *Editors*

Cognitive Technologies

CRC Press
Springer

Telecommunications and Information Technology

Series editor

Alberto Paradisi, Campinas, Brazil

More information about this series at http://www.springer.com/series/14176

Alberto Paradisi
Alan Godoy Souza Mello
Fabrício Lira Figueiredo
Rafael Carvalho Figueiredo
Editors

Cognitive Technologies

Springer

Editors
Alberto Paradisi
Chief Research and Development Officer
CPqD
Campinas, São Paulo
Brazil

Alan Godoy Souza Mello
Cognitive Computing Division
CPqD
Campinas, São Paulo
Brazil

Fabrício Lira Figueiredo
Wireless Technologies Division
CPqD
Campinas, São Paulo
Brazil

Rafael Carvalho Figueiredo
Optical Technologies Division
CPqD
Campinas, São Paulo
Brazil

ISSN 2365-564X ISSN 2365-5658 (electronic)
Telecommunications and Information Technology
ISBN 978-3-319-53752-8 ISBN 978-3-319-53753-5 (eBook)
DOI 10.1007/978-3-319-53753-5

Library of Congress Control Number: 2017933557

Printed on acid-free paper

This Springer imprint is published by Springer Nature
The registered company is Springer International Publishing AG
The registered company address is: Gewerbestrasse 11, 6330 Cham, Switzerland

Preface

"Essentially, all models are wrong, but some are useful" (George E. P. Box, 1978)

Model: This is probably the word one will hear the most when talking about cognitive technologies. After all, much of cognition—natural or artificial—is concerned with building more suitable models and finding the structures that better capture the most relevant aspects of reality. In present days, deep neural networks are the "hottest models" in artificial intelligence (AI), driving some of the most revolutionary technologies currently being built. A few years ago, statistical models were the dominant cognitive technique, just as rule-based models were before them.

Model design is a key issue not only for cognitive technologies but also for science and engineering in general. Good models are able to represent relevant characteristics of a complex phenomenon into an abstract representation, either enabling a better comprehension of a target system or producing testable predictions that can be used to validate a theory. With an accurate model at hand, for instance, one can control a system by forecasting responses to different inputs and, thus, determining the set of inputs that can take the system closest to the desired state.

There are many different types of models. Besides the widely used mathematical and statistical formulations in the cognitive technology context, other examples are textual descriptions and scale models. One feature, however, is common to all models: all of them miss some aspects of the systems they are intended to model, due to simplifications and idealizations, ignoring characteristics of the real-world in the name of treatability. This occurs when one overlooks particularities and considers, for instance, that all electrical batteries of a given type produced by a factory have exactly the same behavior observed in a set of prototypes thoroughly evaluated in a laboratory test. We also simplify reality when we avoid considering that users may interact in a very specific way with a device such as a smartphone, designing a user experience that is adequate for an idealized typical individual.

Some of these simplifications and mismatches are introduced because we lack, at design time, the data or the knowledge needed to create more accurate models or because it would be prohibitively laborious to create models that capture more aspects of the system we intend to represent. Imagine how costly the production of

a wireless router would be if all possible scenarios of the radio spectrum occupation that can be faced by this router were considered, in order to define the best answer for each case.

Until recently, a new system design would only require a theory that roughly explained its behavior and how it was used. Such approach, however, is no longer sufficient. On the one hand, the widespread adoption of technologies increases the unpredictability of their usage and the ever-faster pace of technological and social changes makes models easily outdated. On the other hand, a relentless drive for efficiency and accuracy, as well as the design of applications that tackle more complex tasks, some of which we lack a complete understanding, such as language and image processing, demand that engineers look for new types of models.

How should we respond to this reality? There is where cognitive technologies come in.

Cognitive technologies—especially those linked to machine learning—refer to adaptiveness as a crucial feature for developing better systems, reducing their reliance on the knowledge available at design time. The cognitive approach prescribes that, if we fail to determine a priori how a system will behave and the environment it will meet, such systems should be able to gather data and autonomously adapt to the observed reality, anticipating future states whenever possible. With an increasing number of sensors deployed around the world, meaning that each individual produces, on average, more data than an entire city the size of São Paulo used to produce 25 years ago, data-oriented techniques are especially convenient. Furthermore, the growth in the amount of data and applications requires dynamism and heterogeneity of communication networks. In this sense, cognitive technologies can be applied to current optical and wireless networks, which should be aware of current conditions and have the ability to respond autonomously in order to dynamically reconfigure the network, providing efficient allocation of the spectrum and improving end-to-end performance.

This book presents a wide range of applications, within the cognitive technology context, that are currently being developed at Fundação CPqD: from classical statistical methods and machine learning techniques to cognitive networks and adaptive control.

Part I texts are focused on classical applications of cognitive technologies, such as speech processing and statistical models. In chapter "Exploring Convolutional Neural Networks for Voice Activity Detection", authors employed Convolutional Neural Networks (CNN), a technique initially designed to solve problems in the computer vision scenario, to partition an input audio into parts that contain voice and parts that only have background noise. To enable such transposition of methods, each audio is converted into a spectrogram and then processed as an image. The methodology was tested on a dataset containing 600 hours of audio at different noise scenarios, outperforming state-of-the-art techniques. Chapter "Distributed Averaged Perceptron for Brazilian Portuguese Part-of-Speech Tagging" assesses the application of Averaged Perceptron to grammatically label words in a sentence in Brazilian Portuguese. This labeling task, known as Part-of-Speech Tagging, is common to problems of natural language processing and speech synthesis and recognition. The

technique was evaluated on a corpus consisting of newspaper texts with approximately one million words, 50,000 sentences and 30 different grammatical labels, surpassing the previous state-of-the-art performance for purely supervised classification of Brazilian Portuguese. Chapters "Method for Estimating Confidence Intervals for DEA Efficiency Models Using Regression Models" and "Considerations about Adding Aggregated Variables to the DEA Model" discuss extensions to the Data Envelopment Analysis (DEA), a mathematical technique to compare the performance and evaluate the efficiency of organizations like business companies, schools, and hospitals. In their first work, the authors used a technique known as bootstrapping to estimate confidence intervals for the computed efficiencies. In their second paper, the authors tackled the problem of adequately estimating efficiencies with insufficient data, reducing information loss through the aggregation of variables.

Part II is devoted to the study of cognitive technologies applied to wireless networks, which can be adapted for dynamically optimizing overall system performance and autonomously adapt to the radiofrequency operation environment changes. Chapter "Cognitive Radio Networks" introduces the concept of cognitive radio and presents a framework comprising spectrum management functionalities for addressing typical white space scenarios. In chapter "5G Cognitive Wireless Mesh Network without Common Control Channel", Collaborative Cognitive Mesh Networks (CCMN) are presented as a potential 5G network technology, since they provide high flexibility and efficient spectrum usage. Besides regular cognitive radio mechanisms, such as spectrum sensing, the common control channel and the Multi-Channel-Single Interface Manager (MC-SIM) algorithm enable dynamic channel allocation and maximize spectrum usage. Based on empirical testing, the MC-SIM algorithm provided a throughput enhancement of up to 30% compared to that of a regular system. Chapter "4G/LTE Networks for Mission-Critical Operations: A Cognitive Radio Approach" proposes two innovative strategies based on cognitive radio technology for preventing jamming attacks in 4G/LTE networks, aiming at attending requirements of military and public safety applications. The algorithm performance evaluation is based on Cell Frequency Reconfiguration and Frequency Hopping strategies, considering video streaming service in different jamming scenarios. Extending the scope to radiating elements of a radio system, chapter "A Fast and Efficient 3D Beamforming Algorithm for Cognitive Radio Networks" presents a fast, flexible and accurate algorithm to enable 3D beamforming for cognitive radio networks. Such algorithm mitigates the interference between primary and secondary users in cognitive radio networks, thus reducing the power required per connection and increasing system capacity. The radiation pattern of the algorithm was compared to the results obtained from an RF simulation tool, and the absolute difference was found to be less than −30 dB, which has proven to be an excellent accuracy level.

Part III addresses cognitive technologies applied to optical communications networks, with cognitive approaches employed to reconfigure physical network devices, namely the Erbium-doped Fiber Amplifiers (EDFA)—currently the most deployed device aimed at amplifying the transmitted signal in optical links. Chapter

"Simulation-Based Optimization of OSNR on Under-Monitored EDFA-Based Optical Links Using Backpropagation Correction" employs cognitive technologies aiming at optical signal-to-noise ratio (OSNR) optimization by predicting gain behavior of EDFAs. In particular, a feedback assisted network simulation applying backpropagation error correction technique is proposed and validated on in-lab real network tests with different traffic loads. Meanwhile, chapter "Optical Amplifier Cognitive Gain Adjustment Methodology for Dynamic and Realistic Networks" explores a cognitive methodology to adjust EDFA operating points based on Case-Based Reasoning (CBR). The methodology was validated through simulations in different topology networks and then compared with other approaches.

We would like to thank Alan Caio Rodrigues Marques, André Luiz Verucci da Cunha, André Ricardo Gonçalves, Guilherme Adriano Folego, Jacklyn Dias Reis, Marcos Medeiros Raimundo, and Maria Lucía del Rosario Castro Jorge for their valuable contribution to the review process of this book.

Campinas, Brazil

Alberto Paradisi
Alan Godoy Souza Mello
Fabrício Lira Figueiredo
Rafael Carvalho Figueiredo

Contents

Part I
Classical Applications of Cognitive Technologies

Considerations About Adding Aggregated Variables to the DEA Model

Filipe Giovani Bonin Bisoffi, Renata Maria Ganselli Stevaux, Victor Henrique Duarte de Oliveira and Sérgio Ricardo Barbosa

Abstract Even in a scenario where Big Data has increasingly become a part of company structure, it is not uncommon to come across statistical or mathematical analysis processes lacking sufficient available observations to consider all the business variables of interest. As a consequence, it affects, in different levels, all analytic methods whether statistical or mathematical. Specifically in the case of the benchmarking model known as DEA (Data Envelopment Analysis), the convergence of involved algorithms is directly dependent on the relation between the quantity of observations and the quantity of variable considered. Any attempt to circumvent the conditions imposed by these methodologies will result in loss of information. The scope of this study is to propose an alternative method to deal with this problem when the DEA model is applied and minimize information loss.

Keywords DEA · Confidence interval · Nonparametric regression analysis

1 Introduction

When applying a statistical or mathematical model to a data set, every analyst must ponder the ratio between the number of observations and the number of variables of interest available to perform the analysis, that is, the higher the number of variables is more data is needed. Each method will be subject to impacts of varied degrees of intensity when this ratio is not favorable. For example, a linear regression model needs at least k observations to estimate $k - 1$ parameters; otherwise, the matrices used to estimate the parameters become singular [1].

F.G.B. Bisoffi (✉) · R.M.G. Stevaux
Decision Management Support & Applications Department, CPqD Research and Development Center in Telecommunications, Campinas, Brazil
e-mail: fbisoffi@cpqd.com.br

V.H.D. de Oliveira · S.R. Barbosa
CEMIG Distribuição S.A., Belo Horizonte, Brazil
e-mail: srb@cemig.com.br

A. Paradisi et al. (eds.), *Cognitive Technologies*, Telecommunications and Information Technology, DOI 10.1007/978-3-319-53753-5_1

This is also true for *benchmarking* models, used to compare the performance and estimate efficiency of Decision Making Units (DMUs), as firms, schools or hospitals. For the DEA model [2], for instance, literature indicates that the quantity of compared DMUs should be from two to three times the sum of the number of inputs, plus the number of outputs considered in the model [3]. There is a number of methods to reduce variables in the DEA model, one of which is using stepwise algorithms, as described by Jenkins and Anderson [4] and by Senra [5]. These methods are designed to select variables in such a way as to minimize information loss when any one of them is excluded from the model. However, it is possible that these criteria will lead to the exclusion of a dimension relevant to the business.

Besides contributing to the non-convergence of the estimation algorithm, it is a well-known fact that the number of inputs and outputs affects the quality of results returned by the DEA model, as discussed in Berg [6] and in several other articles. The main impact is that the number of DMUs allocated on the efficiency frontier, that is, the number of DMUs that are used as reference to calculate others efficiency, tends to grow as the number of inputs and outputs increases [5].

This study proposes a method that will estimate DMU efficiency without excluding a single variable from the model, thus minimizing information loss and ensuring that the maximum possible variance is considered in the analysis, particularly discussing cases where it is possible to aggregate one or more inputs and/or outputs. A simulated data set was used to allow the accuracy of achieved results to be evaluated.

Unlike other available literature, which usually focuses on calculating and ordering the efficiency of each DMU, the main metric of the problem herein presented is the value by which each input is to be reduced or the value by which each output is to be expanded. Main focus was given to the Variable Returns to Scales (VRS) frontier model proposed by Banker et al. [7], since it is considered to be the most dynamic in terms of the assumptions it uses. Furthermore, models with slacks[1] were considered, to allow expansion or contractions of the outputs or inputs respectively, even in DMUs with an efficiency of one. As described by Agarwal [8], models that consider only radial efficiency metrics do not fully represent the DMUs potential for improvement.

2 Methodology

The method known as DEA was originally proposed by Charnes et al. [2], who used the ideas of Farrell [9] to create a linear programming problem to measure DMU efficiency.

[1]Slacks are conditions that can be included to the linear problem to consider output increase in an input-oriented model or input decrease in an output-oriented model.

The authors proposed calculating the efficiency of a given DMU based on the pondered ratio between the outputs (u_r) and inputs (v_i) related to this DMU. Mathematically, this was expressed as follows:

$$\begin{gathered}
\max h_0 = \frac{\sum_{r=1}^{s} u_r y_{r0}}{\sum_{i=i}^{m} v_i x_{i0}} \\
\text{subject to} \\
\frac{\sum_{r=1}^{s} u_r y_{rj}}{\sum_{i=1}^{m} v_i x_{ij}} \leq 1, \forall 1 \leq j \leq n \\
u_r, v_i \geq 0 \\
1 \leq r \leq s \\
1 \leq i \leq m,
\end{gathered} \tag{1}$$

where $y_{.j}$ and $x_{.j}$ are, respectively, the outputs and inputs used by the DMU j, h_0 is the efficiency of DMU *0*, and s and m are, in that order, the quantity of outputs and inputs considered in the model. Values assumed by $y_{.j}$ and $x_{.j}$ must be strictly positive and known.

This formulation does not describe a linear programming problem, which may render its solution difficult. Therefore, certain transformations are made, resulting in the following equivalent linear problem (LP):

$$\begin{gathered}
\min E_0 \\
\text{subject to} \\
E_0 x_{r0} \leq \sum_{k=1}^{n} \lambda_k x_{rk}, \ \forall 1 \leq r \leq s \\
y_{i0} \leq \sum_{k=1}^{n} \lambda_k y_{ik}, \ \forall 1 \leq i \leq m \\
\lambda_k \geq 0.
\end{gathered} \tag{2}$$

In this case, E_0 represents input efficiency for DMU 0 and can be interpreted as the complement of the radial contraction to be applied to the inputs, in order for the DMU to achieve full efficiency. For example, when $E_0 = 0.6$, the DMU in question must reduce the value of inputs by 40% and preserve the same number of outputs, to become efficient in the data set employed.

To compute output efficiency, the LP (1) must be changed to reflect the following result:

$$\begin{aligned} &\min F_0 \\ &\text{subject to} \\ &x_{r0} \leq \sum_{k=1}^{n} \lambda_k x_{rk}, \ \forall 1 \leq r \leq s \\ &F_0 y_{i0} \leq \sum_{k=1}^{n} \lambda_k y_{ik}, \ \forall 1 \leq i \leq m \\ &\lambda_k \geq 0. \end{aligned} \tag{3}$$

In this scenario, F_0 can be interpreted as the expansion to be applied to the outputs without changing the number of inputs used, for the DMU to be considered efficient in the data set employed.

Models (1) and (2) consider the CRS (Constant Return to Scale) technological frontier. The main four technological frontiers for the DEA model are:

1. CRS (Constant Return to Scale)—Products increase linearly with inputs, zero products equals zero products
2. VRS (Variable Return to Scale)—Products increase not linearly with inputs, zero products not equals zero products
3. DRS (Decreasing Return to Scale)—Products increase not linearly with inputs, zero products equals zero products
4. IRS (Increasing Return to Scale)—Products increase linearly with inputs, zero products not equals zero products

Each one of these frontiers is associated with a set of assumptions regarding the behavior of the technological frontier of the evaluated DMUs. Figure 1 is a comparison of the frontiers for a simulated data set.

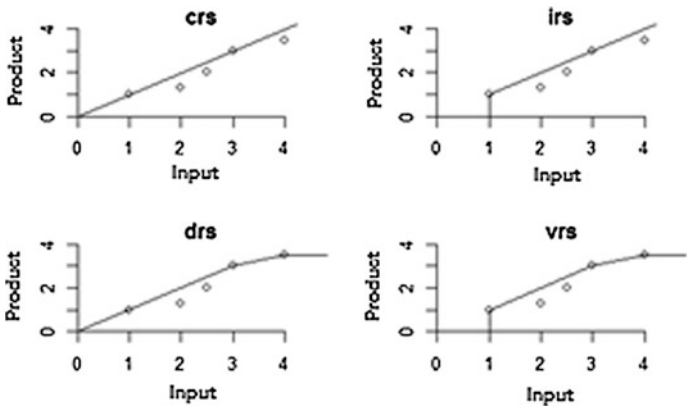

Fig. 1 Comparing technological frontiers

The choice of each frontier affects the model's equations. VRS, for example, is defined as follows:

$$\begin{gathered} \min E_0 \\ \text{subject to} \\ E_0 x_{r0} \leq \sum_{k=1}^{n} \lambda_k x_{rk}, \ \forall 1 \leq r \leq s \\ y_{i0} \leq \sum_{k=1}^{n} \lambda_k y_{ik}, \ \forall 1 \leq i \leq m \\ \lambda_k \geq 0 \\ \sum_{k=1}^{n} \lambda_k = 1 \end{gathered} \tag{4}$$

In their book, Bogetoft and Otto [10] summarize all the changes related to the production frontier and the assumptions linked to each one. They also describe in detail the modeling involved in DEA, presenting example and applications in the R statistics software.

As can be seen in the cases of IRS, DRS, and VRS, a portion of the frontier is vertical/horizontal. This means that a given DMU can be on the efficiency frontier and even so, reduce the number of inputs used or increase the quantity of outputs produced. To correct this characteristic, slacks in the model are allowed, creating room for improvement even for DMUs that act on the efficiency frontier.

In the present study, VRS frontier models with slacks were considered, since they present more flexibility compared to the other combinations.

3 Experimental Analysis

In this section, we present an experimental analysis carried out to evaluate the effectiveness of the proposed method.

3.1 Synthetic Dataset

To guide the studies, a database with 500 DMUs was first simulated, each one with two inputs and four outputs. The inputs, henceforward called x_1 and x_2, received random values, according to a uniform distribution, with intervals [10, 500] and [15, 300], respectively.

Every output was considered a result of the inputs, and the pondered sum of its logarithms was as follows:

$$y_1 = \beta_1 * \ln(x_1) + \beta_2 * \ln(x_2)$$
$$y_2 = \beta_3 * \ln(x_1) + \beta_4 * \ln(x_2)$$
$$y_3 = \beta_5 * \ln(x_1) + \beta_6 * \ln(x_2)$$
$$y_4 = \beta_7 * \ln(x_1) + \beta_8 * \ln(x_2),$$

where β_i, for $i = 1,\ldots,8$, are nonrandom values arbitrarily defined. For the specific case of this study, the values were defined according to Table 1.

Furthermore, to simulate the inefficiency of each DMU, each output was multiplied by a random disturbance, according to a uniform distribution in the [0.1, 1] interval, and y_5 was defined as the sum of y_2, y_3 and y_4.

It is, thus, possible to know the exact output values every DMU must achieve to become efficient, allowing the accuracy of each method to be estimated.

3.2 DEA Models

DEA models can be defined either as input-oriented, if the main goal is to reduce inputs while keeping outputs producing unaltered, or as output-oriented, if the main goal is to maximize the output while keeping the inputs unaltered. Input- and output-oriented VRS frontier models with and without slacks were applied to the simulated data set. Five models were applied in every parameterization, as described in Table 2.

The reference for the efficiency value is thus computed for the complete model, which contains all the variables pertinent to the problem in question. In general, the approach would be to apply model 1, with the aggregated variable. In this project, models 2, 3, and 4 will therefore be called marginal models.

Table 1 Constants defined for the simulation

β_1	β_2	β_3	β_4	β_5	β_6	β_7	β_8
61	97	76	89	62	95	56	60

Table 2 List of variables included in the models

Model	Inputs		Outputs			
Complete	x_1	x_2	y_1	y_2	y_3	y_4
1	x_1	x_2	y_1	y_5	–	–
2	x_1	x_2	y_1	y_2	$y_5 - y_2$	–
3	x_1	x_2	y_1	y_3	$y_5 - y_3$	–
4	x_1	x_2	y_1	y_4	$y_5 - y_4$	–

4 Results

Figure 2 compares the estimated efficiency of the complete model with the estimated efficiency of model 1, under output-oriented VRS parameterization, with no slacks.

It can be observed that 98% of the values computed for efficiency by model 1 overestimate the reference value computed by the complete model. The other models presented a similar behavior, with only a subtle variation in the dispersion. Based on this result, it was proposed to use the minimum between the computed efficiency values in models 2, 3, and 4 as an estimate for the efficiency of the complete model.

Results can be observed in Fig. 3, and leave no doubt that the results of this method are more accurate than aggregating variables. Pearson's correlation between

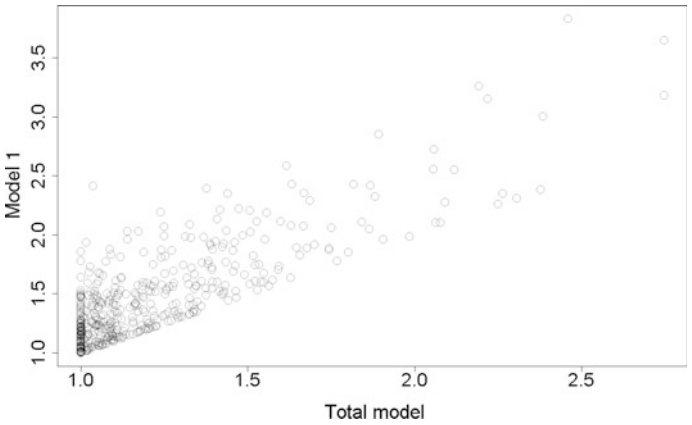

Fig. 2 *Scatterplot* between computed efficiency for the complete model and model 1, note that the correlation of the firm's efficiency is not close to one

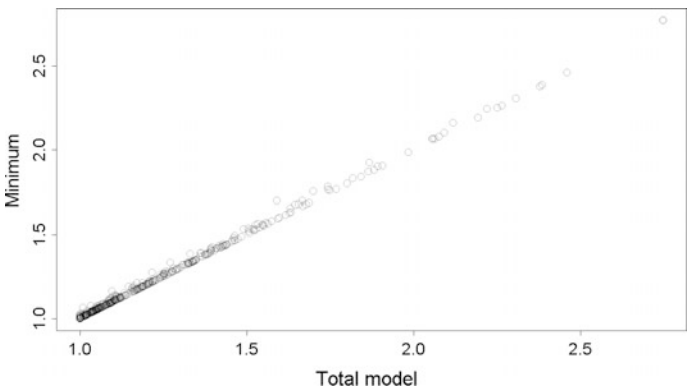

Fig. 3 *Scatterplot* between the minimum marginal efficiencies and the complete model, note that the efficiency is very close to one

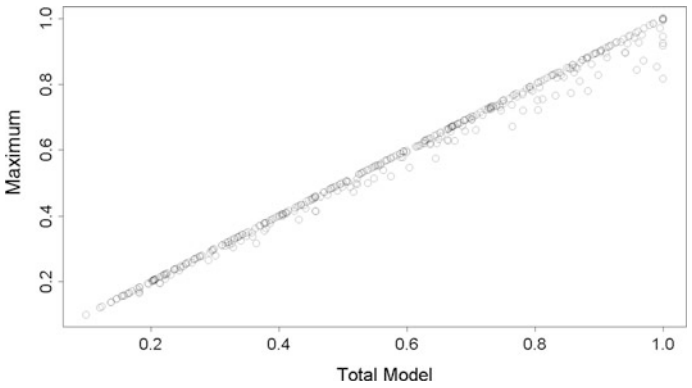

Fig. 4 *Scatterplot* between the maximum marginal efficiencies and the complete model, note that the efficiency is very close to one

the variables was 0.9995, in contrast with the correlation between the efficiency of the complete model and model 1, which was 0.8009.

Since no slacks were included in the model, potential for improvement is directly proportional to efficiency, proving this metric is also more accurate than considering the minimum of the marginal models.

The procedure of the output-oriented model is similar, except for the fact that maximum marginal efficiency is used instead of minimum marginal efficiency. Figure 4 shows the results.

The measured correlation for the maximum marginal efficiencies and the complete model was 0.9983, while the correlation between the complete model and model 1 efficiency was 0.7599.

This demonstrates the effect that grouping variable can have on DEA model results, whether input-oriented or output-oriented, indicating that this method involves considerable information loss.

To validate the results achieved for the first simulation, a thousand samples were generated, with β_i (for i = 1,…,8) assuming random values between 50 and 100, and random disturbances as described in Sect. 3.

For the input-oriented model, Fig. 5 shows the comparison between the estimated densities for the correlation between the efficiency computed for the complete model and the two methods, model 1 and the marginal model minimum. Model 1 presented results below the minimum in every single simulation.

For output-oriented parameterization, the results of model 1 were slightly better, as shown in Fig. 6 When compared with the maximum, however, the conclusion remains the same.

For models that consider slacks in their variables, it is not enough to have more accurate estimated efficiency, since besides the contraction/expansion produced by the efficiency, slacks allow outputs to be increased and inputs decreased by additional values.

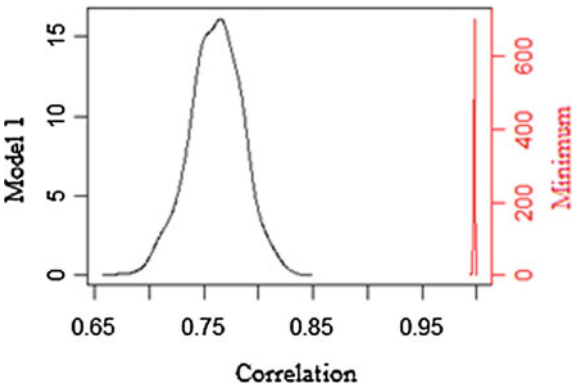

Fig. 5 Estimated densities for correlation—input-oriented model, for every simulation the marginal model minimum showed a stronger correlation on estimated efficiency than model 1

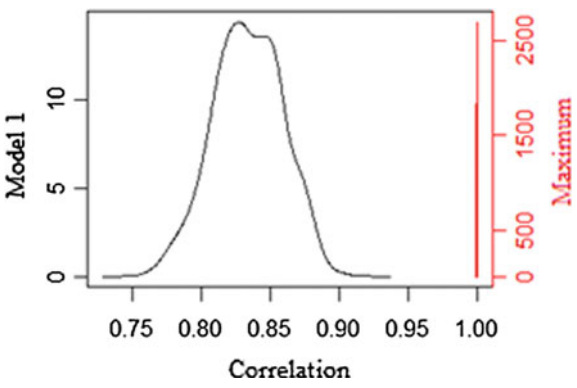

Fig. 6 Estimated densities for correlation—output-oriented model, for every simulation the marginal model maximum showed a stronger correlation on estimated efficiency than model 1

The following variables are defined as the goal for outputs and inputs, respectively:

$$y^*_{ki} = y_{ki} * ef_i + sy_{ki}$$
$$x^*_{li} = x_{li} * ef_i - sx_{li},$$

where $i = 1,\ldots,500$ indexes the DMU, $k = 1,\ldots,5$ indexes the output, $l = 1,2$ indexes the input and sy_{ki} and sx_{li} are the computed slacks.

Model 1 uses variable y_5 as an output and therefore the goal of the variables forming it must be inferred based on its own goal. A proportionate distribution among the variables was performed as the criterion, as follows:

$$y^*_{mi} = \left(\frac{y^*_{5i}}{y_{5i}}\right) * y_{mi}$$

with $m = 2$, 3 and 4.

The goal when using output-oriented and input-oriented marginal models was respectively defined as follows:

$$y^*_{ki} = y_{ki} * \text{minimum}_i + sy_{ki} * I(\text{minimum}_i)_{\{1\}^c}$$
$$x^*_{li} = x_{li} * \text{maximum}_i - sx_{li} * I(\text{maximum}_i)_{\{1\}^c},$$

where sy_{ki} is the margin computed in the k-umpteenth model.

Previous simulations were redone taking model slacks into consideration, and the goal of each variable was calculated both ways, using model 1 and the marginal models. Results revealed no significant modifications regarding efficiency, when slacks in the models were taken into consideration.

Figure 7 shows simulation results for computed goals. Among the goals computed in the complete model, densities for the correlation of goals computed by model 1 are in black, and goals computed by marginal models are in red. Solid lines refer to y_2, dashed lines to y_3 and finally, dotted lines to y_4.

It is clear that the method using the marginal models presented superior results for the outputs that were aggregated. Figure 8 compares the two methods: marginal models are in red and model 1 in black.

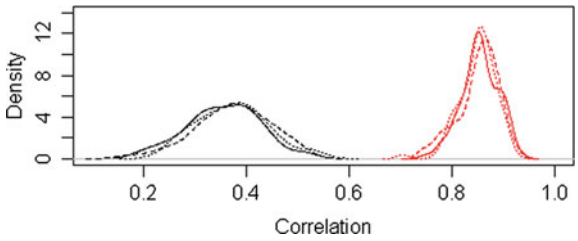

Fig. 7 Comparing the correlation between the two methods for computing goals for y_2, y_3, and y_4, note that the correlation for the marginal model is considerably higher than model 1 correlations

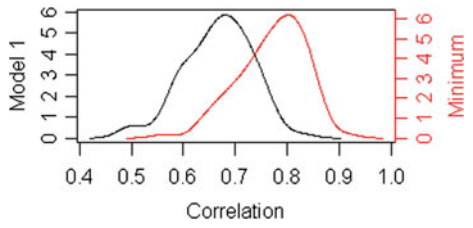

Fig. 8 Comparing the correlation between the two methods for computing goals for y_1. Although the difference is not as expressive as for the other outputs, the method using the marginal models was still better than that of the one using model 1

5 Final Considerations

Achieved results clearly show that for cases with conditions similar to those simulated, marginal models return results significantly superior to those obtained using model 1, that is, aggregating variables and adding them to the model as a single output.

The input-oriented case was not studied with the same thoroughness as the output-oriented case, although preliminary results led to the same conclusions.

Furthermore, it is important to expand validation to a scenario with more inputs and outputs to evaluate how the method will behave under different conditions. Other factors also need to be considered in future simulations, such as models with return to scale frontiers other than VRS, scenarios with less DMUs, and the way changes in the input and output scale affect the efficiency of the proposed method. Furthermore the application of this method on collected and not simulated data could reveal more insights.

The approach of this paper is compliant with the philosophy behind the DEA model, that is, finding the best possible scenario comprising all DMUs. Therefore, considering the minimum or maximum of the marginal models returns results closer to those of the complete model than aggregating outputs, scenario in which information relevant to the analyzed problem is lost.

References

1. Montgomery DC, Peck EA, Vining GG (2012) Introduction to linear regression analysis. Wiley
2. Charnes A, Cooper WW, Rhodes E (1978) Measuring the efficiency of decision making units. Eur J Oper Res 2(6):429–444
3. Tone K, Tsutsui M (2009) Network DEA: a slacks-based measure approach. Eur J Oper Res 197)(1):243–252
4. Jenkins L, Anderson M (2003) A multivariate statistical approach to reducing the number of variables in data envelopment analysis. Eur J Oper Res 147(1):51–61
5. Senra LFADC et al (2007) Estudo sobre métodos de seleção de variáveis em DEA. Pesqui Oper 27(2):191–207
6. Berg SV (2010) Water utility benchmarking: measurement, methodologies, and performance incentives. IWA Publishing
7. Banker RD, Charnes A, Cooper WW (1984) Some models for estimating technical and scale inefficiencies in data envelopment analysis. Manag Sci 30(9):1078–1092
8. Agarwal S, Yadav SP, Singh SP (2011) A new slack DEA model to estimate the impact of slacks on the efficiencies. Eur J Oper Res 12(3):241–256
9. Farrell MJ (1957) The measurement of productive efficiency. J R Stat Soc Ser A (Gener):253–290
10. Bogetoft P, Otto L (2010) Benchmarking with DEA, SFA, and R. Springer

Method for Estimating Confidence Intervals for DEA Efficiency Models Using Regression Models

Filipe Giovani Bonin Bisoffi, Graziella Cardoso Bonadia, Victor Henrique Duarte de Oliveira and Sérgio Ricardo Barbosa

Abstract Benchmarking methods, such as DEA (Data Envelopment Analysis), are used to compare a set of entities regarding their efficiency in a given process. The structure of the DEA method does not take random disturbances into consideration when estimating the efficiency of each entity. In most scenarios, this characteristic does not reflect the reality of the problem, since practically the entire process is subject to external disturbances. Using regression methods, it is possible to generate confidence intervals for DEA-estimated efficiency, considering the model's inputs and outputs as independent variables. With this, the conclusions and subsequent actions based on the returned results are more robust, and begin to contemplate, in a certain manner, random disturbances suffered by the companies.

Keywords DEA · Confidence interval · Nonparametric regression analysis

1 Introduction

Benchmarking is a method used to compare the performance (according to a given metric) of a certain entity, as schools or hospitals, using a reference or benchmark. It is widely used to measure the efficiency of a set of firms or DMUs (Decision-Making Units), as they are generally known in the literature. Given a set of firms with multiple inputs and outputs, a benchmarking method allows to measure the relative performance of the firms through the generation of a curve (frontier) of efficient firms which are obtained by the combination of the providing

F.G.B. Bisoffi (✉) · G.C. Bonadia
Decision Management Support & Applications Department, CPqD - Telecommunications Research and Development Center, Campinas, Brazil
e-mail: fbisoffi@cpqd.com.br

V.H.D. de Oliveira · S.R. Barbosa
CEMIG Distribuição S.A., Belo Horizonte, Brazil
e-mail: srb@cemig.com.br

A. Paradisi et al. (eds.), *Cognitive Technologies*, Telecommunications and Information Technology, DOI 10.1007/978-3-319-53753-5_2

firms. The performance can be measured in terms of the entity productivity or its cost efficiency of inputs to produce outputs.

As observed by Molinero and Woracker [1], benchmarking techniques are especially interesting for organizations that work with inputs or outputs that cannot be monetized. An example of application in this situation can be found in Lorenzett et al. [2], comparing the efficiency of a set of operational units from a network of not-for-profit secondary level professional schools. In this particular example the inputs considered where the total investment and total money transfer of the industry to the school unit. As outputs, the overall performance, the self-sustentation percentual, the client satisfaction index, the product quality index and the quality of management index were considered.

The two main techniques used in benchmarking are the DEA [1] and SFA (Stochastic Frontier Analysis) [3]. The first uses a nonparametric and deterministic structure and the second uses a parametric and stochastic structure. When choosing between a parametric or nonparametric model, one should consider that nonparametric models are more flexible, given that they adapt to the patterns of the data instead of a predefined one. On the other hand, if the chosen model structure is well suited to the underlying nature of the data, the parametric model is expected to give better results. Regarding random effects in the process, stochastic models deal with the errors that are naturally expected in any dataset, either result of measure-related problems or of factors that cannot be measured. One can, thus, test the need to include the error term in the model, and if it is not significant, can opt for a deterministic model.

DEA is based on the solution of linear programming problem to compute the production frontier under which the companies work. This linear problem considers the efficiency as ratio of the outputs produced by the firm and the inputs used in the process. A deficiency of this method is that it does not take random noises into consideration when computing the frontier—consequently, estimates are interpreted deterministically. It is expected that most processes executed by the evaluated companies suffer random disturbances, and not taking this effect into consideration can compromise the efficiency of one or more DMUs assessed in the model.

One way of considering random fluctuations in DEA model results is to estimate confidence intervals for the computed efficiencies. In general, this is accomplished by means of a method known as *bootstrapping*, which consist of resampling the data with replacement to assess the distribution of a given set of estimators. As presented by Bogetoft and Otto [4], there are several alternative approaches to define this procedure. One form of calculating the confidence intervals described by Souza et al. [5], which can be applied to a DEA model with a single product, uses a regression model for this product as a response variable to estimate a confidence interval for the efficiencies. As observed by the author themselves, the literature for multiple product cases is not clear.

The scope of the present study is to build confidence intervals for efficiencies based on regression models trained, considering efficiency a dependent variable, inputs and outputs as independent variables and using DEA-estimated efficiencies as ground-truth to train the regressions. Based on the predicted models, confidence

intervals will be estimated for the efficiency of every DMU and compared with the results of those produced using the bootstrapping method.

2 Methods

Since efficiency can be considered in the interval [0, 1], to estimate confidence intervals it is possible to use the beta regression model proposed by Cribari-Neto and Zeileis [6] or a combination of beta regression models, as described by Grün et al. [7].

Another option is the normal linear regression models. They are adequate for this purpose, as Bogetoft and Otto [4] points out, since they assume that the set of real numbers is the domain of the dependent variable. The Tobit model is an alternative model that presumes normally distributed disturbances, as described in Amemiya [8], and allows variables with lower or upper limits to be modeled in its real domain.

However, these techniques are essentially parametric, in contrast to the DEA method, making it difficult to define an adequate model for the relation between efficiency, inputs and outputs. Therefore, we adopted here nonparametric regression models, for which there is no need to define the relationship between the independent and dependent variables. The estimation methods for this type of regression and other subjects, such as selecting the band matrix, are discussed in Fox [9].

In this work, we built and estimated DEA models using a Variable Return to Scale (VRS) efficiency frontier (also known as BCC model), as defined by Banker, Charnes, and Cooper [10]. We will not present in this paper the linear programming problem associated to DEA, used to compute DMU efficiency. Bogetoft [4] provided the needed theoretical foundation, using the free R Benchmarking package[1] to apply the methodology.

We followed the studies presented by Nadaraya [11] to estimate the nonparametric regressions used to model the DMUs. If ef_i is the calculated efficiency for the i-th DMU and Z_i the vector resulting from the concatenation of inputs X_i and outputs Y_i related to the i-th DMU, then the proposed regression model is described as

$$ef_i = g(Z_i) + \varepsilon_i, \tag{1}$$

where ε_i follows a distribution with $E(\varepsilon_i|Z_i) = 0$ and, thus, $E(ef_i|Z_i) = g(Z_i)$. Unlike parametric regression models, such as the Normal multivariate or beta models, no assumption about $g(Z_i)$ is needed to estimate the model, making this approach more flexible. Normal multivariate regression would assume $g(Z_i) = X\beta$, where X is a matrix—usually nonrandom—containing the observations of the prediction

[1] https://cran.r-project.org/web/packages/Benchmarking/index.html.

variables, and β is a weight vector. Furthermore, it would be assumed that ε_i follows a normal, independent, and homoscedastic distribution. In this case, it is possible to estimate models robust to violation of the residual assumptions, although the relation between the response variable and the predictive variables must be described parametrically.

As a regression model for $g(Z_i)$, we used the nonparametric estimator known as Nadaraya-Watson, which is defined by

$$\widehat{g}_h(z) = \frac{\sum_{j=1}^{n} K_h(z - z_j) ef_j}{\sum_{j=1}^{n} K_h(z - z_j)}, \tag{2}$$

for any kernel $K_h(x)$, with size n of the estimation sample, a nonrandom z vector and the h bandwidth used for estimation.

The kernel function must assume real nonnegative values and be an integrable symmetric function near zero. Furthermore, to ensure the estimated functions are probability distributions, the integral in $\mathbb{R}$ must be equal to one. The kernel proposed by Epanechnikov [12], named after its author, presents the best performance when the evaluated criteria is the average squared error [13]. However, we adopted in the current work the Gaussian kernel, as it is widely used since its estimations are only insignificantly less accurate compared to the Epanechnikov kernel, as proven by Wand and Jones [14], and features convenient mathematical properties.

The Gaussian kernel is defined as

$$K(u) = \frac{1}{\sqrt{2\pi}} e^{-\frac{1}{2}u^2}, \tag{3}$$

and receives this name because it is based on normal distribution. As for the multivariate case, it is common to accept the product of the marginal kernels in Eq. 2.

The h defines the weight given to each observation for the regression estimate at point z, according to its proximity to z. By choosing a small band, only points closest to z will have any impact on the estimate, while at the other extreme, when using a large band, all observations will have an impact on the estimate. Small values for h are associated with more accurate estimates, while larger values lead to less variable estimates. The band should consider a trade-off between these two equally important characteristics.

This effect can be seen in Fig. 1, which shows the estimate for simulated data density originating from a bimodal normal distribution with an averages −2 and 2. It is clear that the higher band value was unable to properly capture the two true distribution averages, and the lower band value leads to the conclusion that there is more variability in the data distribution than there actually is.

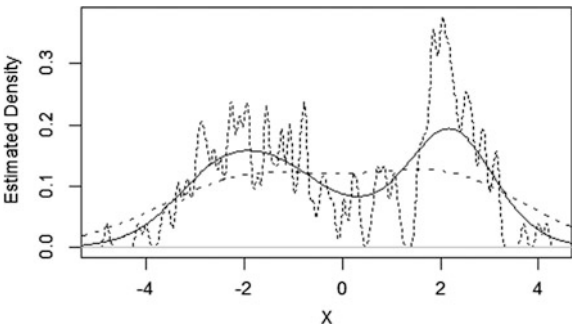

Fig. 1 Comparison of results using different bands. The *dotted line* represents an estimate with a 0.05 band; the *dashed line*, a 1.5 band; and the *solid line*, a 0.6807 band. Notice that a small value for h leads to a overfit on the data and a high value for h leads to a underfit on the data

Ideally, the bands used should, when $n \to \infty$, satisfy $h_n \to 0$ and $nh_n \to \infty$. That is, when the sample size increases, the band must tend to make increasingly local estimates, while increasing the number of observations used to estimate each window.

Several best band selection methods were summarized by Turlach et al. [15], who also present a series of studies on which method is the best. However, their conclusion was that none of the studies reviewed was definitive, and that some of the methods will inevitably have better results in different situations.

The estimates presented in the present work use the band selection method introduced by Li and Racine [16], for generalized multiplicative kernels implemented in the R language inside the NP package,[2] by Hayfield and Racine [17].

The confidence interval for $\widehat{g}_h(z)$ was generated by a bootstrapping procedure. Proposed by Efron [18] based on the *jackknife* method, bootstrapping is a resampling method that generates new samples taken from the original sample, and statistics of interest are computed from these samples. Based on these results, inferences can be made regarding the distribution of these statistics. The concept behind this method is that the bootstrap samples are to the original sample what the original sample is to the population. Since it allows statistical distribution inference without the need for many assumptions, it is a widely used method, especially when the involved algebra becomes too complex, making it hard to identify the theoretical distribution.

3 Data Sets

To evaluate the proposed method, random data sets were created to compute a DEA model and later estimate a nonparametric regression model. Two inputs and four outputs (based on the inputs) were simulated.

[2] https://www.cran.r-project.org/web/packages/np/index.html.

Table 1 Simulation parameter values

	1st round	2nd round
β_1	190	100
β_2	1.5	1.5
β_3	1	1
β_4	90	70
β_5	10	40
β_6	16	50
β_7	0.01	0.1
β_8	15	20

The inputs were simulated as uniform distributions, with the following parametrization:

$$x_1 \sim U[10; 500]$$
$$x_2 \sim U[15; 300]$$

and the outputs with the following equations:

$$y_1 = \beta_1 * \ln(x_1) + \beta_2 * x_2$$
$$y_2 = \beta_3 * x_1 + \beta_4 * \ln(x_2)$$
$$y_3 = \beta_5 * \ln(x_1) + \beta_6 * \ln(x_2)$$
$$y_4 = x_1^{\beta_7} + \beta_8 * \ln(x_2),$$

where β_i, $i = 1, \ldots, 8$ are nonrandom values predefined for each simulation round.

Variables were simulated for 500 DMUs and, to simulate inefficiencies of each DMU, the outputs were multiplied by random reduction factors selected according to a uniform distribution between 0.3 and 1.

The values chosen for β_i were defined according to Table 1.

Once the data sets were simulated, the methods and models described in the previous section were applied to each one of them.

4 Results

DEA models can be defined either as input-oriented, if the main goal is to reduce inputs while keeping outputs producing unaltered, or as output-oriented, if the main goal is to maximize the output while keeping the inputs unaltered an input-oriented DEA model with a VRS frontier was applied to the simulation rounds, without

Table 2 Summary of estimated measured DMU efficiencies

Interval	Quantity	Percentage
0.1 <= ef < 0.2	4	0.8
0.2 <= ef < 0.3	9	1.8
0.3 <= ef < 0.4	23	4.6
0.4 <= ef < 0.5	37	7.4
0.5 <= ef < 0.6	49	9.8
0.6 <= ef < 0.7	59	11.8
0.7 <= ef < 0.8	59	11.8
0.8 <= ef < 0.9	51	10.2
0.9 <= ef < 1	63	12.6
ef = 1	146	29.2

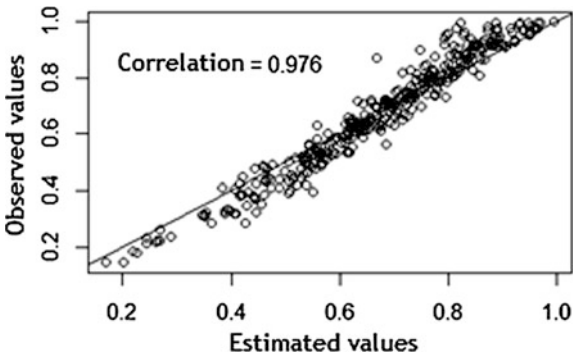

Fig. 2 Relation of N.P. model versus observed values. The *solid line* represents a *straight line* with intercept at the origin and an angular coefficient of one. Ideally, the values should be arranged randomly around the *straight line*. A slight tendency was observed in the lower and higher values, but was not considered detrimental to the model as a whole

slacks,[3] using the R Benchmarking package. Efficiencies for all DMU were computed based on each estimated model.

Table 2 is a summary of the DMU profiles for the first simulation round, as estimated by the DEA model. The quantity and percentage of total DMUs for the entire efficiency interval are also presented. Efficiency values of one were not considered for model estimation. These cases will receive different treatment from the rest.

Figure 2 presents the scatterplot between the estimated values for the efficiency of each DMU using the regression model, and the observed values, computed by the DEA model, together with the correlation between the variables. A strong correlation between the variables can be observed, indicating that the model's accuracy is satisfactory.

[3]Slacks are conditions that can be included to the linear problem to consider output increase in an input-oriented model or input decrease in an output-oriented model.

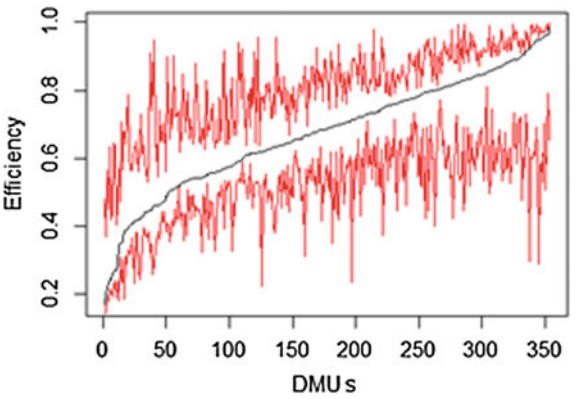

Fig. 3 Ordered efficiency and confidence intervals for the nonparametric model. The *black line* represents the efficiency values estimated by the nonparametric regression model, and the values in *red* represent the upper and lower limits for the confidence interval of 95%

With these results in hand, one hundred bootstrap samples were generated, according to the following algorithm:

1. Repeat 100 times:
   1.1. Sample, with replacement, the observations used for model estimation, with the size of the sample equal to that used to estimate the original model.
   1.2. Estimate the best band for the data set generated in step 1.1.
   1.3. Using the band estimated in step 1.2, compute the estimated efficiency for each point of the original sample.

It was verified that after one hundred rounds, the bootstrap efficiency distribution, estimated by means of the bootstrap sample, did not suffer significant changes, indicating that the number of samples was sufficient for estimator convergence. Figure 3 shows the results achieved by the bootstrap procedure described above. The upper and lower limits were calculated using the 97.5th and 2.5th percentile, respectively, of the generated bootstrap samples.

The idea underlying this procedure is that the result of each DMU is part random and part deterministic, but the efficiency frontier is fixed.

Figure 4 shows the smoothened confidence limits, using the HoltWinters method for time series, without the seasonal component from decomposition, since in the context of the analysis, there is no point in including it. More details on the smoothening method can be checked out in Morettin and Toloi [19]. Smoothening the interval limits should provide more robust results, since part of the variance is absorbed in the process, and make the graphic presentation more readable.

The estimated bias calculated by the bootstrap samples was very close to zero, indicating that the estimates for the generated samples are consistent.

In order to establish a comparison criteria, the bootstrap procedure with bias correction described by Bogetoft and Otto [4] for estimating confidence intervals was also applied to the samples, assuming an input-oriented model with VRS frontier, as in the previous procedure. The R Benchmarking package was used to compute the confidence intervals.

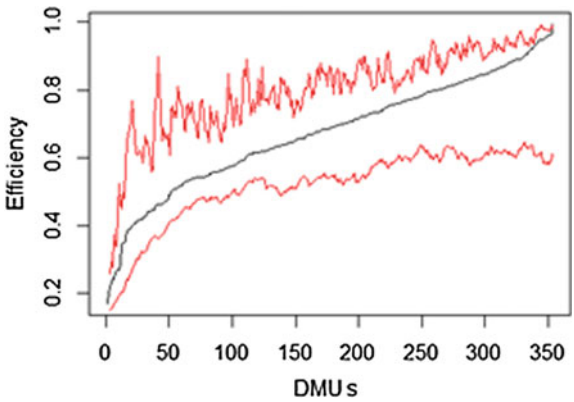

Fig. 4 Ordered efficiency and smoothened confidence intervals for the nonparametric model

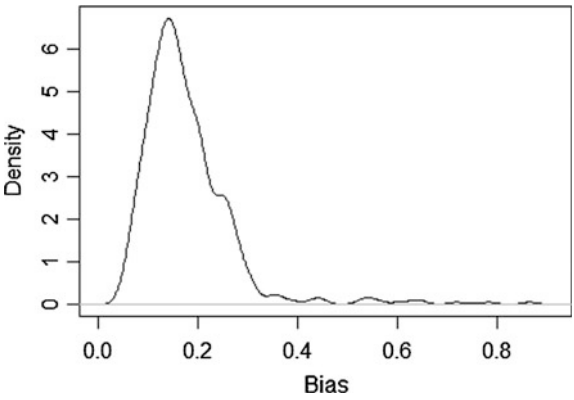

Fig. 5 Estimated density for the bias computed for the first round sample

Figure 5 shows the density estimated in the bootstrap process for the efficiency bias of the DMUs simulated in the first round. Since DEA is positively biased for VRS frontier, in other words, the estimated values for the efficiency of each DMU always overestimate the real value of the parameter, the bias is strictly positive [20]. This happens because the PL built based on the data finds the smallest frontier containing all the observations.

Results of the confidence intervals are displayed in Fig. 6. The black line is the computed efficiency, with no bias correction, for each DMU in the first simulation round, with the values sorted in ascending order.

Efficiencies with bias correction presented incoherent results with negative values and were therefore discarded by the study. The method used in this bootstrap process is based on the concept that computed efficiency is always superior to theoretical efficiency; therefore, the confidence intervals are always lower than the returned values.

As in the previous procedure, HoltWinters smoothening was applied to the confidence interval limits. However, for this case, smoothening was applied only to

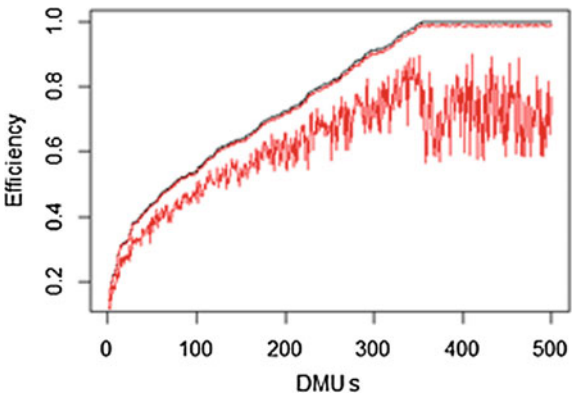

Fig. 6 Ordered efficiency and confidence intervals. The two *red lines* delimit the 95% confidence interval limit for all DMUs

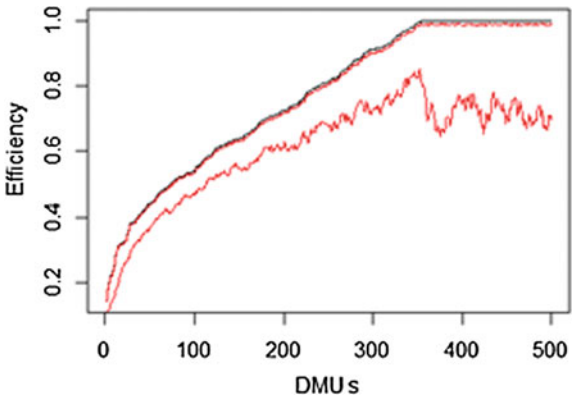

Fig. 7 Ordered efficiency and confidence intervals with smoothened lower limit

the lower limit, since the upper limits presented no significant variance. Figure 7 displays the returned results.

It is interesting to observe that the lower limit of the DMU confidence interval with an efficiency equal to one is lower than the limit of those presenting an efficiency in the [0.7, 1] interval. It would be expected that the limits would follow the value observed for the efficiencies estimated in the original base.

5 Final Considerations

The achieved results show that the two methods studied present conceptual differences. The usual methods, as presented by Bogetoft and Otto [4], are based on the principle that the computed efficiencies are always higher than the real ones, since the frontier computed by the DEA method is the smallest possible. Thus, the objective is to try to define, using a smoothened resampling process, larger frontiers

and generate, for these frontiers, the confidence interval for the efficiencies of each DMU. This way, the information contained in the data can be extrapolated.

The proposed procedure, which uses a nonparametric regression model is based on the idea that each DMU is affected not only by management efficiency, but by random fluctuations as well, and could therefore present better or worse performance than what is displayed. Such random fluctuations are separated from the deterministic part by the nonparametric model, allowing confidence intervals to be generated with the information contained in the data collected originally.

Therefore, it makes no sense to compare the two procedures quantitatively. The choice as to how to build the confidence interval depends on the context of the problem, and the object underlying the analysis. Following the first approach, the intervals are always inferior to the efficiencies originally computed for the DMUs, while the second approach returns intervals that contain the original efficiency.

Furthermore, it is important to point out that the processing time of the first approach is considerably lower than that of the second approach, because of the heavy computational effort required to estimate optimal bands for the nonparametric regression model.

References

1. Molinero CM, Woracker D (1996) Data envelopment analysis. Or Insight 9(4):22–28
2. Lorenzett JR, Lopes ALM, De Lima MVA (2010) Aplicação de método de pesquisa operacional (DEA) na avaliação de desempenho de unidades produtivas para área de educação profissional. Revista Eletrônica de Estratégia & Negócios 3(1):168–190
3. Kumbhakar SC, Lovell CAK (2003) Stochastic frontier analysis. Cambridge University Press
4. Bogetoft P, Otto L (2010) Benchmarking with DEA, SFA, and R. Springer
5. Souza G, Souza M, Gomes E (2011) Computing confidence intervals for output-oriented DEA models: an application to agricultural research in Brazil. J Oper Res Soc 62(10):1844–1850
6. Cribari-Neto F, Zeileis A (2009) Beta regression in R
7. Grün B, Kosmidis I, Zeileis A (2011) Extended beta regression in R: shaken, stirred, mixed, and partitioned. Working papers in economics and statistics
8. Amemiya T (1984) Tobit models: a survey. J Econom 24(1):3–61
9. Fox J (2002) An R and S-plus companion to applied regression. Sage
10. Banker RD, Charnes A, Cooper WW (1984) Some models for estimating technical and scale inefficiencies in data envelopment analysis. Manag Sci 30(9):1078–1092
11. Nadaraya EA (1964) On estimating regression. Theor Probab Appl 9(1):141–142
12. Epanechnikov VA (1969) Non-parametric estimation of a multivariate probability density. Theor Probab Appl 14(1):153–158
13. Comaniciu D, Meer P (1999) Mean shift analysis and applications. In: The proceedings of the seventh IEEE international conference on computer vision. IEEE, pp 1197–1203
14. Wand MP, Jones MC (1994) Kernel smoothing. CRC Press
15. Turlach BA et al (1993) Bandwidth selection in kernel density estimation: a review. Université catholique de Louvain
16. Li Q, Racine J (2004) Cross-validated local linear nonparametric regression. Stat Sin 14 (2):485–512

17. Hayfield T, Racine JS (2008) Nonparametric econometrics: the np package. J Stat Softw 27 (5). http://www.jstatsoft.org/v27/i05/
18. Efron B (1979) Bootstrap methods: another look at the jackknife. In: The annals of statistics, pp 1–26
19. Morettin PA, Toloi C (2006) Análise de séries temporais. Blucher
20. Lothgren M (1998) How to bootstrap DEA estimators: a Monte Carlo comparison. WP in Economics and Finance, no 223

Distributed Averaged Perceptron for Brazilian Portuguese Part-of-Speech Tagging

Valter Akira Miasato Jr., Bruno Gonçalves, Bruno Ribeiro Costa and José Eduardo De Carvalho Silva

Abstract Part-of-Speech Tagging is a problem in Natural Language Processing (NLP) which consists of grammatically labeling textual elements. To accomplish this task, there are models either rule-based or driven by machine learning algorithms. Though semi-supervised strategies have been proposed recently, this work employs a fully supervised learning technique. This technique is the Averaged Perceptron, already applied to the POS Tagging task in English, and used for the Brazilian Portuguese language in this work. An accuracy superior to 97% was achieved, as it was also shown that it is possible to speed up the convergence time of the algorithm more than two times using parallel training strategies.

Keywords Natural language processing · Structured prediction · Averaged perceptron · Parallel processing

1 Introduction

The Natural Language Processing (NLP) field, among other tasks, deals with the problem of transforming human language into machine-readable information. Many techniques emerge as means of dealing with language, being Part-of-Speech Tagging one of them.

V.A. Miasato Jr. (✉) · B. Gonçalves · B.R. Costa · J.E. De Carvalho Silva
Campinas, Brazil
e-mail: valterf@cpqd.com.br

B. Gonçalves
e-mail: brunog@cpqd.com.br

B.R. Costa
e-mail: brunoc@cpqd.com.br

J.E. De Carvalho Silva
e-mail: jcsilva@cpqd.com.br

A. Paradisi et al. (eds.), *Cognitive Technologies*, Telecommunications and Information Technology, DOI 10.1007/978-3-319-53753-5_3

POS Tagging is a process in which tokens, typically words and punctuation, are given grammatical labels, which may be used as new features from the given piece of text. In speech synthesis and recognition, such features are useful for disambiguation, sequence prediction, and lexicographic search.

Given POS Tagging's wide range of applications and its straightforward evaluation, there are many statistical approaches available in this field [9]. However, for Brazilian Portuguese there is still room for improvement, either in correcting corpora [5], or in the employment of techniques only used in other languages so far [2].

This work will present the Averaged Perceptron, which is described as an algorithm of structured prediction in Sect. 2, and further detailed in its sequential and distributed implementations. The dataset is presented in Sect. 3, and the experiments and results are shown in Sects. 4 and 5. We aim to describe a state-of-the-art tool for the POS Tagging task for Brazilian Portuguese.

2 Structured Prediction

A structured prediction task consists of classifying a set of elements which arrange themselves as a structure, rather than predicting them individually [3]. A common instance of structure is a sequence, which may be exemplified in our task by an arrangement of textual elements, being them words, digits, or punctuation. Each element may belong to a limited set of classes, such as verb, article or noun, and the sequence of all predicted classes is the prediction for the text as a whole.

Verifying all possible sequences of arbitrary elements is an intractable problem. Thus, there are many techniques to reduce their computational cost, leaving only the likeliest sequences to be evaluated. The Structured Perceptron [2] is a discriminative algorithm, which estimates probabilities of labels based on features both from the unlabeled sequence and the predicted history. The following subsections explain basic concepts, which compose the full algorithm.

2.1 Perceptron

The Perceptron is described as an error-driven learning process, used for generating a linear classifier through supervised training. Its task is predicting classes c for new observations x given a labeled training set. For each prediction, the classifier is updated if the predicted class deviates from its reference.

2.1.1 Binary and Multiclass Perceptron

In its original form, the Perceptron is a binary classifier for a given class c in which there are:

- a cost function $f(x, c)$,
- a feature vector $\mathbf{h}(x, c)$,
- a weight vector $\mathbf{w}$ with the same dimension of $\mathbf{h}$,
- a bias $b(c)$.

Together, they process the input (x, c) in a cost $f(x, c)$:

$$f(x, c) = -\mathbf{h}(x, c) \cdot \mathbf{w} - b(c). \tag{1}$$

If $f(x, c) < 0$, then x belongs to class c, otherwise, it does not.

To modify the task in a multiclass prediction, i.e., predict a single class $\hat{c}$ for x, we choose the class, which returns the minimum cost:

$$\hat{c}(x) = arg\, min_c(f(x, c)). \tag{2}$$

We train the Perceptron by updating the weight vector $\mathbf{w}$ and the biases $b(c)$ through the update-on-error rule, as we iterate through the training set. Consider the weight vector $\mathbf{w}$ as initialized with null values. Let $(x_i, c_i), 1 \leq i \leq n$ be the training set with n examples, and $\hat{c}_i = \hat{c}(x_i)$. Given this, we may define an update decision function $g(i)$:

$$g(i) = \begin{cases} 0, & \text{if } \hat{c}_i = c_i, \\ 1, & \text{otherwise.} \end{cases} \tag{3}$$

Subsequently, the weights and biases are updated in each example of the training set:

$$\mathbf{w} \leftarrow \mathbf{w} + \alpha[g(i)\mathbf{h}(x_i, c_i) - g(i)\mathbf{h}(x_i, \hat{c}_i)], \tag{4}$$

$$b(c) \leftarrow b(c) + \alpha g(i), \tag{5}$$

$$b(\hat{c}) \leftarrow b(\hat{c}) - \alpha g(i), \tag{6}$$

in which α is the learning rate, with its value typically belonging to the range $(0, 1]$.

Those three steps (Eqs. (4), (5), and (6)) may be, respectively, seen as a penalty to the wrong predictions, increasing the cost of the pair $(x_i, \hat{c}_i)$, and a scoring toward the right prediction (x_i, c_i). Note that when $g(i) = 0$, the weights remain unchanged, since there is no need to update the model when the prediction is right. Each update step corresponds to a seen example in the training set. A full epoch of training is achieved when we have iterated through all the examples. The model is guaranteed to achieve idempotence, i.e. $g(i) = 0,\ 1 \leq i \leq n$, after a finite number of epochs if the training set is linear separable [8]. In practice, though, full separability is not

necessary, and sometimes not even desired due to overfitting, and thus the number of epochs may be limited, while maintaining good results [2].

2.1.2 Structured Perceptron

Consider now that the problem does not consist of classifying a single example x, but a sequence described by a m-dimensional vector $\mathbf{X} = [x_1 \dots x_m]$. The probable classifications may be represented by a class vector $\mathbf{C} = [c_1 \dots c_m]$, respectively, associated. In a first glance, we may apply the Perceptron algorithm over those vectors, with a new cost function $F(\mathbf{X}, \mathbf{C})$ and a decision function $\hat{\mathbf{C}}(\mathbf{X})$. However, due to the exponential growth of possible class vectors $\mathbf{C}$ in terms of m, this kind of classification becomes rapidly intractable.

To reduce the search space, we assume that any prediction $c_j, 1 \leq j \leq m$, has dependency on a finite number of previous predictions. In the trivial case, where c_j is not dependent on any other prediction, the cost function is defined as:

$$F(\mathbf{X}, \mathbf{C}) = \sum_{j=1}^{m} f(x_j, c_j), \tag{7}$$

We may then define the decision function $\mathbf{X}$ as:

$$\hat{\mathbf{C}}(\mathbf{X}) = arg\,min_{\mathbf{C}}(F(\mathbf{X}, \mathbf{C})), \tag{8}$$

and, by Eq. (7), we conclude that:

$$\hat{\mathbf{C}}(\mathbf{X}) = [\hat{c}(x_1) \dots \hat{c}(x_j)], \tag{9}$$

since the minimum sum of $f(x_j, c_j)$ is the sum of the minimums themselves.

Since the vector $\mathbf{X}$ is an argument, and thus does not belong to the search space, it is possible to further modify the Eq. (7) to:

$$F(\mathbf{X}, \mathbf{C}) = \sum_{j=1}^{m} f(\mathbf{X}, c_j). \tag{10}$$

Which means it is possible to define a class c_j in terms of the whole vector $\mathbf{X}$, and not only in terms of a local term x_j.[1] Equation (9) remains equally valid for this case.

[1]This implies in an important property from the Structured Perceptron, which is being able to observe all the elements of the structure, and no only the local ones. This property is emphasized by Collins [3] when the so called *Global Linear Models* are defined.

However, if c_j depends on k prior terms, the cost function in (10) should be modified to:

$$F(\mathbf{X}, \mathbf{C}) = \sum_{j=1}^{m} f\big(\mathbf{X}, [c_{j-k} \ldots c_j]\big), \tag{11}$$

which renders the minimization cost function (8) nontrivial. However, storing the cost history computed by the local functions $f(\mathbf{X}, [c_{j-k} \ldots c_j])$, enables the minimization in polynomial time through the well-known Viterbi algorithm [2].

2.1.3 Averaged Perceptron

A modification in the algorithm proposed by Collins [2] addresses a potential problem in the learning process. Suppose that, in a given iteration, the model is so good that, during the training, it predicts correctly all the examples, except the last one. In this last example, the prediction fails and the update is triggered. Consequently, the final model starts making more mistakes in the previous examples.

Formalizing the aforementioned example, it can be described the following way: in the $n-1$ first examples, the initial values of $\mathbf{w}$ suffice, and in the Eqs. (4), (5) and (6), the model never updates until the nth example. In this last example, the update step changes the values of $\mathbf{w}$, and the final accuracy of the model drops.

To avoid this problem, we store the $\mathbf{w}_i$ weights computed in each example. In the end of each training epoch, the stored vectors are averaged:

$$\mathbf{w} \leftarrow \sum_{i=1}^{n} \frac{\mathbf{w}_i}{n}. \tag{12}$$

It should be noted that there is no need to physically store all vectors. By the equation, there is only the need to store a single vector, which is incremented example by example. The discussion about the convergence speedup as consequence of this method is given by Collins [2].

2.1.4 Parameter Mixing Parallelization

The structured perceptron is an online learning algorithm which updates the weight vector $\mathbf{w}$ example by example. Implementing a parallel algorithm which is strictly equivalent to the sequential one is not a trivial task.

Thus, we have chosen the parallelization strategy proposed by Mcdonald et al. [6]. This algorithm is entirely data parallel, as it calculates the average weights of independently trained models.

Suppose we have P different partitions from the training set, randomly generated in the beginning of each epoch. For each partition P, we train a separate model with its weight vector $\mathbf{w}_p$. In the end of each epoch, all weight vectors are mixed by a simple consensus criterion:

$$\mathbf{w} \leftarrow \sum_{p=1}^{P} \frac{\mathbf{w}_p}{n}. \tag{13}$$

Since this equation may be confused with Eq. (12), we distinguish the notions of parameter averaging and parameter mixing. The first refers to the average of weight vectors computed example by example, which may be done sequentially. The second refers to the average of weight vectors from different models.

3 *Mac-Morpho Revisited* Corpus

Mac-Morpho is a text corpus extracted from the *Folha de São Paulo* newspaper [1]. The corpus had a first automated labeling with part-of-speech tags, and further corrected manually. Even with this revision, the corpus still has issues. A new version (*Mac-Morpho Revisited*), made available by Fonseca and Rosa [5], addresses some of this issues, and this version was used for training and testing in this work.

In its revised version, the corpus has approximately a million words and 50,000 sentences. The tag set has 30 different labels, which is less than half the amount of labels from the original Mac-Morpho. The revision discarded exclusive tags for each kind of punctuation, complex tag composition rules, and splitting of preposition contractions and combinations.

3.1 Feature Vector

We define the feature vector of a sentence $\mathbf{X}$ as $\mathbf{h}(\mathbf{X}, c_k)$, being c_k the label of each token k from the sentence. This vector is the same used by Ratnaparkhi [7], except we do not make the distinction between rare and non-rare words. This means that regardless of the word occurence, we extract features regarding:

- existence of uppercase characters, numbers, or hyphenation
- suffixes and prefixes of length 4,
- word context (two words ahead and behind, and the word itself),
- tag history (last two tags).

The expected sparsity of $\mathbf{h}$ is used to optimize the dot product described in Eq. (1).

3.2 Parallelism Test

For parallelism analysis and its performance impacts, experiments with different number of partitions were made. We chose the values $P = \{1, 8, 12, 16, 24\}$. All the tests were made in a 12-core machine with Hyper Threading (with 24 logical cores), with 64 GB of RAM.

In those tests, the *Mac-Morpho Revisited* corpus was divided in a validation set of nearly 100 thousand words, a test corpus of similar size, and a training corpus with the 800 thousand remaining words.

3.3 Accuracy Test

For the final accuracy test, we define another test setting in which the *Mac-Morpho Revisited* corpus was split according to Fonseca and Rosa [5]. The training set was composed by nearly 900 thousand words, and the test nearly 100 thousand. To measure the quality of the resulting models, we use the accuracy per word (i.e., number of right predictions by the total number of words) and the accuracy per out-of-vocabulary word (OOV, words seen in the test set, but unseen in the training set).

4 Results

4.1 Parallelism

The plots from Fig. 1 were obtained from the parallel training simulations. We observe that the number of epochs of training needed to achieve convergence and the number of partitions used in parallel training are sublinearly correlated. In the case of 24 partitions, convergence is suboptimal. Such behavior was expected, since it is similar to the observed by Mcdonald et al. [6] for the English language.

Table 1 shows the accuracy for the validation set given a specific number of training epochs. For $P = 1$, the chosen epoch was the one which presented the maximum accuracy. On the remaining cases, we chose a number of epochs in which the accuracy was closest to the single partition case. In the 24 partition case, since its convergence was suboptimal, we chose an arbitrarily large value of epochs.

Table 2 shows the training times for each test case from Table 1. We note that there is a maximum relative speedup of 2.45 times for the 8 partition case. There is a great speedup degradation after the 12 partition case, for which we have three hypotheses which may explain such effect:

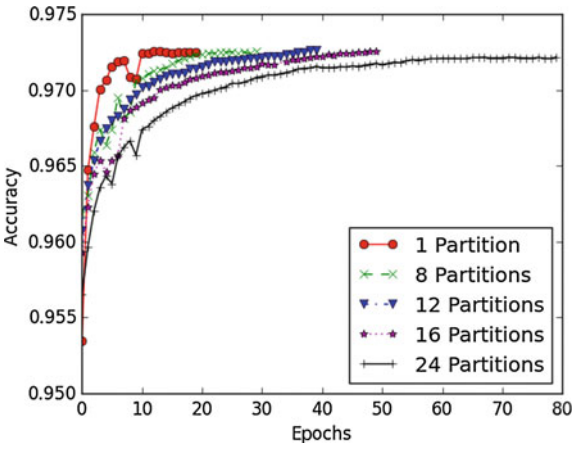

Fig. 1 Convergence curves for each number of partitions in the training set

Table 1 Accuracy for the validation set

Model	Acc (%)	Acc OOV (%)	Epochs
1 Partition	97.26	93.22	13
8 Partitions	97.26	93.00	30
12 Partitions	97.26	92.96	40
16 Partitions	97.26	93.02	50
24 Partitions	97.21	92.77	70

Table 2 Training time for each model

Model	Time per epoch	Total time
1 partition	61 min 28 s	798 min 58 s
8 partitions	10 min 10 s	304 min 56 s
12 partitions	7 min 49 s	312 min 22 s
16 partitions	8 min 18 s	415 min 34 s
24 partitions	8 min 43 s	610 min 28 s

- **Data heterogeneity**: each training epoch has its time lower bounded by the partition, which delays the most. If the data is not split homogeneously enough between the cores, one of them may have a processing time significantly higher than the others.
- **Parameter mixing overhead**: the parameter mixing step is made in a single thread, and thus, it is indifferent to the paralellism.
- **Usage of logic cores** (***hyper threading***): each logic core may not significantly contribute to the parallelization.

As a last note, it is important to emphasize the linear memory usage in terms of the number of partitions, though this problem was not further addressed in this work. McDonald, Mann and Hall [6] cite memory limitations in their experiment.

Table 3 Accuracy for the test set

Model	Acc (%)	Acc OOV (%)	Epochs
Baseline	96.48	87.34	–
1 partition	97.09	91.61	13
8 partitions	97.07	91.48	30
12 partitions	97.07	91.57	40
16 Partitions	97.04	91.14	50
24 partitions	97.06	91.42	70

4.2 Accuracy per Word

The accuracy per word was measured over the test set. The results for each model may be seen in Table 3. The results for the Structured Perceptron, both in the single and multiple partition cases, surpass the 97% accuracy in the test corpus, achieving state-of-the-art for purely supervised training [4].

When comparing the results with our baseline [5], it is important to note the expressive gains in OOV accuracy. In their work, Fonseca and Rosa explain that the unsupervised features generated by their neural network did not show the expected gains for unseen words. This shows that binary handcrafted features still have advantages over inferred word embeddings for out-of-vocabulary words.

5 Conclusion

We presented the results for the Averaged Perceptron described by Collins [2] and its parallel implementation by Mcdonald et al. [6]. We have shown that the performance of both implementations is similar to the state of the art in the field. We also addressed the efficiency limitations of the algorithm through a parallelized implementation with a maximum speedup of 2.45 times for the 8-partition case.

In the future, it would be interesting to test new feature extraction techniques as a mean to couple the algorithm with unsupervised training strategies, aiming to further improve the accuracy of the models.

References

1. Aluisio S, Pelizzoni J, Marchi AR, de Oliveira L, Manenti R, Marquiafável V (2003) An account of the challenge of tagging a reference corpus for brazilian portuguese. In: Proceedings of computational processing of the Portuguese language. Springer, pp 110–117
2. Collins M (2002) Discriminative training methods for hidden markov models: theory and experiments with perceptron algorithms. In: Proceedings of the ACL-02 conference on empirical methods in natural language processing, vol 10. Association for computational linguistics, pp 1–8

3. Collins M (2013) Natural language processing. https://www.coursera.org/course/nlangp. Accessed 05 2013
4. Dos Santos CN, MIlidiú RL, Rentera RP () Portuguese part-of-speech tagging using entropy guided transformation learning. Avaiable in Computational processing of the portuguese language. Springer, pp 143–152
5. Fonseca ER, Rosa JLG (2013) Mac-morpho revisited: towards robust part-of-speech tagging. In: Proceedings of the 9th Brazilian symposium in information and human language technology, pp 98–107
6. Mcdonald R, Hall K, Mann G (2010) Distributed training strategies for the structured perceptron. In: Proceedings of human language technologies: the 2010 annual conference of the north American chapter of the association for computational linguistics. Association for computational linguistics, pp 456–464
7. Ratnaparkhi A (1996) A maximum entropy model for part-of-speech tagging. In: Proceedings of the conference on empirical methods in natural language processing, vol 1. pp 133-142
8. Rojas R (1996) Neural networks: a systematic introduction. Springer science & business media
9. ACL WIKI. Pos tagging (state of the art). http://wiki.aclweb.org/. Last modified in 26 Nov 2014

Exploring Convolutional Neural Networks for Voice Activity Detection

Diego Augusto Silva, José Augusto Stuchi, Ricardo P. Velloso Violato and Luís Gustavo D. Cuozzo

Abstract This paper presents a voice activity detection (VAD) method based on convolutional neural networks (CNN). The proposed method uses the audio spectrogram raw image to detect frames of voice in specific audio signal. The spectrogram is split into frames, each of which is classified according to the presence or absence of voice. The proposed method achieved high accuracy in different noise conditions and was compared to state-of-the-art VAD methods. It outperforms the best VAD systems with a significant improvement in half-total error rate (HTER) when tested on the QUT-NOISE-TIMIT database. This technique indicates that using CNN on audio spectrogram images can be an efficient way for detecting voice even in extremely noisy audio signals.

1 Introduction

Voice activity detection (VAD) is an important step performed in speech processing applications, where an audio signal is analyzed in order to distinguish which parts contain conversational speech and which parts contain only background noise. In applications such as speech recognition [18], speaker diarization [25], speaker recognition [22] or speech coding [3] its goal is to discard the non-speech portions of the signal. In the context of speech enhancement applications, it can be used to estimate and model the noise spectrum which will be used to improve the original audio [11].

D.A. Silva (✉) · J.A. Stuchi · R.P.V. Violato · L.G.D. Cuozzo
CPqD Foudation, Campinas, São Paulo, Brazil
e-mail: diegoa@cpqd.com.br

J.A. Stuchi
e-mail: jastuchi@cpqd.com.br

R.P.V. Violato
e-mail: rviolato@cpqd.com.br

L.G.D. Cuozzo
e-mail: lcuozzo@cpqd.com.br

A. Paradisi et al. (eds.), *Cognitive Technologies*, Telecommunications and Information Technology, DOI 10.1007/978-3-319-53753-5_4

In this scenario, a variety of VAD algorithms were developed. The typical methods perform a feature extraction step and, after that, a classification step to classify if a given signal frame contains active voice or not. As described in [10], it is possible to name many VAD features such as energy, cepstral coefficients, zero crossing rate, high order spectra, LPC analysis, autocorrelation, and spectral divergence. These features can also be combined in order to improve results.

Regarding the classification step, the applied methods range from simple techniques, such as using tunable thresholds [12] or basic statistical modeling [23], to more complex classifiers such as hidden Markov models (HMM) [25], Gaussian mixture models (GMM) [2], support vector machines (SVM) [21, 26] and, more recently, Deep Neural Networks (DNN) [27, 28].

Modern VAD algorithms usually perform very well in low noise scenarios, but they may fail when the signal is too noisy. In this case, the development of noise robust algorithms is necessary. For example, in speech recognition applications, if part of the word pronounced is not detected by the VAD, the word will not be understood by the automatic speech recognition (ASR) algorithm, which may cause semantic losses in natural language processing (NLP) applications. In a noisy scenario, for example, with signal-to-noise ratio (SNR) lower than 5 dB, advanced techniques should be used to build high accuracy VAD algorithms in order to avoid misclassification.

Speech can be broadly classified into two different groups, according to the nature of excitation of the vocal cords or folds. In voiced speech, the air flow from the lungs vibrates the vocal folds, while in unvoiced speech there is no use of the vocal folds. Current VAD implementations are more successful in detecting voiced speech frames rather than unvoiced speech frames [10]. This happens mainly because of the statistical nature of unvoiced speech, which is more random than voiced frames and similar to background noise [8, 15]. Human voiced frames have a quasi-periodic nature that makes it different from unvoiced speech and more robust to background noise [7].

Figure 1 shows an example where it is possible to see a spectrogram with background noise, voiced and unvoiced speech. Since the differences among these three regions are visible in the spectrogram (as it is possible to notice in Fig. 1), some

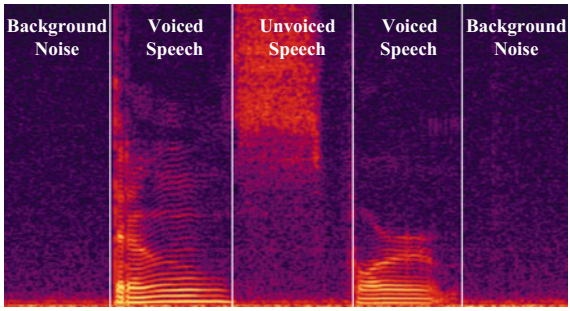

Fig. 1 Segmented spectrogram showing noise, voiced, and unvoiced speech regions

image processing techniques can be applied in order to detect voice activity, i.e., separating background noise from conversational speech.

In this context, different works were already proposed aiming to process the audio spectrogram using different image processing techniques [4, 14, 19]. One of the main approaches is based on convolutional neural networks (CNN) [16]. Some results obtained using CNN in speech recognition [1, 6], speaker recognition [20], and language identification [9] problems show promising results. Regarding the VAD problem, CNN also showed interesting results as presented in [24], but this approach pre-processed the spectrogram, converting it to log mel-scale. After that, it extracted coefficients and the signal derivatives (delta and delta-delta). The result of this pre-processing step is used as the CNN input. In the current approach presented in this paper, the raw spectrogram is processed directly by the CNN, simplifying the feature extraction and training steps. Moreover, the current approach was validated using large VAD datasets.

This was the motivation behind the CNN-based VAD presented in this paper. A new method for voice activity detection using CNN was proposed and evaluated using the QUT-NOISE-TIMIT database [5], which consists of 600 h of noisy speech sequences in different background noise scenarios.

This paper is organized as follows: Sect. 2 describes the neural network architecture used in this work. Sections 3 and 4 present the proposed method and the experiments conducted to assess it. Section 5 exhibits achieved results and discusses them. Finally, Sect. 6 presents conclusions and future work perspectives.

2 CNN Architecture

CNNs are a special kind of deep neural network, originally designed to recognize visual patterns directly from pixel images with minimal pre-processing [17]. It was basically developed to operate over images, but the same idea can be adapted to the speech processing field, usually using a time–frequency representation of the audio signal as the "image".

What differs a CNN from other deep architectures is its layers structure, consisting of alternating so-called convolution and pooling layers [17], which can be seen as a feature extraction module. These networks can recognize patterns with extreme variability and they are robust against distortions and simple geometric transformations.

The CNN used in this paper is based on LeNet 5 [17], created to recognize handwritten and machine-printed character. Figure 2 shows the architecture adopted in this study.

LeNet 5 CNN used is a 8-layer network with 2 convolutional layers, 2 pooling layers, 2 fully connected layers, a rectified linear unit (ReLU) layer and a softmax regression layer with 2 output classes. The network operates over the raw audio spectrogram, split in frames, without any feature extraction step, which is automatically performed by the network and can be seen in the resultant features maps. Section 3

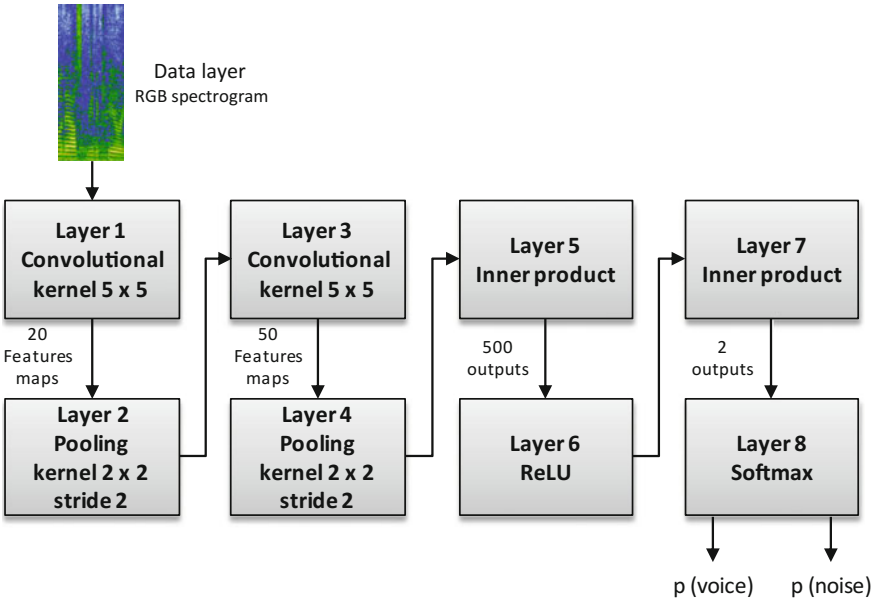

Fig. 2 CNN architecture inspired on LeNet 5 [17]

describes how the spectrogram is obtained and fed into the network. Regarding network output, the softmax layer returns two outputs meaning the probability of voice activity and the probability of background noise for the frame presented to the network to be classified.

3 Method

The basic idea behind the proposed method is that a human expert is able to distinguish among speech and nonspeech parts of an audio recording just by looking at its spectrogram. This is possible because speech usually produces a time–frequency pattern that is different from nonspeech, especially on voiced parts, where the harmonics of the fundamental frequency and the vocal tract resonances are clearly visible. So if there is an artificial neural network that is capable of emulating human vision, it can be trained to perform the VAD task.

Based on this idea, one can use a spectrogram to predict where there is speech in a given signal. Figure 3 displays the flowchart of the proposed method. To generate a spectrogram, an available online toolkit was used.[1] In this paper, each 160 ms audio signal block became a 32×128 pixel spectrogram image (RGB), and an image was

[1] https://github.com/ljvillanueva/Sound-Viewer-Tool.

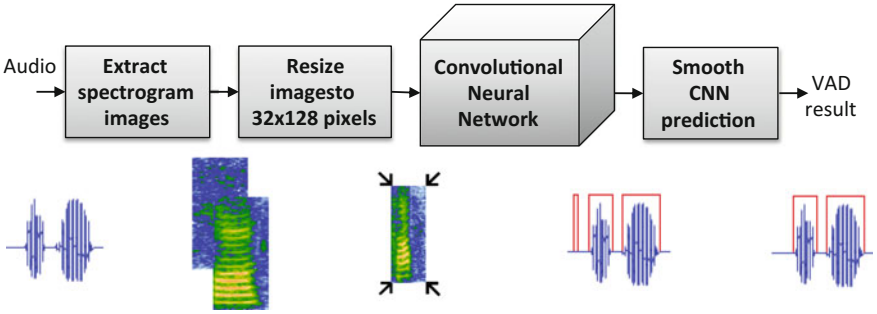

Fig. 3 Schematic of proposed VAD

generated every 80 ms. Following the experimental protocol (see Sect. 4.2), these images will be individually classified as background noise or conversational speech.

The colormap adopted in this work to generate the spectrogram images ranges from a light blue, in the low energy regions, to green and yellow, in the high energy regions, with a white background, thus giving a good contrast and visualization for the frequency ridges and valleys. By convention the final spectrogram has low frequencies on the bottom and high frequencies on the top of the image. Figure 2 shows an example of such a spectrogram.

The image size was chosen in order to provide a good trade-off between good spectrum visibility and low resolution. The lower the resolution, the less the number of parameters to be tuned in the CNN. The resolution, however, should be high enough to keep the spectrum voice characteristics visible.

Given these characteristics, every audio file in the QUT-NOISE-TIMIT database was converted to a set of spectrogram images. It is important to note that, for the training data, when the 160 ms signal block encompasses a transition from/to speech/nonspeech, the 80 ms step was adjusted to keep each block belonging to only one class.

As described in Sect. 2, a CNN was then trained generating a prediction model from scratch and without pretrained models, using 0 to represent background noise and 1 to voice activity. The training process uses NVIDIA®Digits 3.2.0 with Caffe framework 0.14.2 [13]. Default Digits configuration for LeNet 5 was applied with minimal customization: scale factor of $1/256$ and 2 outputs (background noise or converetcsational voice). 15 epochs were used for training CNN parameters and 75% of the images available training data was used for training and 25% for validation. A learning rate of 0.01 on the stochastic gradient descent (SGD) and L2 weight decay of 0.0001 was used.

As it is not expected that there is a single speech block surrounded by nonspeech and vice versa, a post-processing technique was also applied in order to smooth the prediction results, aiming to minimize classification errors. In this case, the final result for each signal block is the average of the predictions of its two previous and two posterior neighbors, and the block under analysis itself.

Once a new sequence of spectrogram images is presented to the network and its outputs are smoothed, the final decision is taken based on a predefined threshold. The threshold was computed in order to minimize half-total error rate (HTER) on the training data, as described in Sect. 4.2, based on the network output that represents voicing probability.

4 Experiment Description

4.1 Database

The experiments conducted in order to evaluate the proposed technique were based on the QUT-NOISE-TIMIT database, a large-scale corpus originally designed to enable a thorough evaluation of VAD algorithms.

The QUT-NOISE-TIMIT database was created by adding realistic noise recordings from the QUT-NOISE corpus to the clean speech from the TIMIT database. It consists of 600 h of noisy speech over 24,000 files created at set lengths of 60 and 120 s and at 6 different SNR. The noise recordings were collected from 10 independent real-noise locations, in 2 sessions, each of them belonging to one of 5 distinct scenarios. The final noisy speech files have a 16,000 Hz sampling rate and 16 bits per sample.

The database is organized so that for each noise level, noise location, and utterance duration, there is the same number of files, 200. Tables 1 and 2 summarize the corpus. Table 1 illustrates one of the 5 scenarios, named "HOME", and the same applies to all other 4 scenarios, described in Table 2.

Additionally to the audio files, QUT-NOISE-TIMIT database also provides metadata with the speech versus nonspeech time marking, i.e., every signal sample in the database is labeled as speech or nonspeech, thus providing the ground truth for VAD experiments.

4.2 Protocol and Evaluation Metric

According to the proposed protocol [5] speech files from three different noise levels were grouped to perform the tests: low noise (SNR = 10 or 15 dB), medium noise (SNR = 0 or 5 dB), and high noise (SNR = −5 or −10 dB). We trained a different CNN model for each of these groups. Still, according to the protocol, the VAD method was trained using data from one location group (A or B) and tested on the other (B or A), and vice versa, in such a way that, although there is training data from all scenarios, there is no prior knowledge of the actual locations.

Table 1 QUT-NOISE-TIMIT properties for HOME scenario

Scenario	Location	SNR (dB)	Duration (s)	# Files
HOME	Kitchen	15	60	200
			120	200
		10	60	200
			120	200
		5	60	200
			120	200
		0	60	200
			120	200
		−5	60	200
			120	200
		−10	60	200
			120	200
	Living room	15	60	200
			120	200
		10	60	200
			120	200
		5	60	200
			120	200
		0	60	200
			120	200
		−5	60	200
			120	200
		−10	60	200
			120	200

Table 2 QUT-NOISE-TIMIT scenarios and locations

Scenarios	Location A	Location B
Cafe	Food court	Cafe
Car	Window down	Window up
Home	Kitchen	Living room
Reverb	Pool	Car park
Street	City	Suburb

The evaluation metrics employed are the miss rate (MR), when the method predicts no speech, but there is speech, false alarm rate (FAR), when the method predicts speech where there is no speech, and the half-total error rate (HTER), which is the average of FAR and MR.

The following equations define how to compute the MR, FAR and HTER, which are expressed in percentages.

$$\text{MR} = \frac{\textit{Number of speech samples not detected as speech}}{\textit{Total number of speech samples}} \times 100 \quad (1)$$

$$\text{FAR} = \frac{\textit{Number of nonspeech samples detected as speech}}{\textit{Total number of nonspeech samples}} \times 100 \quad (2)$$

$$\text{HTER} = \frac{\text{MR} + \text{FAR}}{2} \quad (3)$$

5 Results and Discussion

As described in Sect. 4.2, HTER was used to evaluate the proposed algorithm. The five baseline systems evaluated in [5] (ETSI, G729B, Sohn, LTSD, GMM-MFCC-1), along with the method presented in [11], which will be named GMM-MFCC-2, were used to compare with the method proposed in this work.

The results of the seven VAD systems are shown according to the their HTER in Fig. 4. The results are presented in three broad noise levels according to QUT-NOISE-TIMIT protocol: low noise (SNR 10 to 15 dB); medium noise (SNR 0 to 5 dB); and high noise (SNR −10 to −5 dB).

The CNN-VAD system proposed in this work outperforms the evaluated baseline systems in all noise conditions. For the low noise condition, the proposed method reached a HTER of 3.2%, which is quite a significant improvement. For the medium and high noise conditions, the HTER was 8.0% and 14.5%, respectively, which are also better than the best reported results, as shown in Fig. 4. Table 3 details these results in terms of its MR and FAR. Furthermore, the proposed method could be easily tuned to prioritize false alarms or misses just by changing the threshold, thus giving flexibility to specific applications to find its optimal operation point.

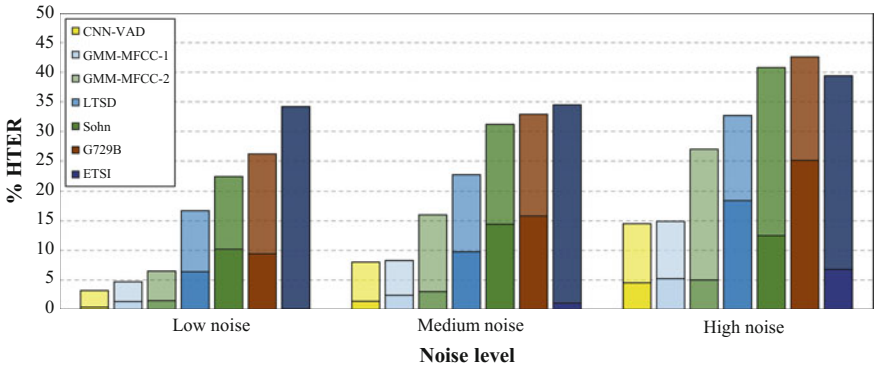

Fig. 4 HTER performance over all VAD systems. Each bar represents the HTER in percentage. The MR and FAR contributions to the total error can also be seen in this figure, shown in *dark* and *light tones*, respectively

Table 3 Detailed results. A → B means the network was trained on A and tested on B, and B → A is the opposite. All results are expressed as percentages

SNR	A → B		B → A	
	MR	FAR	MR	FAR
Low noise	0.4	2.3	0.4	3.3
Medium noise	0.9	7.3	2.0	5.8
High noise	4.0	10.7	5.0	9.3

These results demonstrate that CNN can be used for speech activity detection tasks and have a high potential to be explored in audio processing applications.

6 Conclusion

In this work a VAD method was presented. The method is based on a CNN, a special case of a deep neural network, designed to recognize image patterns. In the speech processing field, this approach uses a time–frequency representation of the audio signal as the "image" to perform the desired task.

The proposed CNN architecture was inspired by the LeNet 5 and the audio time–frequency representation (spectrogram) was split in frames and used as network inputs for training and classification. The method was tested on the QUT-NOISE-TIMIT database, a large noisy speech database created to assess VAD techniques on a wide variety of noise scenarios and SNR.

The results present a improvement over the state-of-the-art performance reported in the literature. An expressive improvement in low noise scenario, reaching a 3.2% HTER, was achieved and also some improvement in medium and high noise conditions, with a HTER of 8.0% and 14.5%, respectively.

Since the default LeNet 5 architecture developed for handwritten character recognition was used, there is huge room for improvement if one were to design a specific network architecture for voice activity detection activities.

Moreover, there are some directions for future work that can lead to better results. The authors aim to test different ways to generate the spectrogram (frame size, frame step, window function, and FFT size) and different colormaps. Finally, one important improvement would be to train a single network, regardless the SNR of the input signal, which in real-life conditions would usually be unknown.

References

1. Abdel-Hamid O, Deng L, Yu D (2013) Exploring convolutional neural network structures and optimization techniques for speech recognition. In: INTERSPEECH, pp 3366–3370
2. Abdulla WH, Guan Z, Sou HC (2009) Noise robust speech activity detection. In: 2009 IEEE international symposium on signal processing and information technology (ISSPIT). IEEE, pp 473–477
3. Benyassine A, Shlomot E, Su HY, Massaloux D, Lamblin C, Petit JP (1997) Itu-t recommendation g. 729 annex b: a silence compression scheme for use with g. 729 optimized for v. 70 digital simultaneous voice and data applications. IEEE Commun Mag 35(9):64–73
4. Costa Y, Oliveira L, Koerich A, Gouyon F (2013) Music genre recognition based on visual features with dynamic ensemble of classifiers selection. In: 2013 20th international conference on systems, signals and image processing (IWSSIP). IEEE, pp 55–58
5. Dean DB, Sridharan S, Vogt RJ, Mason MW (2010) The qut-noise-timit corpus for the evaluation of voice activity detection algorithms. Proceedings of interspeech 2010
6. Deng L, Hinton G, Kingsbury B (2013) New types of deep neural network learning for speech recognition and related applications: an overview. In: 2013 IEEE international conference on acoustics, speech and signal processing (ICASSP). IEEE, pp 8599–8603
7. Eom KB, Chellappa R (1994) Classification of voiced and unvoiced speech by hierarchical stochastic modeling. In: Proceedings of the 12th IAPR international conference on pattern recognition, 1994, vol 3-conference c: signal processing. IEEE, pp 20–24
8. Fisher E, Tabrikian J, Dubnov S (2006) Generalized likelihood ratio test for voiced-unvoiced decision in noisy speech using the harmonic model. IEEE Trans Audio Speech Lang Process 14(2):502–510
9. Ganapathy S, Han KJ, Thomas S, Omar MK, Van Segbroeck M, Narayanan SS (2014) Robust language identification using convolutional neural network features. In: INTERSPEECH, pp 1846–1850
10. Ghaemmaghami H, Baker BJ, Vogt RJ, Sridharan S (2010) Noise robust voice activity detection using features extracted from the time-domain autocorrelation function. Proceedings of interspeech 2010
11. Ghaemmaghami H, Dean D, Kalantari S, Sridharan S, Fookes C (2015) Complete-linkage clustering for voice activity detection in audio and visual speech
12. Ghaemmaghami H, Dean D, Sridharan S, McCowan I (2010) Noise robust voice activity detection using normal probability testing and time-domain histogram analysis. In: 2010 IEEE international conference on acoustics speech and signal processing (ICASSP). IEEE, pp 4470–4473
13. Jia Y, Shelhamer E, Donahue J, Karayev S, Long J, Girshick R, Guadarrama S, Darrell T (2014) Caffe: convolutional architecture for fast feature embedding. arXiv preprint arXiv:1408.5093
14. Kobayashi T, Ye J (2014) Acoustic feature extraction by statistics based local binary pattern for environmental sound classification. In: 2014 IEEE international conference on acoustics, speech and signal processing (ICASSP). IEEE, pp 3052–3056
15. Kristjansson T, Deligne S, Olsen P (2005) Voicing features for robust speech detection. Entropy 2(2.5), 3
16. LeCun Y, Bengio Y (1995) Convolutional networks for images, speech, and time series. Handb Brain Theor Neural Netw 3361(10):1995
17. LeCun Y, Bottou L, Bengio Y, Haffner P (1998) Gradient-based learning applied to document recognition. Proc IEEE 86(11):2278–2324
18. Li JY, Liu B, Wang RH, Dai LR (2004) A complexity reduction of etsi advanced front-end for dsr. In: IEEE international conference on acoustics, speech, and signal processing, 2004. Proceedings.(ICASSP'04), vol 1. IEEE, pp I–61
19. Markel JD (1972) The sift algorithm for fundamental frequency estimation. IEEE Trans Audio Electroacoust 20(5):367–377
20. McLaren M, Lei Y, Scheffer N, Ferrer L (2014) Application of convolutional neural networks to speaker recognition in noisy conditions. In: INTERSPEECH, pp 686–690

21. Ramırez J, Yélamos P, Górriz J, Segura J (2006) Svm-based speech endpoint detection using contextual speech features. Electron Lett 42(7):877–879
22. Reynolds D (2002) An overview of automatic speaker recognition. In: Proceedings of the international conference on acoustics, speech and signal processing (ICASSP), S 4072, p 4075
23. Sohn J, Kim NS, Sung W (1999) A statistical model-based voice activity detection. IEEE Signal Process Lett 6(1):1–3
24. Thomas S, Ganapathy S, Saon G, Soltau H (2014) Analyzing convolutional neural networks for speech activity detection in mismatched acoustic conditions. In: 2014 IEEE international conference on acoustics, speech and signal processing (ICASSP). IEEE, pp 2519–2523
25. Wooters C, Huijbregts M (2008) The icsi rt07s speaker diarization system. In: Multimodal technologies for perception of humans. Springer, pp 509–519
26. Wu J, Zhang XL (2011) Efficient multiple kernel support vector machine based voice activity detection. IEEE Signal Process Lett 18:466–469
27. Zhang XL, Wu J (2013) Deep belief networks based voice activity detection. Proc IEEE 21(4):697–710
28. Zhang XL (2014) Unsupervised domain adaptation for deep neural network based voice activity detection. In: 2014 IEEE international conference on acoustics, speech and signal processing (ICASSP). IEEE, pp 6864–6868

Part II
Cognitive Technologies Applied to Wireless Networks

4G/LTE Networks for Mission-Critical Operations: A Cognitive Radio Approach

J.J. Bazzo, S. Barros, R. Takaki, D. Carrillo and J. Seki

Cognitive radio is an advanced technology being used to improve the efficiency of spectrum usage, as well as to sense the environment and change its radio parameters to avoid interference with primary users (PU) or secondary users (SU). This strategy can also be applied to avoid jamming interference in military defense networks. Also, while LTE (Long-Term Evolution) technology has been successfully deployed worldwide for broadband civil applications, it has also evolved to support Public Safety and National Defense applications. Security and QoS (Quality of Service) features have proven to be especially useful when applied to the Defense sector, but fail to provide protection against intentional jamming attacks, which can interrupt OTA (Over-the-Air) communications. So far, there is no formal 3GPP (3rd Generation Partnership Project) report addressing the jamming issue, although mechanisms to mitigate OTA vulnerabilities have been proposed in the literature, mainly by authors suggesting changes in the LTE physical layer standard. This paper presents two innovative strategies based on cognitive radio technology to prevent jamming attacks, without the need to implement changes in the 3GPP standard or in the base station/terminal hardware. These advantages can accelerate the deployment and reduce the costs using the same

J.J. Bazzo (✉) · S. Barros · R. Takaki · D. Carrillo · J. Seki
CPqD Foundation, Campinas, São Paulo, Brazil
e-mail: jbazzo@cpqd.com.br

S. Barros
e-mail: sbarros@cpqd.com.br

R. Takaki
e-mail: rtakaki@cpqd.com.br

D. Carrillo
e-mail: dickm@cpqd.com.br

J. Seki
e-mail: jseki@cpqd.com.br

A. Paradisi et al. (eds.), *Cognitive Technologies*, Telecommunications and Information Technology, DOI 10.1007/978-3-319-53753-5_5

infrastructure equipment. A computational simulation is performed in order to compare scenarios involving Cell Frequency Reconfiguration and Frequency Hopping Strategies. Performance results are shown considering video streaming service with different jamming scenarios.

1 Introduction

LTE technology is extremely vulnerable to malicious attacks, partly because it has been designed to operate as the primary system in the spectrum usage. On the other hand, the cognitive radio technology is able to work harmoniously with primary and secondary systems, making use of spectrum sensing techniques and other intelligent algorithms. Therefore, combining the cognitive radio approach with LTE technology to avoid jamming attacks seems to be an innovative solution. LTE has achieved significant improvements in data transmission capacity, as well as in reaching higher spectral efficiency, higher peak data rates and low-latency transmission, while providing simplified IP-based network architecture with open interfaces and greater frequency flexibility, channel bandwidths, and service provisioning.

Since its inception, 3GPP has paid due attention to security issues. This approach resulted in a strong set of tools to protect the confidentiality and the integrity of all LTE network elements, using cryptography and authentication techniques. At lower layers, to improve the availability of LTE system and provide robustness to data transmission, LTE already supports some techniques to mitigate interference [1, 2] but they are not efficient enough to ensure the availability of LTE over-the-air sessions under strong jamming interference. As a result, many studies on jamming mitigation emerged to enable the usage of LTE systems in military applications. Some papers have addressed jamming consequences in physical layer channels, such as PDCCH (Physical Downlink Control Channel), PUCCH (Physical Uplink Control Channel), RS (Reference Signal), and PRACH (Physical Random Access Channel), without, however, reflecting real deployment scenarios [3–6].

This paper proposes two solutions to reduce the jamming effects, maintaining the base station, the terminal and the 3GPP standard unchanged. The first solution, the *Cell Frequency Reconfiguration* strategy, is based on the cell reconfiguration process, in which a new frequency band is assigned, and the second solution, the *Frequency Hopping* strategy, is able to switch the DC subcarrier frequency. From a practical implementation point of view, only the second strategy requires a firmware update, which is associated with the RF frequency selector to implement the hopping strategy. Some advantages of adopting this strategy are: (1) it makes new equipment acquisition unnecessary and (2) it enables remote software updates, thus simplifying maintenance procedures.

This paper highlights the main contributions and details of both proposed strategies. Frequency hopping strategy is inspired in the cognitive radio dynamic spectrum access, together with the LTE OFDM (Orthogonal Frequency-Division

Multiplexing) physical layer and scrambling techniques from 3GPP standard, aims at further increasing robustness against jamming attacks.

The cognitive mitigation strategy is based on RF (Radio Frequency) circuit reconfiguration on the BS (Base Station) and UE (User Equipment) side, and the hopping sequence selection.

This study considers a military tactical scenario with a complete LTE system located in a vehicle.

This paper is organized as follows. Section 2 presents LTE advantages for military applications; Sect. 3 explores LTE security features applied in the military context; Sect. 4 describes the experiment conducted to evaluate the jamming mitigation strategy and simulation results.

2 LTE Advantages for the Military

Nowadays, Military sector demands more applications that require mobility and broadband communication. In contrast with the scenario during the Cold War era [7], the military broadband communication technology is now outdated and is no longer ahead when compared to that used in other sectors, such as commercial telecommunications. Some army forces still use network technology from the 1970s or 1980s. The main reasons that drive the adoption of commercial solutions for the Military sector [7] are (a) costs, (b) life cycle and the feature set, which explains the high number of LTE Military-grade devices like tablets, smartphones, BS, and core network. Such equipment presents the same set of features as that of 3GPP, which offer compelling options for military applications [8–10]. A list of some benefits is presented below

- All-IP allowing a broad range of services like: Voice, IP Unicast data, IP Multicast data, and Short Message service;
- High spectral efficiency, from 2 to 3 times higher than the previous cellular technology;
- Low latency in the OTA interface with values around 10 ms;
- High data transmission rates with quality of service;
- Automatic modulation and power setting according to the quality of the signal received in the terminal;
- Frequency Selective Scheduling, Frequency Hopping (within the same channel) and distributed resource allocation, allowing frequency domain transmission diversity and protection against interference;
- The use of MIMO technology with spatial multiplexing to increase data transmission rates;
- The use of transmit diversity schemes to explore different multipath channel propagation;
- CA (Carrier Aggregation) of contiguous or fragmented spectrum to increase data transmission rates;

- Different Terminal classes that cover different requirements of cost, data transmission rates, and power saving.

LTE, LTE-A, and even future 5G technologies are evolving very quickly due to a strong role performed by both the standardization body and the research community. This evolution provides interesting features for the Military sector.

3 Military Scenario and LTE Security

LTE technology has been used by Public Safety and Public Services, such as the Law Enforcement authority, and, in some cases, by the National Defense Industry [11]. It is also used in crisis or mission-critical scenarios that require military intervention. In these cases, the network operators cannot be the primary solution, because of the low availability of network elements [12] and the lack of infrastructure necessary to operate in hostile environments. The main concern stands in the overload and weakness of over-the-air (OTA) communication, which can be easily degraded due to interferences or jamming attacks. In spite of a variety of LTE MIL-grade devices being made available with a number of technological advantages, vulnerability to jamming attacks represents a barrier for a wider application of LTE systems in the military.

3.1 Hostile Interference

The thread of jamming to battlefield communication consists of malicious radio signals generated to interfere in the receiver side of the opponent's wireless system —some sort of denial of service (DoS) attack. There are different types of jamming in wireless networks [3, 13, 14], ranging from elementary to advanced strategies. In [3], authors present a broad view of jamming in multiple wireless network technologies. Different jammer classes are mentioned: proactive jammers emit continuous random bits, and reactive jammers only transmit when the target wireless system is active, making it more difficult to detect and defend against, but, on the other hand, having a temporal penalty to detect and perform an analysis of the transmission before the attack occurs [15]. Function-specific jammers consist of a more advanced class of jammers that can hop over channels cyclically, thousand times per second, changing the pseudorandom hopping sequence. Smart-hybrid jammers [3] can perform a more sophisticated attack, placing a large amount of energy in some specific frequencies or subcarriers, just as those dedicated to transport the control information. In LTE, this type of jammer can even cancel uplink or downlink subcarriers allocated to control channels or reference signals.

Studies and proposed solutions to mitigate such vulnerabilities are presented in [3–6], however, they do not consider real deployment scenarios, in which attacks are not that effective. For instance, the jamming in the LTE downlink signal has to be performed on the UE side, because that is where the signal received is weaker. Then, as the UE is spread out across the battlefield, the jamming acts on multiple UE simultaneously, which proved to be an unfeasible approach. On the other side, LTE uplink jamming is easily deployed since the eNodeB is usually fixed/nomadic, the antenna is visible and the terminal transmission power is usually lower than 0.5 Watts. The mitigation strategy proposed in this paper is based on the uplink side, but it can also be applied to the downlink. LTE systems can usually be applied in the Defense or Military scenarios [16, 17] using the following configuration:

- **SOW—Systems On Wheels**: the eNodeB and EPC are co-located in a vehicle;
- **COW—Cell On Wheels**: vehicle with local eNodeB and remote EPC.

Since higher jamming vulnerability occurs at the uplink, we propose two mitigation strategies driven by cognitive radio techniques. The first strategy is based on the cell reconfiguration process in which a new frequency band is assigned, adding a significant delay to the process. The second strategy results in changes to the DC subcarrier frequency without causing any significant delay. Both are described in detail in the following subsections.

3.2 Description of Proposed Solutions

The proposed solutions aim at mitigating jamming attacks in SOW or COW scenarios of tactical military operations. Efficient spectrum usage was not considered in order to favor the hardening process and to provide higher availability. Additionally, spectrum availability is not known to be a common problem in greenfield deployments. The proposed simulation considers a single cell to serve a platoon of 15 soldiers spread out over an area of up to 3 km around the SOW. Each soldier holds a terminal and a camera to communicate with the Command Center. Figure 1 depicts this scenario.

The LTE system operates at the FDD Band 28 (Frequency-Division Duplex), divided into nine channels of 5 MHz each. The eNodeB is able to detect the jammer by using a SON (Self-Organizing Network) feature [18] and employing a similar technique as that of the Wireless Intrusion Detection System (WIDS) used in Wi-Fi or WLAN networks [19].

3.2.1 Strategy 1: Cell Frequency Reconfiguration

The first strategy is based on the cell frequency reconfiguration process, since the jamming is detected by the SON Controller. This reconfiguration implies a long

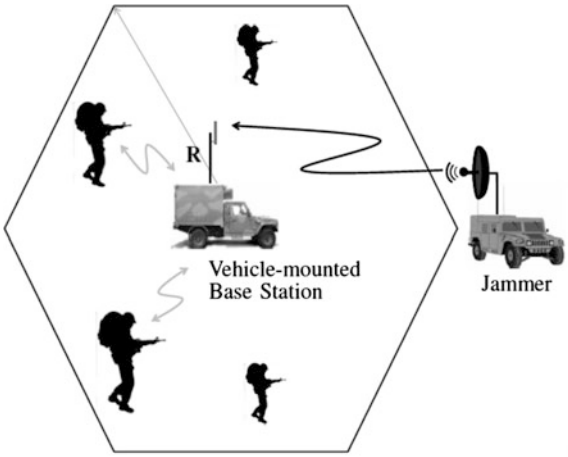

Fig. 1 Simulation scenario

nonoperational period that can considerably degrade the communication. The following steps are performed after the jamming is detected:

1. Terminal disconnection command with next frequency selection is sent by the PDSCH (Physical Downlink Shared Channel); Terminal disconnection command and next frequency selection information is sent by the PDSCH;
2. eNodeB cell is deactivated;
3. eNodeB cell is reconfigured to the new frequency band;
4. eNodeB cell is activated;
5. Terminals start the cell search followed by attaching process.

The delay between steps 2 and 4 can be set in seconds, and may lead application session crash.

3.2.2 Strategy 2: RF Frequency Hopping

The second solution combines cognitive radio with the LTE-A Carrier Aggregation feature in which a single cell can operate with combined channels or RF carriers for modulation, performing Frequency Hopping among the combined channels, which can be applied in the downlink, uplink or both, to avoid jamming attacks. In Frequency Hopping solution, eNodeB and terminals jump to a sequence of pseudorandom frequencies within a DC subcarrier frequency, similar to a traditional Frequency Hopping strategy. Unlike Strategy 1, the cell is not deactivated and the frequency reconfiguration occurs on the RF Circuits levels found in the eNodeB and Terminal. This mechanism is simply performed by RF switches or reconfiguration commands which do not result in any system performance degradation. The LTE baseband, on the other hand, is not modified, since, at each 1 ms (or 1 *Transmission Time Interval*—TTI), the transmission or reception only occurs

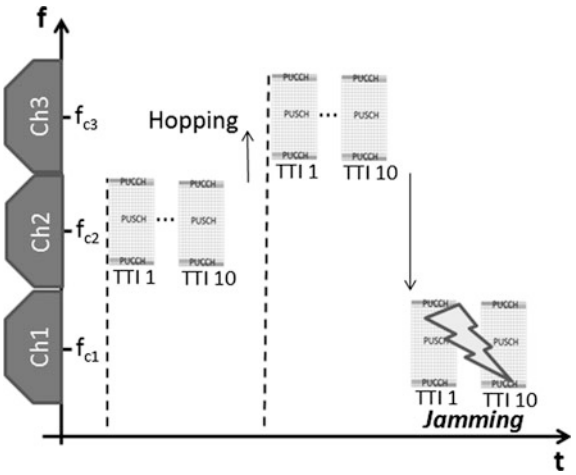

Fig. 2 Uplink communication using frequency hopping

within a single DC subcarrier frequency or channel. Opposite to regular cognitive radio spectrum sensing that evaluates the RF signal, in the current strategy jamming sensing is performed in the eNodeB protocol level that evaluates the channel measuring indicators.

Figure 2 presents the Frequency Hopping operation, in the time and frequency domain, for a single physical carrier for TX or RX, and the corresponding set of three individual channels, each one with its own DC subcarrier frequency of operation. More specifically, Fig. 2 illustrates an example of frequency hopping operation over time, showing only three hops to subcarriers f_{c1}, f_{c2}, and f_{c3} which are, respectively, central subcarriers of channels C_1, C_2, and C_3.

The illustrated frequency hopping starts switching to subcarrier f_{c2} and, after a hopping period, which was selected to be equal to an LTE frame, switches to subcarrier f_{c3}. After another hopping period, the frequency hops to subcarrier f_{c1}. On subcarrier f_{c1} the channel is attacked by jamming signals. The LTE uplink PUCCH remains under attack for a period of time corresponding to an LTE frame, i.e., 10 ms, and then hops to another subcarrier provided by its pseudorandom frequency hopping sequence. The LTE physical broadcast control channel is transmitted in every LTE frame, enabling the adoption of this time as the hopping period of Strategy 2. Additionally, many channel quality measurements are performed during the frame period.

Transmission Time Interval (TTI) is the minimum transmission or reception period. An LTE frame is composed of 10 TTIs. The number of channels is determined by the level demand of hardening and frequency band flexibility.

Thus, Frequency Hopping occurs between LTE frames (10 ms). If jamming occurs at constant frequencies, with a period smaller than 10 ms, communication will not be disrupted due to the HARQ (Hybrid Automatic Repeat Request) message retransmission process, which is another LTE feature that helps to mitigate jamming attacks. The pseudorandom sequence has to be synchronized for both the

eNodeB and the Terminal. The sequence can be programmed in advance or transmitted via PDSCH when tactical mission operations begin. On a classical narrow-band Frequency Hopping, the jammer can still disrupt all channels or carriers. Using the LTE broadband Frequency Hopping strategy, channels or carriers are simultaneously dispersed, requiring a large amount of energy to generate jamming signals. This is particularly relevant when comparing jammings in narrow-band radio communications, which require much less energy over the frequency band, with broadband LTE. The efficiency of the jamming mitigation strategy is demonstrated by the following aspects:

- There is no service disruption;
- The Frequency Hopping does not require the terminal to perform any another RACH procedure;
- The 3GPP standard does not need to be changed;
- The eNodeB and Terminal hardware also do not need to be changed.

Taking into consideration implementation aspects, a single change must be done at the eNodeB and terminal levels: including a command interface to change the frequency of DC subcarrier of the modulator/demodulator. It is recommendable to have an RF front-end circuit that operates in a large range of frequencies, allowing as many hopping channels as possible. This is feasible because terminals usually support large amounts of bandwidth. Next sections present the experiments conducted and the performance results of the proposed solutions.

4 Description of Experiments

The experiments proposed in this section were performed with the aid of the strategies described in Sect. 3.2. Customizations made and design options are also discussed here.

4.1 LTE and Jamming Simulation

The LTE network with jamming signals is simulated with the open source software NS-3. The simulator is a well-known test environment used in many academic works related to cable and wireless networks. The LENA NS-3 module [20] is used to run the LTE network, including all the elements such as: eNodeB, EPC, UE, 3GPP channel models, mobility, and others. The simulation scenario is presented in Fig. 1 and the common configuration is summarized in Table 1. The platoon is served by a vehicle-mounted BS that irradiates LTE signals to all directions. The jammer has a directional antenna with a pencil beam that can fully block the

Table 1 Common simulation scenario parameters

#	Parameter	Value
1	3-GPP Band	28
2	Frequency	703–748 (uplink) 758–803 (downlink)
3	Bandwidth	5 MHz
4	Number of 5 MHz channels in band 28	9
5	Number of cells	1
6	Maximum platoon distance from BS (cell radius)	R = 3 km
7	Platoon size (Number of terminals)	15
8	BS Antenna Type	Omni

Table 2 Specific parameters

Parameter	Strategy 1	Strategy 2
Jamming period	τ_1 = 150 ms	τ_1 = 10 ms at the same LTE hopping period
Jamming searching period for c channels	τ_2 = U (3, 7c/2) s	None. Hopping pseudorandomly
LTE network changing frequency delay period	τ_3 = U (10–20) s	None. Instantly

eNodeB reception, at the uplink channel, after τ_1 milliseconds. Specific parameters of Strategies 1 and 2 are summarized in Table 2.

For Strategy 1, τ_1 period is based on the maximum number of HARQ retransmissions, since the LTE protocol is designed to keep the connection up for this period even in the presence of strong interference. Only after this time, the eNodeB drops the terminal and the reconnection process starts.

For Strategy 2, which uses a pseudorandom hopping sequence, τ_1 period has the same LTE frequency hopping period duration, although the jammer could stand in a single channel for a longer period, to make sure the eNodeB uplink transmission is over. The jammer keeps tracking of the LTE channels to search for new eNodeB frequency operations.

The scanning period is proportional to the number of available channels for Strategy 1, which can be described by the uniform random variable τ_2. In Strategy 2, it is assumed that the jammer cannot track the LTE signal within a period below 10 ms, since reactive jamming includes a temporal penalty to perform an analysis of the detected uplink transmission and to identify PUCCH channels before any attack occurs. In addition, the temporal penalty growth is proportional to the spectrum bandwidth, since the jammer has to search for the desired uplink transmission rate in order to detect and identify it. The LTE network uses a random variable τ_3 to switch its frequency to a new channel. The frequency is much higher in Strategy 1, because the LTE cell is deactivated and the terminal's reconnection process is started over. In Strategy 2, the LTE cell is not deactivated/activated, so

the DC carrier hopping starts immediately after, because it is based on a RF switch command.

Terminals are transmitting video streaming to the base station, which accelerates the exhaustion of cell capacity. The video freezes with the jamming, but the logical session of the transport layer is not interrupted, and no significant delay is added. The uplink cell throughput is measured at the end of the simulation to compare results between both. Each simulation campaign is composed of 10 rounds of 5 min.

The 3GPP FDD Band 28 (APT 700 MHz) is chosen because some regulators tend to select this band for Public Safety. In Brazil, the first channel (703–708 and 758–763 MHz) is assigned to the Defense and the Public Safety and Infrastructure sectors. Band 28 is composed of 9 × 5 MHz channels, for military purposes, in remote areas such as Country borders, which can all be used to provide communication.

4.2 Simulation Results Analysis and Discussion

In order to evaluate the performance of both mitigation strategies, simulations were performed with a complete LTE System including many Terminals, eNodeB, and EPC (Core Network). The NS-3 software, with LENA package, was chosen for the simulation, which includes channel models, mobility, feedback messages, link adaptation, power control, and many other features. The simulator is able to measure important information, like throughput and delay, in an almost exact replication of the real operation. Details of simulation parameters are shown in Table 1.

The results presented in this section are derived from the following measurement methodology: The uplink cell throughput are evaluated without any source of jamming and proportionally compared with scenarios 1 and 2. All data are taken from the PDCP LTE layer. The performance is evaluated with Cell Frequency Reconfiguration and Frequency Hopping for channels and bands ranging from 1 to 2, 1 to 3, 1 to 4, up to 1 to 9. Therefore, the last configuration is much less likely to be jammed. Initially, Figs. 3 and 4 present the received bytes over the sampling time for available channels 2 and 9, respectively.

Each sample stores bytes received from all Terminals in the uplink PDCP in 1.5 s. Strategy 1 refers to the "Cell Frequency Reconfiguration" and the Strategy 2 to "RF Frequency Hopping" as described in Sects. 3.2.1 and 3.2.2. Strategy 1 functions as an on/off switch. In off periods, all bytes are lost as a result of the jamming. There is a smooth transition between the states because of the Terminal attach procedure. As expected, there are many more transitions as the number of available channels decreases. Strategy 2 works pseudorandomly because the jamming attack occurs between LTE frames (10 ms), hopping from one channel to another. Therefore, each sample time refers to the bytes received over 150 LTE frames, which never blocks the eNodeB reception for a longer period as that of the

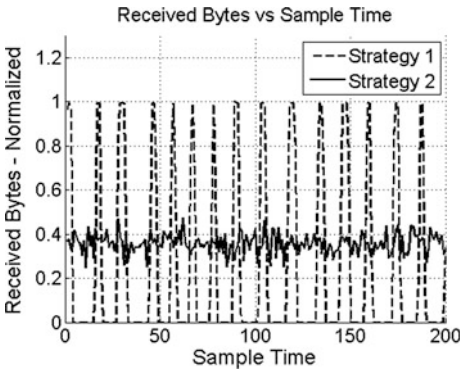

Fig. 3 Received bytes at the PDCP layer over the simulation period with two available channels

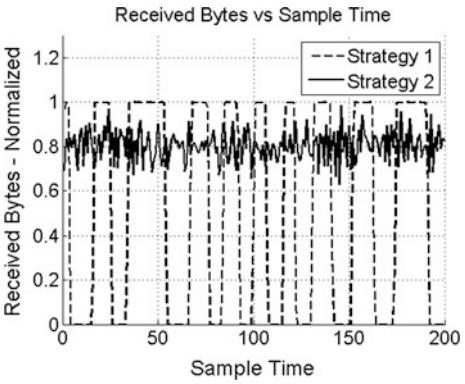

Fig. 4 Received bytes at the PDCP layer over the simulation period with nine available channels

Strategy 1. Figure 5 shows the uplink cell throughput with available channels/bands ranging from 2 to 9 and then normalized with respect to throughput in a jamming-free scenario. The ordinal axis is evaluated by taking the cell throughput from the given jamming scenario and then that of the normalized jamming-free scenario. The cell throughput is evaluated as the sum of all individual Terminals throughput. The jamming-free is the scenario without any jamming attacks.

The confidence interval is evaluated with 10 different simulation rounds, changing the statistic seed, which leads to many modifications in the Terminal cell position and in mobility directions. Strategy 1 results are greatly inferior to those of the Strategy 2, especially because of the frequency changing delay (τ_3), which penalizes the transmission for many seconds. This penalty is reduced as the number of available channels increases.

Strategy 2 presents a much better performance, demonstrating about 50% better results when compared to those of the first strategy. There is a slightly higher decrease in the performance as the number of available channels becomes lower. The expected value for the scenario with 2 channels, for instance, would be 50%, as 1 in every two frames is attacked.

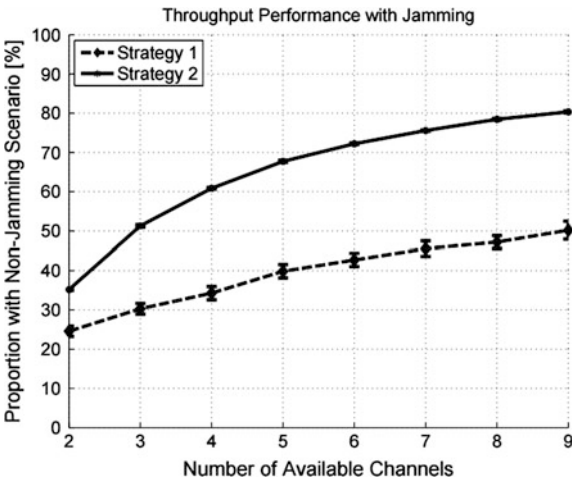

Fig. 5 Proportional uplink cell throughput compared with jamming-free scenario

However, jammed frames force all the protocol stacks to waste air interface resources with retransmissions, contributing to the reduction of the PDCP effective throughput. As the number of available channels increases, the effects from packages retransmissions decrease. On the other hand, the nine-channel scenario, for instance, loses one in every nine frames. Therefore, the expected throughput would be of 88% in comparison with the jamming-free scenario. The simulation results reached 80%, which is much closer to the expected value. The difference of 8% is due to the retransmission effect.

5 Conclusion

This paper presents an innovative strategy based on a cognitive radio approach to avoid severe LTE system performance degradation caused by jamming attacks. The presented jamming mitigation techniques can be applied at the downlink or uplink directions and FDD or TDD.

The cognitive radio sensing is performed in the eNodeB protocol level, by evaluating the channel measuring indicators. There is also no need to implement changes to the 3GPP standard, to the base station or to the terminal hardware.

Taking implementation aspects into consideration, the firmware at the RF frequency selector may require some updates in order to implement the cognitive radio strategy at the base station and at the terminal. This simple intervention has many advantages, such as making unnecessary the acquisition of new equipment, using remote software control and updating hop-ping strategy, besides maintenance simplification.

Different from narrow-band jamming evaluation scenarios, the solution proposed took into consideration LTE protocol issues like frame structure, synchronization

signals, and control channel structures. Important parameters, such as the hopping period, were selected in order to avoid bad LTE channel quality reports. Therefore, the frequency hopping was configured taking into account LTE system level aspects. Frequency Hopping can be performed in all 3GPP frequency bands, depending only on the RF circuit flexibility and in areas where spectrum or channel availability are not a major constraint, such as greenfield deployment scenario, or where the military spectrum usage has preference over the civil spectrum.

There are no constraints related to the eNodeB or Terminal architecture. The eNodeB can be static or mobile like COW (Cell on Wheels) or SOW (System on Wheels) architectures. The Terminal can be static or mobile, such as a Man Backpack or a portable Smartphone.

The technique is also effective in distributed jamming attacks, keeping the LTE system operation in the battlefield. Throughput degradation is more intense in Strategy 1 as the jamming signals force the cell setup to switch to another available frequency channel, which leads to an on/off operation over the time. Strategy 2 presents a much better performance when compared to that of the first strategy because it is based on hopping strategies, but it also considers the LTE protocol particularities.

As the number of available channels increases, retransmission effects that are influenced by the LTE frame attacks are reduced. The strategies proposed are complementary with the interference mitigation advantages that are already available in the LTE protocol: OFDM physical layer, resource block scrambling, and interference aware schedulers. When combined, cognitive radio strategies make the LTE deployment more feasible for military battlefield applications.

Acknowledgements The CPqD LTE 450 Project was supported by FUNTTEL (Telecommunications Technology Development Fund), from the Ministry of Communications.

References

1. Kwan R, Leung C (2010) A survey of scheduling and interference mitigation in LTE. J Electr Comput Eng 2010(273486):10
2. Sesia S, Toufik I, Baker M (2011) LTE, the UMTS long term evolution: from theory to practice, 2nd edn. Wiley Ltd, Chichester, West Sussex, United Kingdom
3. Clancy TC, Norton M, Lichtman M (2013) Security challenges with LTE- advanced systems and military spectrum. In: Military communications conference, MILCOM 2013-2013. IEEE, pp 375–381
4. Menon R, Yun J, Gormley E, Immendorf C (2013) SON for government spectrum applications. In: Military communications conference, MIL-COM 2013-2013. IEEE, pp 1308–1315
5. Kakar J, McDermott K, Garg V, Lichtman M, Marojevic V, Reed JH (2014) Analysis and mitigation of interference to the LTE physical control format indicator channel. In: Military communications conference (MILCOM), 2014. IEEE, pp 228–234
6. Lichtman M, Czauski T, Ha S, David P, Reed JH (2014) Detection and mitigation of uplink control channel jamming in LTE. In: Military communications conference (MILCOM), 2014. IEEE, pp 1187–1194, 6–8 Oct 2014

7. Andrusenko J, Burbank JL, Ouyang F (2015) Future trends in commercial wireless communications and why they matter to the military. Johns Hopkins APL Tech Dig 33(1)
8. White Paper, Mobile broadband explosion: the 3GPP wireless evolution. 4G Americas. http://www.4gamericas.org/en/resources/white-papers/2013/, Aug 2012
9. G Americas White Paper, LTE carrier aggregation technology development and deployment worldwide. http://www.4gamericas.org/en/resources/white-papers/2013/, Oct 2014
10. G Americas White Paper, Spectrum Sharing. http://www.4gamericas.org/en/resources/white-papers/2013/, Oct 2014
11. White Paper, On the future architecture of mission critical mobile broadband PPDR networks. Federal Ministry of the Interior, Project Group on Public Safety Digital Radio; Federal Coordinating Office, 10559 Berlin, Germany
12. Forge S, Horvitz R, Blackman C (2014) Is commercial cellular suitable for mission critical broadband? A study prepared for the European commission DG communications networks, content and technology by: SCF Associates LTD. European Union
13. Grover K, Lim A, Yang Q (2014) Jamming and anti-jamming techniques in wireless networks: a survey. Int J Ad Hoc Ubiquit Comput Arch 17(4):197–215
14. Rohde and Schwarz, White Paper, Vulnerabilities of LTE and LTE-advanced communication. 1MA245
15. Wilhelm M, Martinovic I, Schmitt JB, Lenders V (2011) Short paper: reactive jamming in wireless networks: how realistic is the threat?. In: Proceedings of the fourth ACM conference on wireless network security (WiSec'11). ACM, New York, NY, USA
16. Coupland R, Jenkins R, Presentation: a discussion on deployable systems to address FirstNet needs. Broadband summit, 05 May 2014
17. Schmitt M, Deaton J, Papke C, Cherry S (2008) Analyzing options for airborne emergency wireless communications. Idaho National Laboratory (INL)
18. Piqueras Jover R (2013) Security attacks against the availability of LTE mobility networks: overview and research directions. In: 2013 16th international symposium on wireless personal multimedia communications (WPMC), pp 1–9, 24–27 June 2013
19. Hutchison K (2005) Wireless intrusion detection systems. GIAC Security Essentials Certification (GSEC) Practical Assignment Version 1.4c, SANS Institute
20. Baldo N, The ns-3 LTE module by the LENA project. https://www.nsnam.org/tutorials/consortium13/lte-tutorial.pdf

5G Cognitive Wireless Mesh Network Without Common Control Channel

D. Carrillo, R. Takaki, F. Lira Figueiredo and F. Mathilde

Abstract Collaborative cognitive mesh networks (CCMN) are a potential technology to be adopted in next-generation wireless networks, as it meets key requirements of 5G application scenarios, such as high flexibility and efficient spectrum usage. CCMN is composed of regular cognitive mechanisms and components, such as energy detection-based sensing, and has the ability to switch the data channel to take advantage of any available channels on a given spectrum band. Several cognitive mesh network architectures employ a common control channel (CCC) to perform dynamic channel allocation. Therefore, the multichannel–single interface manager (MC-SIM) algorithm aims to maximize channel usage with a system that does not depend on any CCC. The MC-SIM algorithm was tested in a real scenario and results showed enhanced throughput levels that are 29.5% greater.

1 Introduction

Over the last few decades, wireless telecommunications technologies have evolved quite fast. While 2G (Mobile Second Generation) provided the possibility to increase the number of simultaneous phone calls sharing the same RF (Radio Frequency) spectrum, 3G technology (Mobile Third Generation) increased the data rate transmission and improved the quality of services. In the past decade, some standards, such as the 3GPP Release 8 (Third Generation Partnership Project

D. Carrillo (✉) · R. Takaki · F. Lira Figueiredo · F. Mathilde
CPqD Foundation, Campinas, SP, Brazil
e-mail: dickm@cpqd.com.br

R. Takaki
e-mail: rtakaki@cpqd.com.br

F. Lira Figueiredo
e-mail: fabricio@cpqd.com.br

F. Mathilde
e-mail: fabianom@cpqd.com.br

A. Paradisi et al. (eds.), *Cognitive Technologies*, Telecommunications and Information Technology, DOI 10.1007/978-3-319-53753-5_6

Release 8—LTE) and 802.16e/m (Worldwide Interoperability for Microwave Access—WiMAX), improved the spectral efficiency of wireless channels using OFDM (Orthogonal Frequency-Division Multiplexing), but failed to achieve the IMT-A (International Mobile Telecommunications Advanced) requirements. One of these requirements consists of supporting a peak data rate up to 1 Gbps in the Downlink (DL), for the best case scenarios in terms of channel bandwidth and radio propagation.

In order to meet IMT-A requirements, 3GPP has released LTE LTE-Advanced (LTE-A) [1], and more recently Release 12, LTE-B version.

The evolution to 5G networks has been driven by an increased demand for traffic which is expected to take place over the next decade, due to more complex applications and contents, such as 3D multimedia, HDTV (High Definition TV), VoIP (Voice over IP), gaming, e-Health, and Vehicle to Vehicle Communications. As an example, 5G is expected to provide a thousand times more network capacity compared to 4G, as well as allow 10–100 times more connected devices. 5G also aims to increase power consumption by 10 times, with five times reduced latency, compared to 4G. In this context, 5G data rates should reach up to10 Gbps [2].

On the other hand, 50 billion devices are expected to be connected until 2020 [3]. Mass development of applications will lead to further diverse requirements in wireless communication systems. LTE-B, for example, is targeted to complement cellular service with Wi-Fi (Wireless Fidelity—IEEE 802.11) to further increase the overall traffic capacity. Integration of LTE and Wi-Fi is currently supported by the core network. However, considering that public Wi-Fi hot spots deployed by mobile operators are becoming more popular, integrated air interfaces will be required. Thus, a 5G requirement is to ensure service coverage by using hot spots in urban areas with high subscriber density. In order to meet such requirement, dynamic wireless mesh networks (DWMN) [4] architectures can be considered, as a complimentary approach to regular cellular networks. DWMN are wireless mesh networks whose architecture is based on the implementation of cognitive radio concepts.

This chapter presents the results of a DWMN implementation in a real-world scenario, named (CCMN, which was developed, installed and tested at CPqD facilities. The MC-SIM algorithm was implemented, enabling the control channel management without depending on a CCC. This feature provides significant increase in overall system throughput gains.

Authors [5–7] contributed with insights on performance optimization of cognitive mesh networks, considering that there is no common control channel. All of these approaches provide similar throughput results when compared to those presented in this chapter, although all of them are restricted to simulation results.

The structure of this chapter is described as follows: Sect. 2 provides a description of the cognitive mesh network architecture. Section 3 describes the architecture of CCMN. Details on the experimental network are presented in Sect. 4. In Sect. 5 conclusions are presented.

2 Cognitive Wireless Mesh Networks

This section outlines the architecture of cognitive wireless mesh networks as well as channel routing and switching mechanisms.

2.1 Cognitive Wireless Mesh Network Architecture

The elements of a cognitive wireless mesh network are mainly cognitive mesh routers that coexist with primary users (PUs), which can be, for example, IEEE 802.11 access points and Bluetooth or Zigbee devices. Experimental results in urban areas with high user density show that these devices occupy most of the ISM (Industrial, Scientific, and Medical) spectrum band [8].

Cognitive mesh routers are wireless devices equipped with multiple radio interfaces. One of these interfaces is used to exchange control messages between routers [9] and the remaining interfaces are used to send and receive packets through multiple channels. A particular case of this architecture was developed in [10], corresponding to a Wi-Fi cognitive mesh network, with data packet transmission on four different channels, dynamically selected by the cognitive mechanism. The control message interface is a dedicated CCC, comprising routing and updated channel status information.

2.2 Channel Routing and Switching in Cognitive Wireless Mesh Networks

Routing protocols enable routers to discover multiple paths from a source node toward a gateway or any other specific destination. Alternative routes can be used when the source path is not available, the path is jammed as a result of other routing activity or PU signals are detected.

There are on-demand routing protocols [11, 12] that use the ETX (Expected Transmission Count) metric [13], others using the ETT (Expected Transmission Time) or the WCETT (Weighted Cumulative ETT) [14] metrics, which are not appropriate when the path between two routers is fixed and the link quality is modified by PU activity. Kassler et al. [15] describes an algorithm called Urban-X that implements a forwarding mesh structure. In this algorithm, the message is transmitted between routers and contains information of relay router.

2.3 Assignment Techniques in Scenarios with Multiple Channels and Multiple Interfaces

In [16] various scenarios are presented with multiple communication channels, however, the number of available interfaces is considerably smaller. Other studies show strategies employed to assign interfaces, which can be classified as follows:

- Static assignment: each interface is assigned a specific channel for a long period of time [17, 18].
- Dynamic assignment: in this approach, any interface can be assigned to any channel, and can be switched from one channel to another. In this case, it is crucial to use a proper coordination mechanism to ensure that the interfaces are on the same channel [19, 20].
- Hybrid assignment: a combination of the previous two approaches, in which static assignment and dynamic assignments are applied for different interfaces. Wu et al. [21] provides an example of a hybrid approach.

3 CCMN—Collaborative Cognitive Mesh Networks

3.1 Architecture of CCMN

The adopted CCMN architecture comprises two kinds of cognitive router, each one equipped with multiple radio interfaces. These routers were named management cognitive mesh router (MCMR) and forwarding cognitive mesh router (FCMR). They are described next:

- MCMR is composed of three radio interfaces (R1, R2 and R3). R1 is a Wi-Fi interface that operates in frequency bands below 1 GHz. R2 is a RF interface, responsible for spectrum sensing. R3 is another Wi-Fi interface that operates at 2.4 GHz frequency bands.
- FCMR is composed of two RF interfaces (R1 and R3), providing the same functionalities offered by MCMR interfaces.

The R1 interface is responsible for data transmission between FCMR and MCMR router and operates on a channel that is dynamically adjusted according to PU activity.

The R2 interface is composed of an antenna that operates in the frequency band sub-1 GHz. The signal received by R2 is processed by an energy detection algorithm in order to check the spectrum signal only outside the band, in contrast with the regular procedure found in the literature (in-band and out-band sensing simultaneously) [10].

The R3 interface is responsible for establishing connectivity between networks operating at sub-1 GHz frequency bands and commercial devices operating at 2.4 GHz frequency bands (smartphones, tablets, etc.).

In [15] a cognitive multi-radio architecture is presented, which is based on principles of dynamic spectrum access to improve mesh network throughput. It also contemplates an algorithm for optimizing traffic channel allocation when any PU activity is detected.

In the absence of a CCC, the control information will be transmitted via data channels. Mesh network routers always switch to the same channel, even having detected a PU with high channel occupancy that might interfere in the connection between routers. This technique is known as Frequency *Rendezvous* [22]. In order to minimize the performance impacts in this scenario, the algorithm called (MC-SIM) is proposed.

3.2 Spectrum Sensing

CCMN spectrum sensing is based on the implementation of an energy detector sensor. The energy detector sensitivity ensures PU protection against interferences [23].

The energy detector algorithm calculates the statistics of samples collected by the R2 interface. This signal is represented by r(n), so the average power is estimated using the relationship of Eq. (1), in which M is the number of samples.

$$Z_{DE}(n) = \frac{1}{M} \sum_{n=0}^{M-1} |r(n)|^2 \tag{1}$$

The average power represented by Z_{DE} is compared with the threshold λ, which is dynamically calculated based on a given value of false alarm probability. The optimal λ calculation details are outside the scope of this chapter.

The threshold λ is used to decide if the channel is occupied or available according to Eq. (2).

$$\begin{aligned} &if \quad Z_{DE} > \lambda \rightarrow H_0 \\ &if \quad Z_{DE} \leq \lambda \rightarrow H_1 \end{aligned} \tag{2}$$

in which H_0 and H_1 represent a hypothesis that the channel is occupied by the PU and the channel is not occupied, respectively.

Based on information of Eqs. (1) and (2), the MCMR will calculate the average power for all available channels. Occupancy statistics are represented by the variable Z_j.

Equation (3) is used to select the channel with less occupancy in group A. Group A represents all available channels.

$$i = arg \max_{j} \frac{1}{Z_j},\ j \in \mathrm{A} \tag{3}$$

Equation (3) is used by the MCMR to select the best channel, and each router must keep an updated ranking of the best channels according to this rule. In the proposed architecture, a cognitive controller periodically collects the spectrum occupancy information from the mesh routers, organizes the ranking of channels and uses a control or data channel to send the information back to the network.

3.3 Multi Channel–Single Interface Manager (MC-SIM)

The MC-SIM algorithm enables the CCMN architecture to be developed without using a common control channel. This approach allows monitoring and managing of a router characterized of having multiple channels to operate through a single interface.

MC-SIM is based on Algorithm 1, it is organized in three main steps, which are presented next.

Step 1 is a process of defining routers' connection status. The algorithm consists of broadcasting beacons among all routers. Once a router receives a beacon, the variable **IsAlive** switches to 1, otherwise it switches to 0. Thus, the algorithm contemplates two possible states for variable **IsAlive**:

- **IsAlive = 1** when the communication between routers is working properly.
- **IsAlive = 0** when the communication between routers has any failures.

Step 2 is performed in order to validate the channel, based on two well-defined parameters:

$$\begin{aligned} P_i &\rightarrow DataTransmission\ Flow \\ Z_i &\rightarrow Occupancy\ of\ Channel\ i \end{aligned} \tag{4}$$

Parameter P_i is calculated in order to benefit from the MAC layer algorithm that controls data rate in IEEE 802.11 standard. This algorithm is named Minstrel [24], which classifies transmission rates according to an integer discrete scale [0, 1, 2, 3, 4, 5, 6, 7, 8, 9]. For example, if data transmission flow is too low, Minstrel will use a rate equal to zero. In the same way, if the data transmission flow is too high, the Minstrel will use a rate equal to nine.

Parameter Z_i, which was defined in Eq. (1), represents the channel occupancy, which depends on spectrum sensing accuracy in order to determine if a channel is occupied or available. Details on how to calculate such statistics are outside the scope of this work. Next, the product of parameters P_i and $\frac{1}{Z_i}$ is calculated. This operation is repeated for all available channels and results are saved in vector Q.

In step 3 vector elements of Q are arranged in descending order. The first element of this vector will indicate the best channel for transmission.

Algorithm 1: The MC-SIM algorithm's step by step

STEP 1: Message transmission between MCMR and FCMR routers to check communication

1. Check $IsAlive_{jk}, j \neq k, \{j, k \in G\}$

STEP 2: Getting the metrics to be used as a decision trigger

1. **for** $i \in F, F \rightarrow Set\ of\ Channels$ **do**
2. $Q \leftarrow \frac{P_i}{Z_i}$
3. **end for**

STEP 3: Ranking of channels update

1. **while** $Q \neq 0$ **do**
2. $C \leftarrow descendingOrder(Q)$
3. $i^* \leftarrow C[0]$
4. **if** $ActualChannel = 0$ **then**
5. $switch\ to\ channel\ i^*$
6. **if** $ActualChannel = 0$ **then**
7. $i^{**} \leftarrow C[1]$
8. $switch\ to\ channel\ i^{**}$
9. **end if**
10. **end if**
11. **end while**

3.4 Routing and Switching Channel

While the implementation of CCMN focuses on network performance evaluation in cognitive scenarios, the distribution of routers is made so that the routing protocol is fixed between routers to ensure that the routing table is always the same.

The channel switching scheduling is based on information of channel ranking provided by Eq. (3). The resource manager provides details on the cognitive network deployed at CPqD campus that are outside the scope of this study. Please refer to [10].

The difference of the MC-SIM algorithm in relation to practical implementations of cognitive networks [10] is that it does not run any in-band sensing process. When PU and WMN access the channel at the same time, mesh routers shall switch to the best channel (i^*). Therefore, synchronization is a critical factor in this algorithm. In fact, if routers cannot synchronize, each WMN will switch to channel i^{**}, called emergency channel.

A key element in a practical implementation of the MC-SIM algorithm is that all routers need to be synchronized, therefore all cognitive routers run a NtpClient-based script to ensure network synchronization. WMN channels are changed in case a new best channel is detected. The idea is that, in contrast to [10], routers do not turn off Wi-Fi interfaces at any moment.

4 Experimental Results with CCMN

This section presents experimental results from field tests performed with CCMN at CPqD facilities.

4.1 CCMN Configurations

As stated in Sect. 2, CCMN is composed of two types of cognitive routers: MCMR and FCMR.

The experimental network deployed at CPqD consists of one MCMR and two FCMR routers.

MCMR is composed of an embedded system responsible for running the MC-SIM algorithm using information from the following sources:

- The power detector, which provides the information that will be used to calculate the channel occupancy. This energy detector runs on a software-defined radio (SDR) platform;
- The mesh router provides data rate information related to the Minstrel algorithm. A cross-layer algorithm is performed on a Wi-Fi standard architecture (MAC/PHY) to define channel switching sequences and the algorithm that will determine the status of the variable ***IsAlive***.

The communication between routers (MCMR and FCMRs) is based on a Wi-Fi Mesh interface, which is able to switch between frequency channels: 763, 768, 773, and 778 MHz. Network topology is shown in Fig. 1. All routers provide Wi-Fi internet access occupying a 2.4 GHz band.

4.2 Primary User Model

In order to evaluate cognitive network performance, primary user spectrum occupancy is emulated by an OFDM signal generation, according to the following operation modes:

- PU sequential mode: primary users have an incremental change in channel operation, for example: $CH1 \rightarrow CH2 \rightarrow CH3 \rightarrow CH4$
- PU random mode: primary users follow a random pattern to switch channels for example: $CH3 \rightarrow CH1 \rightarrow CH2 \rightarrow CH4$

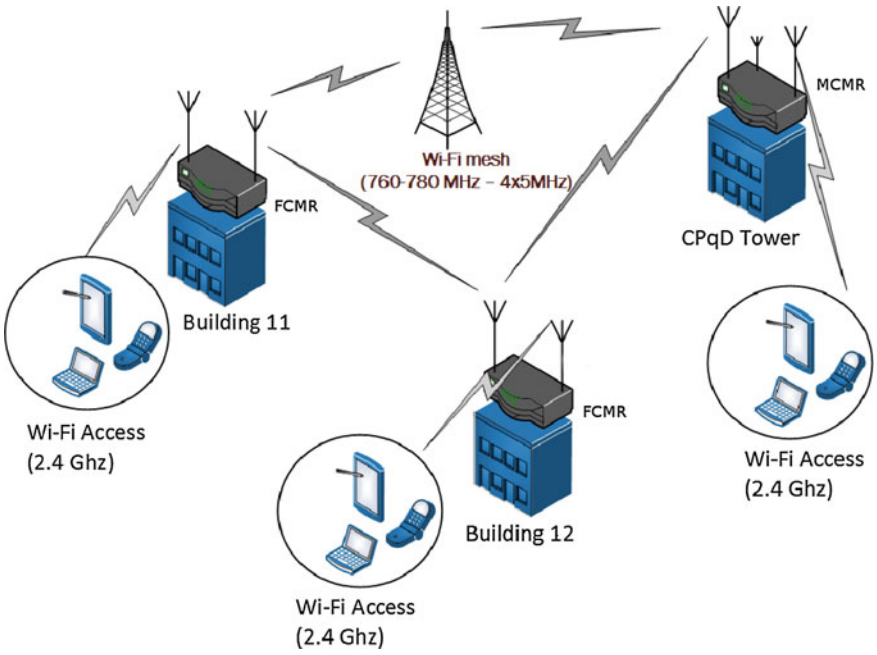

Fig. 1 Experimental network topology of CCMN deployed at CPqD facilities

PU signals are generated in frequencies below 1 GHz, with the following features:

- Signal generation is performed only in one of the four available channels
- Signal is generated with a low SNR, typically greater than 3 dB
- OFDM with BPSK modulation, with typical data rate of 2.5 Mbps, 5 MHz BW, FFT 512, and CP 128

4.3 Experimental Results

Tests were based on the network performance test tools (iperf and Wget). TCP traffic was generated in different scenarios to provide distinguished system performance in cases MC-SIM algorithm is adopted.

Results are shown in Table 1. All measurements show the average throughput increased when the MC-SIM algorithm was active. Furthermore, Sequential PU mode presented the highest throughput gain, compared with the reference scenario (absence of cognition and PU activity).

Table 1 Average throughput with TCP traffic using the MC-SIM algorithm

Average throughput (Mbps)		Primary user type	Throughput gain (%)
With MC-SIM	Without MC-SIM		
6	6	Without PU and without cognition	
5.23	4.83	Without PU	8.28%
4.83	3.73	Sequential PU	29.5%
4.94	4.43	Random PU	11.5%

5 Conclusion

This chapter presented the architecture and test results of a DWMN, with high potential to be incorporated in future networks, including 5G scenarios. Named CCMN, the DWMN was developed and implemented in a real scenario at CPqD facilities.

The MC-SIM algorithm was tested in all routers, enabling in-band management control channel, without using CCC. Thus, multiple channels were dynamically selected over a single interface, thereby maximizing the number of available channels. The algorithm MC-SIM also generated important total throughput gains, with increased channel capacity. All tests performed using the MC-SIM algorithm provided a higher throughput, when compared to tests performed without the algorithm. As an example, for PU sequential generation, the average TCP traffic throughput using the MC-SIM algorithm was 4.83 Mbps, in contrast with 3.73 Mbps achieved in the very same scenario but without the MC-SIM algorithm, producing an average gain of 29.5% in overall system performance.

References

1. Noh J-H, Oh S-J (2011) System-level simulation of LTE/LTE-A for IMT-advanced systems. In: Vehicular technology conference (VTC Spring), 2011 IEEE 73rd, Yokohama, pp 1–5
2. Hossain E, Rasti M, Tabassum H, Abdelnasser A (2014) Evolution toward 5G multi-tier cellular wireless networks: an interference management perspective. In: IEEE_M_WC, vol 21, no 3, pp 118–127, June 2014
3. Ericsson (2014) Connected devices. [Online]. More than 50 Billion connected devices (white paper)
4. Gohil A, Modi H, Patel SK (2013) 5G technology of mobile communication: a survey. In: 2013 international conference on intelligent systems and signal processing (ISSP), Gujarat, pp 288–292
5. Dai Y, Wu J, Xin C (2013) Efficient virtual backbone construction without a common control channel in cognitive radio networks. In: INFOCOM, 2013 proceedings IEEE, Turin, April 2013, pp 1456–1464
6. Zhang J, Zhang Z (2011) Initial link establishment in cognitive radio networks without common control channel. In: Wireless communications and networking conference (WCNC), 2011 IEEE, Cancun, Quintana Roo, pp 150–155

7. Kondareddy YR, Agrawal P, Sivalingam K (2008) Cognitive radio network setup without a common control channel. In: Military communications conference, 2008. MILCOM 2008. IEEE, San Diego, CA, pp 1–6
8. Gokhale D, Sen S, Chebrolu K, Raman B (2008) On the feasibility of the link abstraction in (rural) mesh networks. In: INFOCOM 2008. The 27th conference on computer communications. IEEE, Phoenix, AZ, pp 13–18
9. Kyasanur P, Chereddi C, Vaidya NH (2006) Net-x: system extensions for supporting multiple channels, multiple interfaces, and other interface capabilities, Technical 2006
10. Carrillo D, Mathilde F, Yoshimura R, Bazzo J (2013) Red experimental cognitiva: Algoritmos y resultados. In: 2013 IEEE Colombian conference on communications and computing (COLCOM), Medellin, pp 1–5
11. Subramanian AP, Buddhikot MM, Miller S (2006) Interference aware routing in multi-radio wireless mesh networks. In: 2nd IEEE workshop on wireless mesh networks, 2006. WiMesh 2006. Reston, VA, pp 55–63
12. Waharte S, Ishibashi B, Boutaba R, Meddour D (2008) Interference-aware routing metric for improved load balancing in wireless mesh networks. In: IEEE international conference on communications, 2008. ICC '08. Beijing, pp 2979–2983
13. Aguayo D, Bicket J, Morris R, De Couto DSJ (2003) A high-throughput path metric for multi-hop wireless routing
14. Draves R, Padhye J, Zill B (2004) Comparison of routing metrics for static multi-hop wireless networks, Technical 2004
15. Kassler AJ, Di Felice M, Gerla M, Kim W (2010) Cognitive multi-radio mesh networks on ISM bands: a cross-layer architecture. In: Performance computing and communications conference (IPCCC), 2010 IEEE 29th international, Alburqueque, NM, pp 34–41
16. Kyasanur P, Vaidya NH (2006) Routing and link-layer protocols for multi-channel multi-interface ad hoc wireless networks. In: ACM SIGMOBILE mobile computing and communications review, New York, pp 31–43
17. Draves R, Padhye J, Zill B (2004) Comparison of routing metrics for static multi-hop wireless networks. In: ACM SIGCOMM computer communication review. New York, pp 133–144
18. Raniwala A, Gopalan K, Chiueh T (2004) Centralized channel assignment and routing algorithms for multi-channel wireless mesh networks. In: ACM SIGMOBILE mobile computing and communications review, vol 8, no 2, pp 50–65, April 2004
19. Dunagan JD, Bahl P, Chandra R (2008) Slotted seeded channel hopping for capacity improvement in wireless networks, US Patent 7,379,447
20. So J, Vaidya NH (2004) Multi-channel mac for ad hoc networks: handling multi-channel hidden terminals using a single transceiver. In: MobiHoc '04 proceedings of the 5th ACM international symposium on Mobile ad hoc networking and computing, New York, pp 222–233
21. Wu S-L, Lin C-Y, Tseng Y-C, Sheu J-P (2000) A new multi-channel MAC protocol with on-demand channel assignment for multi-hop mobile ad hoc networks. In: International symposium on parallel architectures, algorithms and networks, 2000. I-SPAN 2000. Proceedings. Dallas, TX, pp 232–237
22. Bian K, Park J-M (2013) Maximizing rendezvous diversity in rendezvous protocols for decentralized cognitive radio networks. IEEE Trans Mobile Comput 12(7):1294–1307
23. Chandran A, Karthik RA, Kumar A, Naidu RC, Siva MS, Iyer US, Ramanathan R (2010) Evaluation of energy detector based spectrum sensing for OFDM based cognitive radio. In: 2010 international conference on communication and computational intelligence (INCOCCI), Erode, pp 163–167
24. Hart J, Fu Q, Xia D (2013) Evaluation of the Minstrel rate adaptation algorithm in IEEE 802.11g WLANs. In: 2013 IEEE international conference on communications (ICC), Budapest, pp 2223–2228

A Fast and Efficient 3D Beamforming Algorithm for Cognitive Radio Networks

A.J. van den Biggelaar, A.B. Smolders, C.B. de Paula, D.C.S. e Silva and J.J. Bazzo

3D beamforming can be applied to avoid interference between primary and secondary users in cognitive radio networks. One of the questions that arise when designing an antenna system to perform beamforming is how to properly determine the current excitations. Multiple techniques are available in literature, but most of them make assumptions on the E-field patterns of the individual antenna elements, resulting in inaccurate beam steering results. Techniques that do not impose any assumptions are often computationally very intensive, resulting in an increased design time. This chapter presents a fast, flexible, and accurate algorithm to find the current excitations in order to shape the 3D radiation pattern of an arbitrary antenna system.

A.J. van den Biggelaar (✉) · A.B. Smolders
Department of Electrical Engineering, Electromagnetics Group Eindhoven University of Technology (TU/e), Eindhoven, Netherlands
e-mail: a.j.v.d.biggelaar@tue.nl

A.B. Smolders
e-mail: a.b.smolders@tue.nl

C.B. de Paula · D.C.S. e Silva · J.J. Bazzo
CPqD Foundation, Campinas, São Paulo, Brazil
e-mail: cborges@cpqd.com.br

D.C.S. e Silva
e-mail: diogos@cpqd.com.br

J.J. Bazzo
e-mail: jbazzo@cpqd.com.br

A. Paradisi et al. (eds.), *Cognitive Technologies*, Telecommunications and Information Technology, DOI 10.1007/978-3-319-53753-5_7

1 Introduction

A cognitive radio network is composed of many functionalities that are able to get information from the environment and change the radio parameters in order to improve the system performance. The most known functionality is spectrum sensing, in which devices measure the spectrum in order to share the same frequency as efficiently as possible. Primary and secondary users are the usual terms that refer, respectively, to the radio that owns the spectrum license and has priority over the use of a given spectrum, and non-licensed devices that can access vacant spectrum opportunistically when primary users are idle. Therefore, spectrum sensing is an important functionality that prevents interference between both users, bringing new challenges for signal detection and estimation and maximizing spectrum usage efficiency. The spatial dimension has not been exploited well enough for spectrum opportunity. It is assumed that primary users and secondary users transmit in all directions. However, with the recent advances in multi-antenna technologies, e.g., beamforming, multiple users can be multiplexed into the same channel at the same time and in the same geographical area [1]. Previous works like in [2] investigate the impact of using directional antennas and beamforming schemes on the connectivity of cognitive radio ad hoc networks (CRAHNs), considering secondary users with different antenna types. Innovative proposals like in [3] explore the problem of beamforming optimization in an energy harvesting cognitive radio network, in which the secondary transmitter harvests energy from the primary transmitter and cooperatively relays the information to the primary user. These works present different advantages of exploiting cooperative beamforming for cognitive wireless networks.

Generally, in cognitive radio communications, the channel is often shared amongst different devices with techniques based on opportunistic time division access. However, such techniques do not make use of information on the physical location of the devices. This means that a low-gain omnidirectional antenna is used at the transmitter and the receiver. This results in a very inefficient system, as the signal is transmitted in all directions rather than being towards the desired device. Also, other devices will receive these signals, resulting in a lower signal-to-noise ratio and decreased system performance [4].

Spatial-division multiple-access (SDMA) solves this problem. In SDMA, a high-gain antenna will be used to focus the transmitted signal towards the desired mobile devices. The beamforming multi-antenna technology enables the SDMA configuration. An active antenna system (AAS) contains active electronic components, which are able to manipulate the signal's amplitude and phase (often referred to as weights or current excitations in literature) of each individual antenna element. By manipulating these weights in a smart way, the AAS is able to steer the signal towards a certain direction and control the side lobes, avoiding interference with primary users and improving the received signal strength. This creates a high-gain antenna, resulting in a more efficient system with less system interference. In cognitive radio networks, beamforming is a promising technology to improve the spectrum efficiency. The concept of beamforming is depicted in Fig. 1.

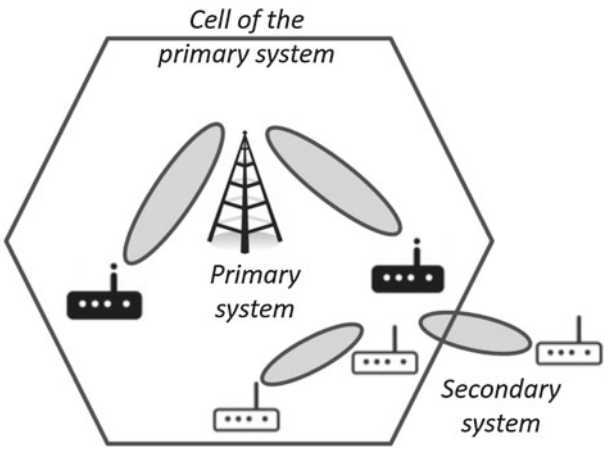

Fig. 1 Cognitive radio network with beamforming support

The primary and secondary systems are in the same region and equipped with array antennas to support beamforming. The spectrum sharing would not be possible with omnidirectional antennas due to the mutual interference.

Determining the weights of the individual antenna elements in a smart way in order to create a flexible beamformer is a challenging task. Examples of weighting schemes are the Dolph–Chebyshev polynomials [5] and the genetic algorithms [6]. However, the Dolph–Chebyshev polynomials do not take the E-field pattern of the individual antenna elements into account, resulting in inaccurate beam steering. The genetic algorithms on the other hand can cope with different E-field patterns of the individual antenna elements and therefore generate accurate beam steering results. However, the genetic algorithms are often computationally intensive, resulting in an increased design time and execution delays.

In this chapter, a fast, flexible, and accurate algorithm is presented in order to find weights that make it possible to steer the signal in a certain direction and, at the same time, control the side lobes of the radiation pattern. Section 2 provides the reasons for choosing an algorithm for steering the total radiated power instead of steering one field component. Section 3 is devoted to the developed iterative algorithm, which is thoroughly explained. Section 4 briefly describes the simulated antenna and Sect. 5 shows the algorithm in practice. In the last section, a conclusion will be drawn regarding the performance of the presented algorithm.

2 Steering Field Versus Steering Power

In literature, one will often find algorithms for shaping radiation patterns, which only focus on steering one field component [5, 7, 8]. However, since the polarization of a mobile wireless link is often not fixed and/or known, it makes sense to

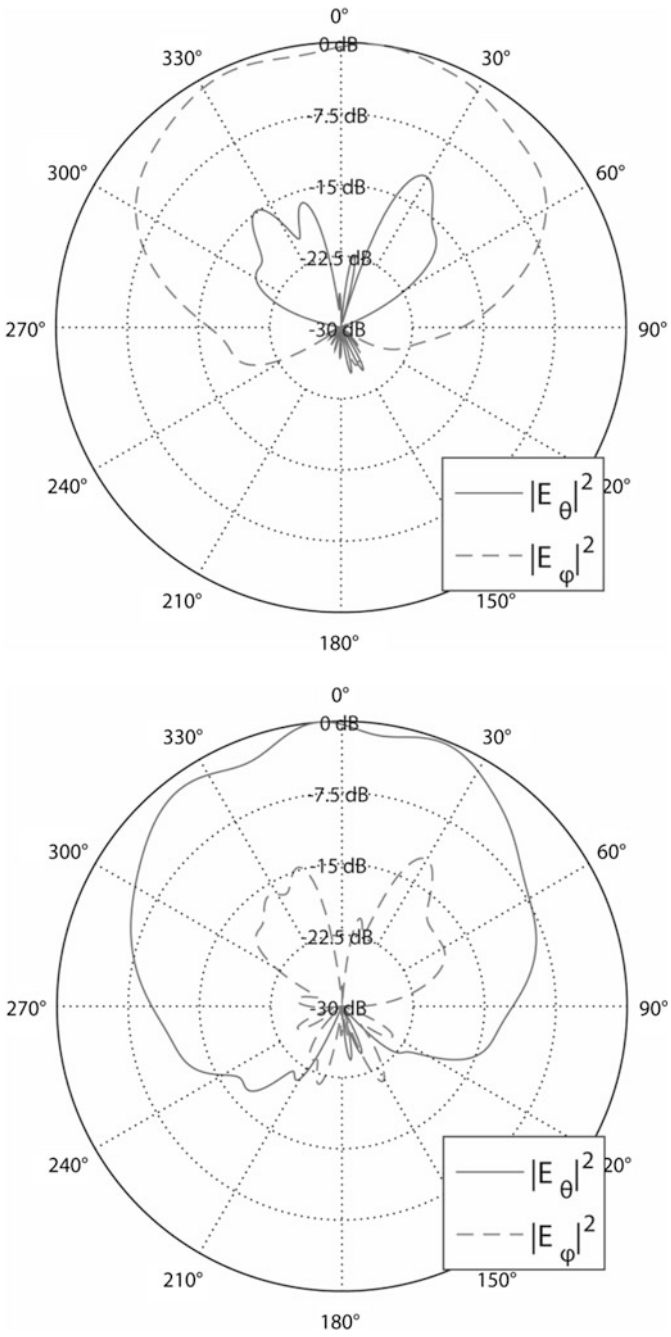

Fig. 2 Planar cuts in the azimuth plane (*upper*) and elevation plane (*lower*) of a simulated patch antenna

maximize the total radiated power (i.e., the combination of E_θ and E_ϕ) instead of maximizing one field component.

Next to that, microstrip patch antennas are very popular nowadays. This is mainly because microstrip patch antennas are low-profile antennas that have a number of advantages over other antennas. Some of these advantages are being lightweight, inexpensive, easy to manufacture, and electronics can be integrated very easily with these antennas [9]. The patch antenna can be considered as an aperture antenna [10]. For an ideal aperture antenna, it is known that in one principal plane (say azimuth plane), one of the field components of the E-field is equal to 0, while in the other principal plane (say elevation plane), the other field component of the E-field is equal to 0 [10]. This is shown in Fig. 2; in the azimuth plane the θ-component of the E-field is very low compared to the ϕ-component, whereas the θ-component of the E-field dominates over the ϕ-component in the elevation plane. It becomes very difficult to steer the E-field in the azimuth, as well as in the elevation plane, when the E-field itself is almost non-existent in some regions. In other words, with conventional patch antennas, or other aperture antennas, it is hard (if not impossible) to steer one field component in both the azimuth and the elevation planes. Therefore, an algorithm dedicated to steering the total radiated power is desired.

3 Algorithm for Shaping the 3D Radiation Pattern

3.1 Introduction to the Algorithm

One of the problems in designing an AAS that supports beamforming is how to determine current excitations in order to synthesize a desired radiation pattern. The presented algorithm is derived from the algorithm for a linear AAS, as presented in [11], and is extended to be valid for planar arrays. The algorithm becomes non-linear since the total radiated power is considered instead of one field component, as discussed in Sect. 2. Therefore, the algorithm does not have closed-form solutions, which is a disadvantageous feature in terms of convergence speed. However, a typical calculation still only takes a few seconds on an average notebook for an AAS containing 16 antenna elements. Next to that, it takes the E-field patterns for the individual antenna elements into account, which highly improve the accuracy. The normalized far-field radiation pattern is defined as:

$$F(\theta,\phi) = \frac{|E_\theta(\theta,\phi)|^2 + |E_\phi(\theta,\phi)|^2}{\max_{(\theta,\phi)}\left(|E_\theta(\theta,\phi)|^2 + |E_\phi(\theta,\phi)|^2\right)} \tag{1}$$

with $E_\theta(\theta,\phi)$ and $E_\phi(\theta,\phi)$ the E-field component in the θ and ϕ-direction, respectively. The E-field contributions can be written as:

$$E_\theta(\theta,\phi) = \underline{w}^\dagger \underline{v}_\theta(\theta,\phi)$$
$$E_\phi(\theta,\phi) = \underline{w}^\dagger \underline{v}_\phi(\theta,\phi) \tag{2}$$

with the dagger † defined as the Hermitian transpose operator, with $\underline{w}$ an $N \times 1$-vector containing the complex weights of the N individual antenna elements and $\underline{v}_\theta(\theta,\phi)$ and $\underline{v}_\phi(\theta,\phi)$ the steering vectors, which are also $N \times 1$-vectors, and are defined as:

$$\underline{v}_\theta(\theta,\phi) = \begin{bmatrix} g_{1,\theta}(\theta,\phi) \\ g_{2,\theta}(\theta,\phi) \\ \vdots \\ g_{N,\theta}(\theta,\phi) \end{bmatrix}, \quad \underline{v}_\phi(\theta,\phi) = \begin{bmatrix} g_{1,\phi}(\theta,\phi) \\ g_{2,\phi}(\theta,\phi) \\ \vdots \\ g_{N,\phi}(\theta,\phi) \end{bmatrix} \tag{3}$$

Here $g_{n,\theta}(\theta,\phi)$ and $g_{n,\phi}(\theta,\phi)$ are the complex E-field patterns of the θ and ϕ-component, respectively, of the nth antenna element. Since scaled versions of the complex weights will produce a scaled version of the radiation pattern, one can always normalize the radiation pattern by scaling the complex weights. Therefore, from now on, the normalization factor in Eq. (1) will be omitted.

The complex E-field patterns of the individual antenna elements have to be extracted from the simulation software or measured using a real antenna. In both cases, the pattern will consist of samples. In order for the algorithm to work properly, it is important that the samples of the complex E-field patterns are, in terms of degrees, equally spaced in the θ and ϕ-directions. The number of samples in the θ and ϕ-directions are indicated by L_θ and L_ϕ, respectively. Next to that, the kth sample in the θ-direction is indicated by θ_k and the l^{th} sample in the ϕ-direction is indicated by ϕ_l.

The goal of this algorithm is to shape the radiation pattern; the main lobe has to be steered in a certain direction and the side lobes have to be suppressed to a certain level. In addition, it is desired to minimize the total contribution to the radiation pattern in the direction other than the direction of pointing. This unwanted radiation will be referred to as interference in the remainder of this chapter.

In the proposed algorithm, the final radiation pattern will be obtained using an iterative procedure. In the first step, a method to minimize the overall interference, while maintaining the main lobe in a certain direction, will be presented. This is formulated in a nonlinear constrained least squares minimization problem. When this first step is completed, an iterative method is presented to make sure that the side lobes are suppressed to a certain level, while maintaining the old constraints.

3.2 Interference Minimization and Steering the Main Lobe

In mathematics, minimizing the interference can be expressed as follows:

$$\min_{\underline{w}} \underline{w}^{\dagger} \mathbf{A} \underline{w} \tag{4}$$

with $\mathbf{A}$ the covariance matrix defined as:

$$\mathbf{A} = \sum_{k=1}^{L_\theta} \sum_{l=1}^{L_\phi} e\,(k,l)\, \mathbf{V}_{kl} \sin\,(\theta_k) \tag{5}$$

with

$$\mathbf{V}_{kl} = \underline{v}_\theta(\theta_k, \phi_l)\underline{v}_\theta^{\dagger}(\theta_k, \phi_l) + \underline{v}_\phi(\theta_k, \phi_l)\underline{v}_\phi^{\dagger}(\theta_k, \phi_l) \tag{6}$$

and

$$e\,(k,l) = \begin{cases} 0 & \text{if the main lobe contains } (\theta,\phi) = (k,l) \\ 1 & \text{otherwise} \end{cases} \tag{7}$$

In these formulas, a few things have to be clarified. First of all, the goal is to minimize the interference. The total unweighted contribution to the radiation pattern is collected by the covariance matrix $\mathbf{A}$. In order to capture only the unweighted interference, instead of also capturing the radiation caused by the main lobe, the term of Eq. (7) is introduced. This concept is shown in Fig. 3. Here, the main lobe is pointed to $\theta = \phi = 70°$, and the expected beamwidth in both the θ and ϕ-direction is 40°. One can see in Fig. 3 that the introduced e-parameter is equal to 0 in the region around the main lobe, so the desired unweighted radiation is not included in the covariance matrix $\mathbf{A}$.

Since the algorithm is developed using spherical coordinates, a correction factor needs to be applied. This is resembled by the $\sin\,(\theta_k)$-term in Eq. (5).

So, in other words, in Eq. (5) all the contributions of the unweighted field patterns are summed, except for the contributions containing the main lobe, and then Eq. (4) calculates the weights that minimize these contributions.

In order to make sure that the main lobe is pointed to a certain direction, some constraints have to be defined parallel to the minimization problem formulated in Eq. (4). First of all, in order to not end up with a trivial solution, the radiation pattern has to be equal to a positive number in the direction of pointing. Here the radiation pattern will be chosen equal to 1 in the direction of pointing in order to avoid an extra normalization step. Next to that, the radiation pattern must have a local maximum in the direction of pointing. This can be achieved by forcing the partial derivatives of the radiation pattern, with respect to θ and ϕ, to be zero.[1] This can be expressed in mathematics in the following way:

[1]To be mathematically more precise, the second-order partial derivatives with respect to θ and ϕ should also be constrained to be negative in order to ensure a peak [7]. However, this constraint is omitted since in most practical situations this will be satisfied.

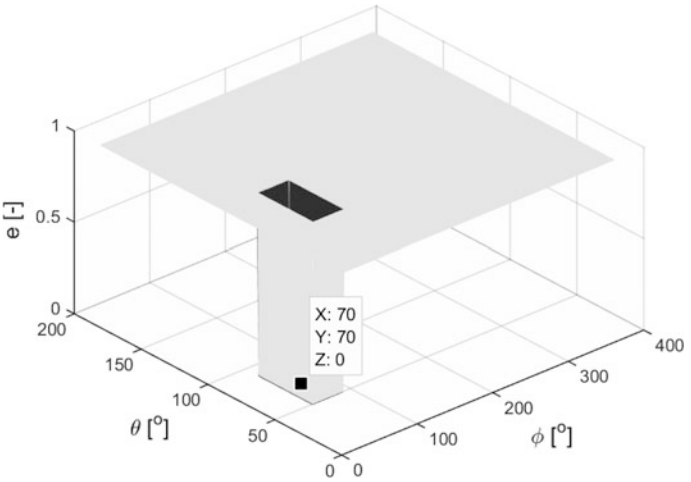

Fig. 3 Visualization of the e-parameter as a function of θ and ϕ

$$F(\theta_0, \phi_0) = 1 \tag{8}$$

$$\left.\frac{\partial F(\theta, \phi)}{\partial \theta}\right|_{(\theta, \phi) = (\theta_0, \phi_0)} = 0 \tag{9}$$

$$\left.\frac{\partial F(\theta, \phi)}{\partial \phi}\right|_{(\theta, \phi) = (\theta_0, \phi_0)} = 0 \tag{10}$$

with θ_0 and ϕ_0 the θ and ϕ-coordinate of the desired pointing angle. Since the radiation pattern consists of samples, one has to use a numerical differentiation method, such as the Finite Difference Method, to determine the partial derivatives of Eqs. (9) and (10).

In order to keep the equations readable, the following shorthand notations will be used:

$$\begin{aligned} \underline{v}_\theta(\theta_0, \phi_0) &= \underline{v}_\theta^0 \\ \underline{v}_\phi(\theta_0, \phi_0) &= \underline{v}_\phi^0 \\ \left.\frac{\partial x(\theta, \phi)}{\partial \theta}\right|_{(\theta, \phi) = (\theta_0, \phi_0)} &= \partial_\theta^0 x \\ \left.\frac{\partial x(\theta, \phi)}{\partial \phi}\right|_{(\theta, \phi) = (\theta_0, \phi_0)} &= \partial_\phi^0 x \end{aligned} \tag{11}$$

with $x(\theta, \phi)$ an arbitrary function. Equation (8) can be rewritten using Eqs. (1) and (2) as:

$$F(\theta_0,\phi_0)=\underline{w}^{\dagger}\underline{v}_{\theta}^{0}(\underline{v}_{\theta}^{0})^{\dagger}\underline{w}+\underline{w}^{\dagger}\underline{v}_{\phi}^{0}(\underline{v}_{\phi}^{0})^{\dagger}\underline{w}=\underline{w}^{\dagger}\mathbf{V}\underline{w}=1$$

with

$$\mathbf{V}=\underline{v}_{\theta}^{0}(\underline{v}_{\theta}^{0})^{\dagger}+\underline{v}_{\phi}^{0}(\underline{v}_{\phi}^{0})^{\dagger} \tag{12}$$

With proper use of the product rule for derivatives, Eq. (9) can be written as:

$$\partial_{\theta}^{0}F=\underline{w}^{\dagger}\mathbf{V}_{\partial\theta}\underline{w}=0$$

with

$$\mathbf{V}_{\partial\theta}=\partial_{\theta}^{0}\underline{v}_{\theta}(\underline{v}_{\theta}^{0})^{\dagger}+\underline{v}_{\theta}^{0}\partial_{\theta}^{0}\underline{v}_{\theta}^{\dagger}+\partial_{\theta}^{0}\underline{v}_{\phi}(\underline{v}_{\phi}^{0})^{\dagger}+\underline{v}_{\phi}^{0}\partial_{\theta}^{0}\underline{v}_{\phi}^{\dagger} \tag{13}$$

On the same argument, Eq. (10) can be written as:

$$\partial_{\phi}^{0}F=\underline{w}^{\dagger}\mathbf{V}_{\partial\phi}\underline{w}=0$$

with

$$\mathbf{V}_{\partial\phi}=\partial_{\phi}^{0}\underline{v}_{\theta}(\underline{v}_{\theta}^{0})^{\dagger}+\underline{v}_{\theta}^{0}\partial_{\phi}^{0}\underline{v}_{\theta}^{\dagger}+\partial_{\phi}^{0}\underline{v}_{\phi}(\underline{v}_{\phi}^{0})^{\dagger}+\underline{v}_{\phi}^{0}\partial_{\phi}^{0}\underline{v}_{\phi}^{\dagger} \tag{14}$$

In summary, the constraints are as follows:

$$\begin{aligned}
F(\theta_0,\phi_0)&=\underline{w}^{\dagger}\mathbf{V}\underline{w}=1\\
\left.\frac{\partial F(\theta,\phi)}{\partial\theta}\right|_{(\theta,\phi)=(\theta_0,\phi_0)}&=\underline{w}^{\dagger}\mathbf{V}_{\partial\theta}\underline{w}=0\\
\left.\frac{\partial F(\theta,\phi)}{\partial\phi}\right|_{(\theta,\phi)=(\theta_0,\phi_0)}&=\underline{w}^{\dagger}\mathbf{V}_{\partial\phi}\underline{w}=0
\end{aligned} \tag{15}$$

3.3 Solving the Real Counterpart

The minimization problem formulated in Eq. (4), in combination with the constraints defined in Eq. (15), is a complex minimization problem, with no direct possible solution [12]. However, this problem can be expressed in a real counterpart and then a solution can be found [12]. This gives the following minimization problem:

$$\min_{\tilde{\underline{w}}}\ \tilde{\underline{w}}^{T}\widetilde{\mathbf{A}}\tilde{\underline{w}}$$

under the constraints

$$\begin{aligned}
&\tilde{\underline{w}}^{T}\widetilde{\mathbf{V}}\tilde{\underline{w}}=1\\
&\tilde{\underline{w}}^{T}\widetilde{\mathbf{V}}_{\partial\theta}\tilde{\underline{w}}=0\\
&\tilde{\underline{w}}^{T}\widetilde{\mathbf{V}}_{\partial\phi}\tilde{\underline{w}}=0
\end{aligned} \tag{16}$$

with superscript T defined as the transpose operator, and with:

$$\begin{aligned}
\underline{\tilde{w}} &= \begin{bmatrix} \mathrm{Re}\{\underline{w}\} \\ \mathrm{Im}\{\underline{w}\} \end{bmatrix} \\
\tilde{\mathbf{A}} &= \begin{bmatrix} \mathrm{Re}\{\mathbf{A}\} & -\mathrm{Im}\{\mathbf{A}\} \\ \mathrm{Im}\{\mathbf{A}\} & \mathrm{Re}\{\mathbf{A}\} \end{bmatrix} \\
\tilde{\mathbf{V}} &= \begin{bmatrix} \mathrm{Re}\{\mathbf{V}\} & -\mathrm{Im}\{\mathbf{V}\} \\ \mathrm{Im}\{\mathbf{V}\} & \mathrm{Re}\{\mathbf{V}\} \end{bmatrix} \\
\tilde{\mathbf{V}}_{\partial\theta} &= \begin{bmatrix} \mathrm{Re}\{\mathbf{V}_{\partial\theta}\} & -\mathrm{Im}\{\mathbf{V}_{\partial\theta}\} \\ \mathrm{Im}\{\mathbf{V}_{\partial\theta}\} & \mathrm{Re}\{\mathbf{V}_{\partial\theta}\} \end{bmatrix} \\
\tilde{\mathbf{V}}_{\partial\phi} &= \begin{bmatrix} \mathrm{Re}\{\mathbf{V}_{\partial\phi}\} & -\mathrm{Im}\{\mathbf{V}_{\partial\phi}\} \\ \mathrm{Im}\{\mathbf{V}_{\partial\phi}\} & \mathrm{Re}\{\mathbf{V}_{\partial\phi}\} \end{bmatrix}
\end{aligned} \tag{17}$$

This nonlinear minimization problem has no closed solution. Commercial computational software packages often have an iterative solver, such as the *fmincon* function in MATLAB R2015a, which helps solving this nonlinear minimization problem.

3.4 Suppressing the Side Lobes

The so far proposed computation ensures that the main lobe is at the desired angle, and minimizes the total interference. The goal, however, is not to minimize the total interference but to minimize the maximum possible interference in any direction, meaning that the side lobes need to be equalized [5].

To do this, an iterative process is proposed. In each iteration, new weights will be calculated. This can be written as:

$$\underline{w}_{n+1} \leftarrow \underline{w}_n + \Delta\underline{w}. \tag{18}$$

Although new weights have to be found to equalize the side lobes, the constraints, which were defined earlier, still have to be met. Also, while the weights are being changed, the added interference must be as minimal as possible. This can be expressed in mathematics as follows:

$$\min_{\Delta\underline{w}} \quad \Delta\underline{w}^{\dagger}\mathbf{A}\Delta\underline{w}$$

under the constraints

$$\begin{aligned}
(\underline{w}_n + \Delta\underline{w})^{\dagger}\mathbf{V}(\underline{w}_n + \Delta\underline{w}) &= 1 \\
(\underline{w}_n + \Delta\underline{w})^{\dagger}\mathbf{V}_{\partial\theta}(\underline{w}_n + \Delta\underline{w}) &= 0 \\
(\underline{w}_n + \Delta\underline{w})^{\dagger}\mathbf{V}_{\partial\phi}(\underline{w}_n + \Delta\underline{w}) &= 0
\end{aligned} \tag{19}$$

To ensure that the side lobes will be suppressed to a certain level, some extra constraints have to be defined. Of course, only a limited amount of extra constraints can be defined. Since the variable $\Delta\underline{w}$ is an $N \times 1$ vector, in principle, N constraints can be defined in total. However, one has to bear in mind that three constraints have already been imposed in the problem defined in Eq. (19). This means $M_{\max} = N - 3$ side lobes can be controlled in each iteration. The first step is to find the $M_{\max}$ highest peaks in the radiation pattern. Once these locations are known, the following constraint can be introduced to suppress the ith side lobe:

$$(\underline{w}_n + \Delta\underline{w})^{\dagger}\mathbf{V}_i(\underline{w}_n + \Delta\underline{w}) - \underline{w}_n^{\dagger}\mathbf{V}_i\underline{w}_n = f_i$$

with

$$\begin{aligned} f_i &= (R - |c_i|)\frac{c_i}{|c_i|} \\ c_i &= \underline{w}_n^{\dagger}\mathbf{V}_i\underline{w}_n \\ \mathbf{V}_i &= \underline{v}_{\theta}(\theta_i, \phi_i)\underline{v}_{\theta}^{\dagger}(\theta_i, \phi_i) + \underline{v}_{\phi}(\theta_i, \phi_i)\underline{v}_{\phi}^{\dagger}(\theta_i, \phi_i) \\ i &= 1, 2, \ldots, M_{\max} \end{aligned} \tag{20}$$

with θ_i and ϕ_i the θ and the ϕ-coordinate of the location of the ith side lobe and R is the desired side lobe level. In addition to that, c_i is the value of the ith side lobe and f_i resembles the residual amount needed for the ith side lobe to achieve the desired side lobe level.

In the same way as in the previous paragraph, the real counterpart of the new complex minimization problem can be found. This can be expressed as follows:

$$\min_{\Delta\underline{\tilde{w}}} \quad \Delta\underline{\tilde{w}}^T\widetilde{\mathbf{A}}\Delta\underline{\tilde{w}}$$

under the constraints

$$\begin{aligned} &(\underline{\tilde{w}}_n + \Delta\underline{\tilde{w}})^T\widetilde{\mathbf{V}}(\underline{\tilde{w}}_n + \Delta\underline{\tilde{w}}) = 1 \\ &(\underline{\tilde{w}}_n + \Delta\underline{\tilde{w}})^T\widetilde{\mathbf{V}}_{\partial\theta}(\underline{\tilde{w}}_n + \Delta\underline{\tilde{w}}) = 0 \\ &(\underline{\tilde{w}}_n + \Delta\underline{\tilde{w}})^T\widetilde{\mathbf{V}}_{\partial\phi}(\underline{\tilde{w}}_n + \Delta\underline{\tilde{w}}) = 0 \\ &(\underline{\tilde{w}}_n + \Delta\underline{\tilde{w}})^T\widetilde{\mathbf{V}}_i(\underline{\tilde{w}}_n + \Delta\underline{\tilde{w}}) - \underline{\tilde{w}}_n^T\widetilde{\mathbf{V}}_i\underline{\tilde{w}}_n = \tilde{f}_i \end{aligned} \tag{21}$$

with:

$$\begin{aligned} \underline{\tilde{w}}_n &= \begin{bmatrix} \mathrm{Re}\{\underline{w}_n\} \\ \mathrm{Im}\{\underline{w}_n\} \end{bmatrix} \\ \Delta\underline{\tilde{w}} &= \begin{bmatrix} \mathrm{Re}\{\Delta\underline{w}\} \\ \mathrm{Im}\{\Delta\underline{w}\} \end{bmatrix} \\ \tilde{f}_i &= \begin{bmatrix} \mathrm{Re}\{f_i\} \\ \mathrm{Im}\{f_i\} \end{bmatrix} \\ \widetilde{\mathbf{V}}_i &= \begin{bmatrix} \mathrm{Re}\{\mathbf{V}_i\} & -\mathrm{Im}\{\mathbf{V}_i\} \\ \mathrm{Im}\{\mathbf{V}_i\} & \mathrm{Re}\{\mathbf{V}_i\} \end{bmatrix} \end{aligned} \tag{22}$$

and $\widetilde{\mathbf{A}}$, $\widetilde{\mathbf{V}}$, $\widetilde{\mathbf{V}}_{\partial\theta}$ and $\widetilde{\mathbf{V}}_{\partial\phi}$ defined as in Eq. (17). Again, this minimization problem can be solved by an iterative solver from a commercial computational software package. When one follows this procedure, a desired 3D radiation pattern can be constructed.

3.5 *Evaluation of the Algorithm*

The presented algorithm is an iterative algorithm that finds weights which ensure that the main lobe points to a certain direction and that the side lobes are suppressed to a certain level. In the first iteration, the minimization problem given by Eq. (16) reduces the total weighted interference, while pointing the main lobe at the desired steering angle. In the subsequent iterations, the minimization problem formulated in Eq. (21) ensures that the main lobe stays at the desired pointing angle, and minimizes the extra interference caused by the new weights. Next to that, it can suppress $M_{\max}$ side lobes to the desired level in each iteration.

Note that the mathematics presented do not prove that the algorithm converges to a solution. If one tries to suppress side lobes, the algorithm only ensures that, at that certain position, the radiation pattern will be equal to the desired side lobe level in the next iteration. It is possible that at other angles, some side lobes will arise. However, in practice, after a few iterations (typically less than 10) the side lobes will be equalized. This is because the impact of the new weights is minimized according to Eq. (21). This prevents 'randomly' popping up new high side lobes at other angles.

Another point worth mentioning is that sometimes combining certain constraints is not possible. There will always be a trade-off between the number of antenna elements, the desired beamwidth, the desired side lobe level, and the pointing angle. For example, it is very impractical to design a 2×2 planar antenna array and to expect to have a beamwidth of 5°. The algorithm will attempt (but fail) to find a solution, thus resulting in inconsistent patterns. If this occurs, one will need to change the antenna design or relieve the constraints. Besides this, it is advised not to search for the peaks in the back radiation when selecting the side lobes that are to be suppressed. Because of the symmetry, on the other side of the pointing angle, a peak will occur in the back radiation. If one tries to suppress this peak in the back radiation, while keeping the main lobe to a certain level, one will have two conflicting constraints, which will again result in inconsistent patterns. If this occurs, the antenna design has to be changed and one has to make sure that the radiation pattern of the individual antenna elements does not contain too much back radiation.

4 Antenna Design

In order to test the proposed algorithm, a 4×4 planar antenna array has been designed using CST Microwave Studio, Release Version 2014.06. The antenna is designed for the ISM band with a center frequency of 5.8 GHz, but note that this

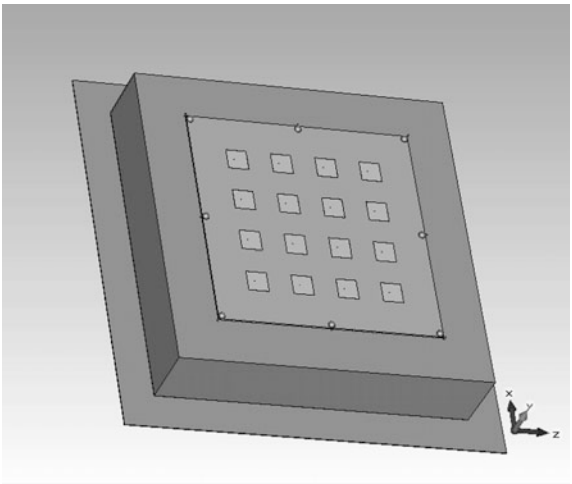

Fig. 4 The CST design of the planar antenna array

algorithm is frequency-independent; the algorithm only requires the complex E-field patterns of the individual antenna elements as input. The 5.8 GHz frequency was selected due to the License Assisted Access (LAA) feature that has been standardized by 3GPP [13].

The individual antenna elements are probe-fed microstrip patch antennas. The patches are made of annealed copper ($\sigma = 5.80 \times 10^7$ S / m), whose length, width, and thickness are 11.7 mm, 11.7 mm, and 35 µm, respectively. The radius of the probe is 0.2 mm and the position of the probe is 1.75 mm out of the center of the patch. The substrate is made of Taconic RF-43 ($\varepsilon_r = 4.3$, $\tan\delta = 0.0033$) and has a thickness of 1.02 mm. The substrate is placed on top of an aluminum ($\sigma = 3.56 \times 10^7$ S / m) box and reflector. The box and reflector have been constructed in order to store electronics and facilitate mounting of the antenna on a base station. The dimensions of this box and reflector have been optimized in order to reduce as much back radiation as possible. The box has a length, width, and height of 180.91 mm, 180.91 mm, and 38.77 mm, respectively, and the reflector has length and width of 219.68 mm. The thickness of the aluminum is chosen as 1 mm. The CST design is shown in Fig. 4.

5 Validation of the Algorithm

Figure 5 presents the iterative process in four contour plots. In this example, $\theta_0 = \phi_0 = 70°$ and $R = -20$ dB.

Note that for this antenna, $\theta = \phi = 90°$ is the broadside direction. At the first iteration, one will notice that the steering angle is nicely obtained at $\theta_0 = \phi_0 = 70°$,

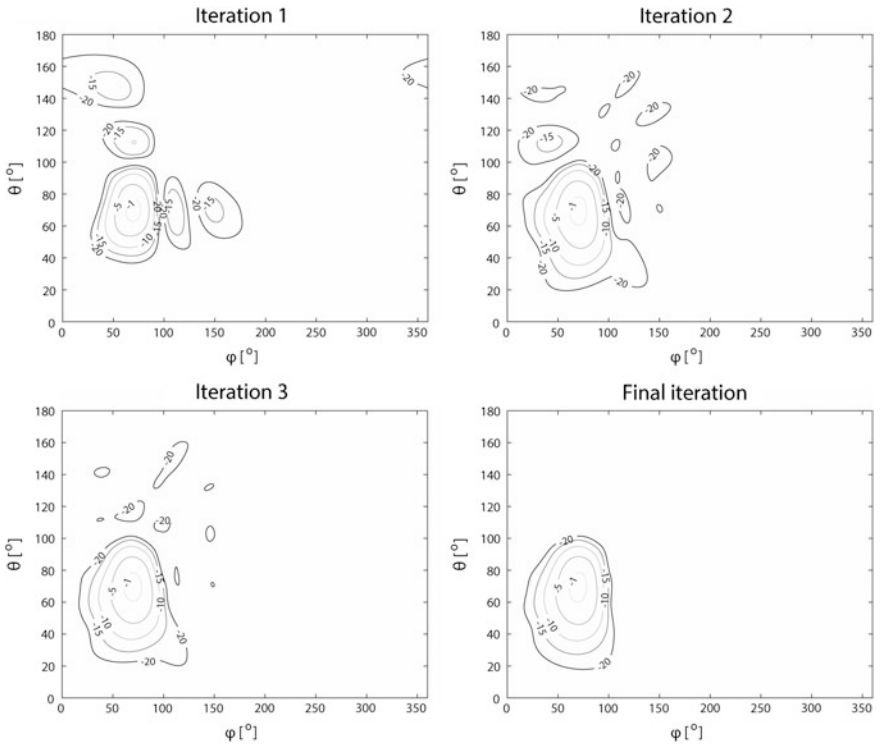

Fig. 5 Contour plot of the radiation pattern of different iterations of the algorithm

Table 1 Normalized current excitations of the individual antenna elements of the final iteration using the following parameters: $\theta_0 = \phi_0 = 70°$, $R = -20$ dB

#	Amplitude	Phase [°]	#	Amplitude	Phase [°]
1	0.170	141.74	9	0.438	–8.19
2	0.256	97.76	10	0.697	–67.45
3	0.576	11.95	11	0.911	–120.15
4	0.242	–128.94	12	0.835	–179.11
5	0.477	60.35	13	0.276	–89.13
6	1.000	0.00	14	0.497	68.78
7	0.689	–39.76	15	0.619	175.99
8	0.480	–108.04	16	0.518	82.05

but the side lobes are rather high; three side lobes exceed −15 dB, and one of the side lobes is even higher than −10 dB. In the following iterations, the main lobe is still positioned at the desired angle, whereas the side lobes are slowly being suppressed. This eventually results in a radiation pattern with no side lobes exceeding −20 dB. The weights associated with this radiation pattern are listed in Table 1 and

were inserted in CST. This resulted in an AAS with a gain of 15.1 dBi, as shown in Fig. 6.

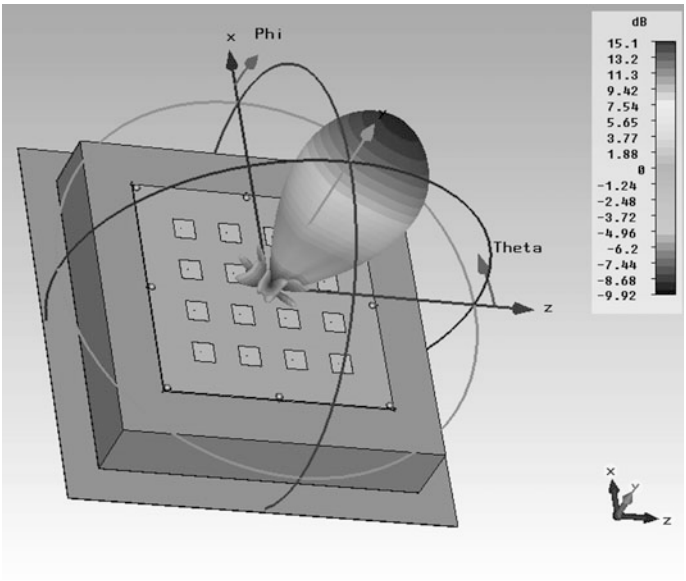

Fig. 6 The CST design including the shaped 3D radiation pattern

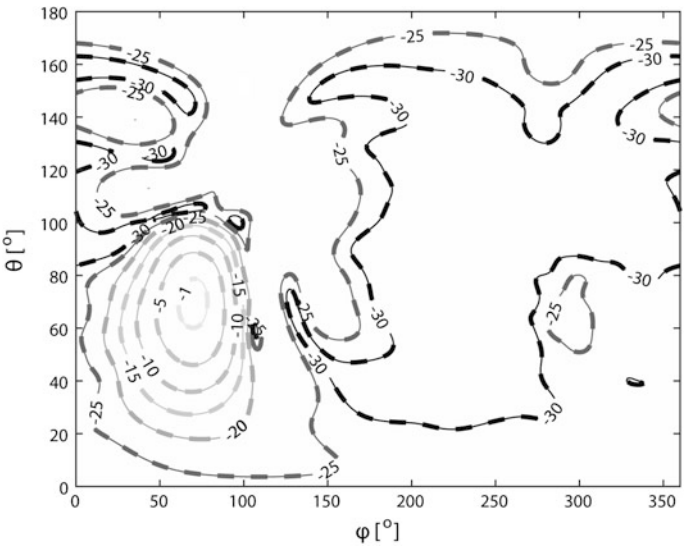

Fig. 7 Contour plot of the radiation pattern in CST (*solid*) and MATLAB (*dashed*)

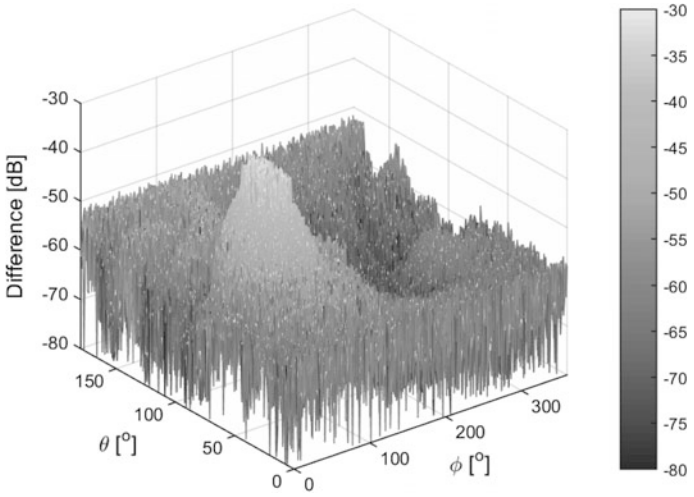

Fig. 8 Absolute difference between the radiation patterns from the proposed algorithm programmed in MATLAB and the simulated model of CST

As stated in Sect. 3.5, if one tries to suppress side lobes, often at other angles, other side lobes will rise. Note that this behavior is also shown in Fig. 5. In the contour plot of iteration 1, only four side lobes of more than −20 dB are present, whereas in the following iteration, 10 side lobes exceeding −20 dB are present.

In order to verify the proposed algorithm, the radiation patterns of CST and the algorithm, programmed in MATLAB, were compared. A contour plot of both models is shown in Fig. 7.

This contour plot shows very good agreement between both radiation patterns. The absolute difference between these two radiation patterns is shown in Fig. 8. Next to that, the absolute difference was calculated for different combinations of steering angles and side lobe levels, and was found to be maximally around −30 dB.

6 Conclusion

In this chapter, a fast, flexible, and accurate iterative algorithm to find current excitations in order to shape the 3D radiation pattern of an active antenna system to enable beamforming for cognitive radio networks has been presented. The algorithm forces the side lobes of the radiation pattern to a certain level, keeps the main lobe to the desired pointing angle, and minimizes the unwanted radiation in all other directions. The algorithm is independent of the design frequency and can be used for every arbitrary antenna array, since the only input needed are the complex E-field patterns of the individual antenna elements. This also means that the

algorithm can be applied not only in the design phase using simulated data, but also in the calibration phase using measured data. Next, the algorithm converges typically in the order of seconds on an average notebook for an AAS containing 16 antenna elements. A 4×4 planar antenna array has been designed using CST in order to verify the algorithm. The estimated radiation pattern of the algorithm was compared to the results obtained from CST, and the absolute difference was found to be maximally around -30 dB.

Acknowledgements The CPqD LTE 450 Project was supported by FUNTTEL (Telecommunications Technology Development Fund), from the Ministry of Communications.

We thank Prof. André L. F. de Almeida, Ph.D., from the Federal University of Ceará (UFC) and Prof. Bart Smolders, Ph.D., from Eindhoven University of Technology (TU/e), who have provided technical and administrative support, which greatly assisted the research.

References

1. Yucek T, Arslan H (2009) A survey of spectrum sensing algorithms for cognitive radio applications. IEEE Commun Surv Tutor 11(1)
2. Dung LT, Hieu TD, An B, Kim BS (2016) How does beamforming influence the connectivity of cognitive radio ad-hoc networks? In: 2016 International symposium on computer, consumer and control (IS3C). Xi'an, China
3. Hu S, Ding Z, Ni Q, Yuan Y (2016) Beamforming optimization for full-duplex cooperative cognitive radio networks. In: 2016 IEEE 17th international workshop on signal processing advances in wireless communications (SPAWC). Edinburgh, United Kingdom
4. Haykin S, Moher M (2005) Modern wireless communications, 1st edn. Pearson Education Inc, New Jersey
5. Hansen RC (2009) Phased array antennas, 2nd edn. Wiley, New York
6. Rahmat-Samii Y, Michielssen E (1999) Electromagnetic optimization by genetic algorithms, 1st edn. Wiley, New York
7. Tseng CY, Griffiths LJ (1992) A simple algorithm to achieve desired patterns for arbitrary arrays. IEEE Trans Signal Process 40(11):2737–2746
8. Visser HJ (2005) Array and phased array antenna basics, 1st edn. Wiley, New York
9. Orban D, Moernaut GJK (2009) The basics of patch antennas. RF Globalnet Newsletter (September 2009)
10. Visser HJ (2012) Antenna theory and applications, 1st edn. Wiley, New York
11. Ferreira DB, de Paula CB, Nascimento DC (2013) Design techniques for conformal microstrip antennas and their arrays. In: Kishk A (ed) Advancement in microstrip antennas with recent applications. Rijeka, pp. 3–31. doi:10.5772/53019. (InTech, 2013)
12. Tseng CY (1992) Minimum variance beamforming with phase-independent derivative constraints. IEEE Trans Antennas Propag 40(3):285–294
13. 3GPP TR 36.889 (2015) Feasibility study on licensed-assisted access to unlicensed spectrum

Cognitive Radio Networks

D. Carrillo

Abstract A cognitive radio can be defined by the capability of being aware of its environment and the internal state and, based on the knowledge of these elements and any stored pre-defined objectives, can dynamically adapt, make, and implement decisions about its behavior. Among the applications of cognitive radio, the most widely explored regards the improvement of spectrum bands usage, also known as white spaces. This paper presents a review of cognitive radio framework that facilitates the understanding and implementation of spectrum management functions of a typical-cognitive radio network project.

1 Introduction

Many Internet services are provided through wireless channels, specially using smartphones through cellular access using metropolitan area networks, which are complemented by extensible deployment of local areas with Wi-Fi at every home around the world. Currently, spectrum allocation for wireless services indicates that most frequencies below 6 GHz have already been occupied. Considering future wireless trends, the integration of emerging fifth generation (5G) technologies will require a special task force, especially for large-scale networks [1]. In contrast, many research studies indicate that a large portion of the licensed spectrum is not used [2]. The idea is to take advantage of instantaneous spectrum availability enabling secondary users to operate on licensed spectrum.

In order to solve the lack of available frequency bands for secondary users, cognitive radio technology can be employed to improve spectrum usage [3]. According to the federal communications commission (FCC) [4], cognitive radios (CR) are defined as radio systems that continuously perform spectrum sensing,

D. Carrillo (✉)
CPqD Foundation, Campinas, Brazil
e-mail: dickm@cpqd.com.br

A. Paradisi et al. (eds.), *Cognitive Technologies*, Telecommunications and Information Technology, DOI 10.1007/978-3-319-53753-5_8

dynamically identify unused spectrum, and then operate in those spectrum holes where the licensed (primary) radio systems are idle. This communication paradigm can dramatically enhance spectrum efficiency for emerging 5G services [5].

Cognitive radio is based on two main processes, which are described in following paragraphs. The first process involves performing spectrum sensing in order to identify any primary user activity and define strategies for opportunistically occupying the spectrum. However, secondary users hardly ever can communicate based on the information detected in the cognitive environment, because, in some cases, full spectrum sensing requires continuous sensing, which is not an efficient energy solution especially for low-cost battery-powered wireless nodes.

Secondary users have the possibility to sense specific bands and, after inferring channel occupancy, they must select the channel over which transmission is possible [6]. In spectrum sensing, it is important to maintain high sensitivity performance in order to detect weak primary user (PU) signals [7]. Other important aspect of spectrum sensing is that secondary users should vacate the occupied segments when primary user transmission power is weak. Generally, spectrum sensing techniques [5] fall into three categories: energy detection [8], matched filter detection [9], and cyclostationary feature detection [10]. If secondary users have limited information on primary user signals, then the energy detector is optimal [8]. Considering this assumption, it is hard to distinguish between a white spectrum and a weak signal attenuated by deep fading. In order to improve the reliability of spectrum sensing, radio cooperation exploiting spatial diversity among secondary users has been proposed in [7] and [11].

The second process comprises optimally managing information obtained during spectrum sensing in order to optimize cognitive network throughput, receiver–transmitter synchronization, mobility issues of secondary users and primary user protection against interferences. Most of these features should be provided by medium access control (MAC) in opportunistic spectrum access (OSA) networks [5, 6]. The importance of MAC in maintaining quality of service (QoS) is described in the next paragraph.

A general criterion for every CR regarding primary user protection is that secondary users should select vacant channels when primary users access licensed bands. However, ensuring QoS of primary users sometimes depends on the selected service. In some cases, QoS can be maintained by introducing some interference-power constraints in which both primary and secondary users operate under certain interference.

This paper is organized as follows: Sect. 3 presents a general description of the cognitive radio framework. In the following sections, the authors describe all elements of the cognitive radio framework. Additionally, Sect. 4 gives a detailed description of the spectrum-sensing feature. Section 5 describes main concepts of spectrum decision. Spectrum sharing information is provided in Sect. 6. Section 7 presents some features related to spectrum mobility for cognitive radio networks.

2 Cognitive Radio Networks

Some features uniquely characterize Cognitive radio networks, such as choice of transmission spectrum, multi-hop/multi-spectrum transmission, and distinguishing mobility from PU activities. The following paragraphs describe these features, which result from an ever-changing spectrum environment and aim at protecting the transmission of primary user signals within the spectrum of channels.

- Choice of transmission spectrum: CR technology allows for the spectrum bands to be distributed over a broad frequency range, varying over space and time and presenting to each user available frequencies according to primary user dynamics. In contrast to other radio networks, protecting primary user transmission is an aspect of vital importance in cognitive radio networks.
- Multi-hop/multi-spectrum transmission: In CR, radio signals travel through multiple hops in a number of channels available in the spectrum. Spectrum switching, in turn, is increased by frequent PU arrivals. In this scenario, ensuring end-to-end QoS is not a simple task, as it depends on a number of factors such as: the traffic load, the number of channels and spectrum bands used in the path, the number of PUs and events detected in the spectrum and the application of periodic spectrum sensing, among others.
- Distinguishing mobility from PU activity: Usually node mobility can lead to frequent disconnections. The cognitive radio approach prevents a node from transmitting as soon as a PU is detected on the spectrum, even when no mobility is assumed. Moreover, CR employs spectrum sensing techniques and spectrum recovery mechanisms.

a. Cognitive radio framework
A cognitive radio scenario encompasses the primary network and the CR network (CRN) components, as shown in Fig. 1. The existing network comprises primary users (PUs) already licensed to operate in a certain spectrum band, including primary base stations to control their operations/activities. Primary users have spectrum access priority and should not be affected by unlicensed users. Because no license to operate in a desired band has been granted to the CR network, CR users must have an additional functionality in order to share the licensed spectrum band. Besides, CRN also takes advantage of mobility, through which users can communicate with each other using multi-hop techniques on both licensed and unlicensed spectrum bands. Thus, any activity in CR networks depends on local observations.
A framework for cognitive radio networks on a specific scenario where nodes are part of an ad hoc network is proposed in [12]. A cognitive radio network requires some operations, i.e., the configuration of the so-called cognitive cycle (components of the cognitive radio framework), which consists of four spectrum management functions: spectrum sensing, spectrum decision, spectrum sharing, and spectrum mobility. The following are the main features of the spectrum management functions [13]:

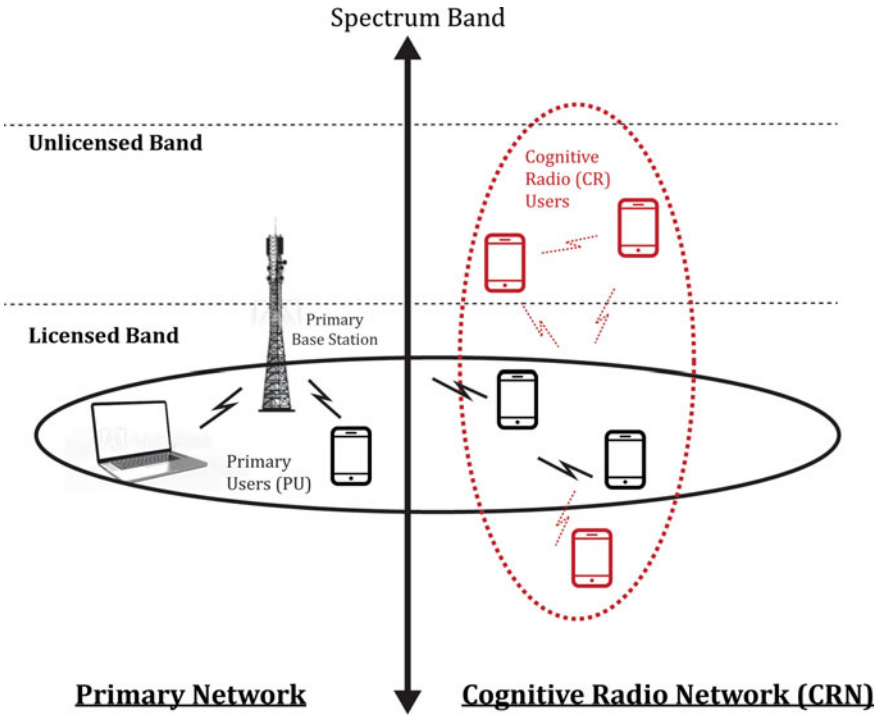

Fig. 1 Cognitive radio network components

- Spectrum sensing: Only unused portions of the spectrum can be allocated to CR users. Monitoring available spectrum bands and detecting spectrum holes are tasks performed by CR users. Sensing the spectrum and layering protocols to provide information on spectrum availability are basic functionalities in CR networks. Spectrum sensing relates to other spectrum management functions and makes use of sensibility functions to provide information on primary user activities, and protection against any interference generated by CR networks;
- Spectrum mobility: When primary users access specific portions of the spectrum occupied by CR users, the latter should vacate the spectrum immediately and find other vacant portions of the spectrum to continue communication. This is a very dynamic process and requires a new spectrum band to be chosen or a handoff strategy to be applied, detecting the affected links and switching them to a new spectrum band. This requires a collaborative environment, including: spectrum sensing, link layer neighboring discovery strategy, and a connection management scheme that will support the performance of upper layer protocols by mitigating the interference generated by spectrum switching;

- Spectrum decision: Next, CR users must consider the respective QoS requirements in order to select the most appropriate band from the available spectrum. Such requirements include radio environment and statistical behavior of primary users, along with information regarding PU activity. These will provide a basis for designing a dynamic decision algorithm that will encompass spectrum characteristics;
- Spectrum sharing: Assuming that a number of CR users are competing for the spectrum bands and coordinated transmissions should be used to prevent collisions in the overlapping portions of the spectrum, opportunistic sharing is an effective means to allocate spectrum resources and avoid interference in primary users when multiple CR users are involved. In this context, the use of game-theoretical approaches, usually to establish cooperation between players, helps analyze the behavior of selfish CR users and maximize the network usage. A medium access control (MAC) protocol is required in order to facilitate the sensing control and respective assignment of the sensing task to coordinating nodes and the transmission time of dynamic spectrum access.

3 Spectrum Sensing for Cognitive Radio Networks

Spectrum sensing is an important requirement for the design and implementation of CR networks, since it provides the ability to sense the spectrum to detect changes or holes, enabling CR users to cooperatively and opportunistically exploit unused spectrum portions in the primary network. This capability is particularly relevant in the following cases: (1) out-of-band sensing, in which CR users are trying to find available spectrum holes over a wide frequency range as transmission opportunities, and (2) in-band sensing, in which CR users monitor transmissions in spectrum bands to detect the presence of primary networks and avoid interferences [12].

As shown in Fig. 2, the CRN requires the following functionalities for spectrum sensing:

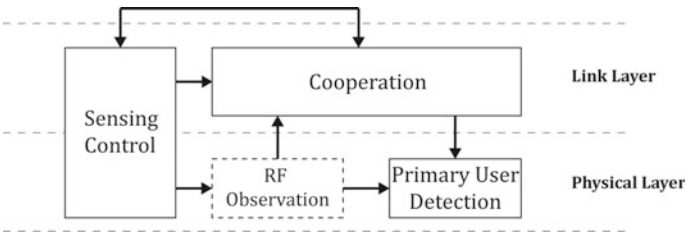

Fig. 2 Spectrum sensing framework for a generic cognitive radio network [12]

- Primary user detection: CR users observe and analyze the local radio environment (both CR and PU), detect the presence of PU transmissions, and promptly identify current spectrum availability;
- Cooperation: All information observed by CR users is exchanged among neighbors thus improving sensing accuracy;
- Sensing control: Distributed coordination for each sensing operation being dynamically performed in the radio environment, reducing the occurrence of false alarms, which can decrease spectrum access opportunities.

In order to make the highest and best use of spectrum, causing as little interference as possible, some functionalities, described in following subsections, are required.

a. Primary user detection
The ongoing transmissions of primary users are usually not known to CR users since there is no real-time interaction between them. Thus, PU detection relies solely on local radio observations performed by CR users. Detection techniques employed by CR users are commonly classified into three groups: [13] primary transmitter detection, primary receiver detection [14], and interference temperature management [15]. Since most of the current research on spectrum sensing in CRN focuses mainly on primary transmitter detection, the following paragraphs present detailed information on this CR feature.
First, both used and unused spectrum bands must be identified in a way that CR signals can be effectively distinguished from a PU transmitter when transmitter detection techniques are employed. Detection sensing involves observations made to the local radio frequency, which are carried out by PU and are based on the following hypothesis model:

$$r(t) = \begin{cases} n(t), & H_0, \\ h\,s(t) + n(t), & H_1, \end{cases} \tag{1}$$

where $r(t)$ is the signal received by the CR user, $s(t)$ is a zero-mean additive white Gaussian noise (AWGN) and h is the amplitude gain of the channel. H_0 is a null hypothesis, which states that there is no licensed user signal in a certain spectrum band. On the other hand, H_1 is an alternative hypothesis, which indicates that there exists some PU signal. Three schemes can be used for the transmitter detection in spectrum sensing: matched filter detection, energy detection, and feature detection [12, 16].

b. Sensing control
Sensing control can enhance spectrum access opportunities without generating interference in primary networks. A sensing controller is responsible for controlling and coordinating sensing operations of CR users and is mainly concerned with: (1) time and frequency parameters required by CR sensing operations to obtain in-band sensing accuracy, and (2) spectrum discovery time of vacant spectrum band in out-of-band sensing.

i. Sensing control: in-band
Most of in-band sensing operations adopt the periodic sensing structure, which provides CR users with limited access to the spectrum, only within transmission periods and followed by sensing (observation) periods. This type of scheme adopts optimized sensing time, leading to stronger signals and less interference. The longer the sensing time, the shorter the transmission time of CR users. In contrast, not only access opportunities are greater when transmission time is longer, but interference as well, since there may be not sufficient sensing information. Thus, selecting proper sensing and transmission time values helps to improve general performance of CR networks.

ii. Sensing control: out-of-band
CRN performance is also defined by the spectrum discovery time, which consists of the time CR users need to find new available spectrum bands (out-of-band sensing). Coordination schemes may be used to assure that as many spectrum opportunities as possible are discovered whilst minimizing delays. This feature is also applicable to spectrum mobility as it works as a mechanism to reduce switching time.
Finding the optimal spectrum sensing order can help minimize delay in out-of-band sensing. Also, sequential sensing can help maximize access opportunities and spectrum searching time.

c. Cooperation
When CR users find unused portions of the spectrum, there may be interferences in the transmission range of primary receivers. Such interference occurs because the observation range of CR users is smaller and usually less efficient than the respective transmission range. Also, multipath fading and shadowing effects also prevent CR users from detecting PU signals. A more accurate detection requires sensing information to be shared among users locally and calls for a common cooperative detection technique to be employed in order to minimize interference in PU outside the observation range of CR users.
A cooperative technique will enable CR users to detect PU activities and share observations with their neighbors, promptly releasing the occupied spectrum. A reliable control channel is the mechanism chosen for discovering neighbors and exchanging sensing information among CR users. Thus, the implementation of CR networks depends strongly on cooperative sensing techniques, encompassing robust neighbor discovery and reliable information exchange.

4 Spectrum Decision for Cognitive Radio Networks

The selection of the best band among the available spectrum bands takes into consideration the QoS application requirements and is called spectrum decision. This rather important process is related to channel characteristics and operations of

PU and involves two steps: (1) gathering information based on local observations of CR users and statistical information of PU; and (2) selecting the most appropriate spectrum band based on such characterization [12]. Spectrum decision consists of the following features:

- Spectrum characterization: Consists of drawing the characteristics of the available spectrum and related PU activity model based on local observations;
- Spectrum selection: Consists of finding the best spectrum band for each hop, which will be determined by the end-to-end link that will meet cognitive radio's QoS requirements;
- Reconfiguration: Consists of reconfiguring communication protocol and hardware and RF front end, based on the radio environment and user's QoS requirements.

Spectrum decision must be performed by CR users in the beginning of the transmission. Figure 3 shows the structure for characterizing the available spectrum bands, which is based on RF observation, and takes into account the received signal strength, interference, and the number of users currently accessing the spectrum. CR users observe that the spectrum availability is not homogeneous, varying over time and space, mostly affected by PU activities. The heterogeneity of the spectrum usage is considered when CR users select the best available spectrum band according to their QoS requirements. Also, the quality of a current session is determined by a spectrum handoff scheme, which will switch to a new spectrum band with minimum quality degradation.

a. Spectrum characterization

   i. Radio environment
   The characterization of spectrum holes is not consistent, varying over time. Because of this, time-varying variables, operating frequency and bandwidth

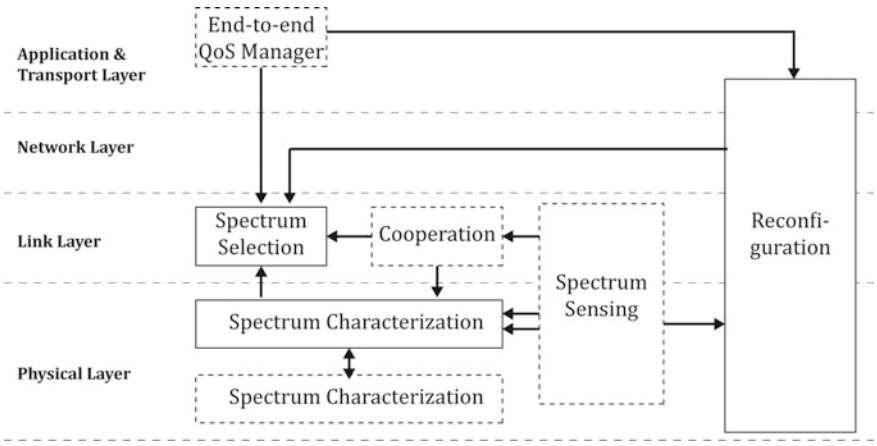

Fig. 3 Spectrum decision structure for cognitive radio networks

parameters must be configured. In addition, parameters must be spectrum-band-specific:

- Interference: The level of interference at the primary receiver defines the permissible power of a CR user, this power is also used to estimate channel capacity;
- Path loss: Path loss depends on signal frequency and distance parameters. The increased operating frequency generates an increased signal path loss, also decreasing transmission range. Thus, an increased path loss requires the allocation of greater transmission power, generating more interference between channels;
- Wireless link errors: The modulation scheme and the interference level of the spectrum band will determine the channel error rate;
- Link layer delay: Different parameters, such as path loss, wireless link error, and interference, require different link layer protocols among spectrum bands, generating different link layer delays.

ii. Primary user activity [1]
The CR network scenario requires a new and dynamic method to identify the statistical behavior of primary networks, commonly referred to as primary user (PU) activity. Estimating PU activity has become a very crucial issue in spectrum decision, as spectrum band may not be available during the entire communication session, which consists of multiple hops with heterogeneous spectrum availability. An attempt to model the PU traffic results in a two-state birth and death process with death rate a and birth rate b, ON (Busy) representing the period used by PU and OFF (Idle) indicating the unused period [17]. In some cases artificial intelligence techniques could be used to identify primary user behavior [18–20].

b. Spectrum selection
As stated in [12], "once the available spectrum bands are characterized, the most appropriate spectrum band should be selected." This selection is based on user's QoS requirements and on the following parameters: transmission data rate, spectrum characteristics, delay bound, acceptable error rate, transmission mode, and bandwidth. Spectrum selection rules are then applied enabling the appropriate spectrum bands to be selected.
Spectrum decision requires a dynamic decision framework that is based on channel conditions and on the user's QoS requirements. Besides, when primary users access the spectrum, CR users cannot use the spectrum effectively, being unable to provide a reliable communication channel over long transmission lengths. Also, when CR users are unable to detect any single spectrum band that meets the user's requirements, multiple radio front ends can be activated to capture non-contiguous spectrum bands for different users and to transmit data simultaneously. When a PU accesses one of the current spectrum bands, or when one of the next hop neighbors is missing, signal transmission remains unaffected.

c. Reconfiguration
Following spectrum decision, the communication system must be reconfigured. CR users are required to select the proper communication modules, including the physical layer technology and upper layer protocols of signals, which are dynamically dependent on application requirements and spectrum features.

5 Spectrum Sharing for Cognitive Radio Networks

Shared wireless channels require a cluster-based coordination approach in order to control packet transmission attempts between CR users. Spectrum sharing provides a specific scheme for: (1) coordinating multiple CR users trying to access the spectrum, and (2) changing parameters to make more flexible communication resources used among licensed and unlicensed bands, thus maintaining the QoS, without causing any degradations to primary users. Spectrum sharing is also performed during a communication session using the spectrum band, and includes a medium access control (MAC) protocol and management functionality, which enable a more efficient resource allocation of resources. Nevertheless, dynamic spectrum access, which enables the coexistence of CR networks with primary users, and the wide range of available spectrum are major challenges for spectrum sharing.

Spectrum sharing techniques encompass two types of solutions, i.e., intra-network spectrum sharing, in which CR users try to access available spectrum bands without generating interference in primary users, and internetwork spectrum sharing for multiple CR networks being deployed in overlapping spectrum [13]. Furthermore, the same way as to spectrum sensing, spectrum sharing requires that CR users have all CR sharing capabilities. Functional blocks for spectrum sharing are described in Fig. 4. Spectrum sharing and spectrum sensing comprise similar functionalities in CRN as follows:

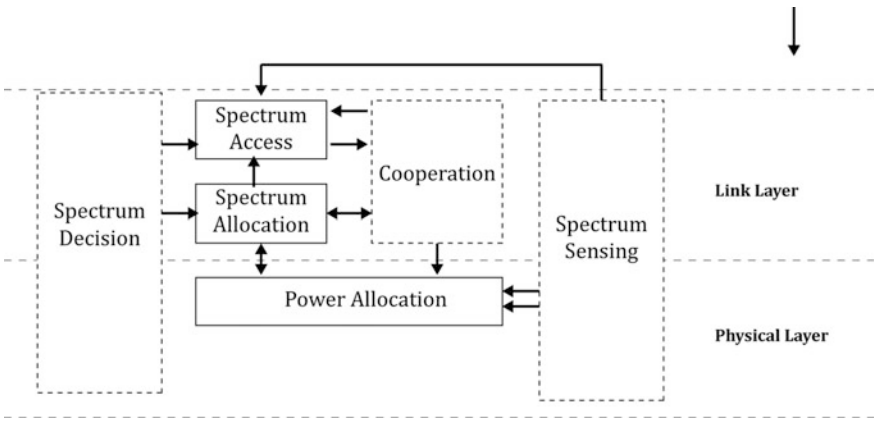

Fig. 4 Spectrum sharing structure for cognitive radio network

- Resource allocation: Selection of proper channels (channel allocation) and respective transmission power adjustment (power control), in order to meet QoS requirements and resource availability, are performed by CR users, supported by QoS monitoring results. Especially in power control, sensing and monitoring results need to be considered in order to address interference constraints;
- Spectrum access: Spectrum resources (channels) are shared by multiple CR users, a specific algorithm should define the time and user that may access the channels. The most difficult task is synchronization because the typical method relies on random access schemes.

Following spectrum decision, resource allocation must take place. Available channels will be assigned to CR users, and transmission power determined to prevent interference on primary networks. After that, a spectrum management technique must be adopted for enabling CR users to control the channels access, avoiding more than one CR to transmit at the same time and channel. Spectrum sharing processes include resource allocation and spectrum access techniques, which are detailed next.

a. Resource allocation
   Local observations provide CR users with information on specific portions of the spectrum band, which will support their decision on the intelligent use of communication resources. In general, game theory addresses resource allocation (wireless channels, bandwidth and transmission power) in CR. Though multiple CR users have a common interest in making the most of spectrum resources, they also locally compete for them. Such competitive environment may result in degradations in the spectrum usage. In addition, CR users must be able to anticipate players' responses in order to get rational decisions. To obtain a fair allocation of the spectrum, a cooperative game theory model is applied in this scenario, enabling CR users to coordinate rational and intelligent solutions. Spectrum sharing game models are detailed next [21].

   - Normal form game: The simplest and most basic model of game theory enabling all players to share common knowledge, with each player being able to make a single decision. The output is the result of combining all other player's decisions;
   - Repeated game: A sequence of stages in which each stage is a normal form game. The actions of each stage are based on the knowledge of game-past actions, current observations, and future expectations;
   - Asynchronous myopic repeated game: The most recent stage of the game is observed and serves as the only input of the player's strategy update. Because they are unable to consider future outcomes, players employ simpler myopic strategies in order to determine current actions, in contrast to complex multi-stage strategies, usually used in general repeated games;
   - Mixed strategy game: Players can choose mixed strategies, assigning probabilities to a set of pure strategies (probability distribution), achieving the Nash equilibrium.

i. Channel allocation
CR users may apply either the FDMA method enabling the division of a frequency band allocated for wireless communication into multiple channels or the OFDM method to modulate multiple signals at different frequencies, in order to determine channels or sub-carriers according to specific QoS requirements.

ii. Power allocation
Co-channel interference is addressed by CR users by adjusting the transmission power accordingly, meaning that such adjustment should be based on PU's interference constraints. Spectrum sharing performance is also enhanced using cooperative neighbor sensing, especially increasing power efficiency, and detecting any PU activity in the transmission range.

b. Spectrum access—CR MAC
Cognitive Radio MAC (CR MAC) protocols are designed to provide efficient channel sensing and control. Because of the absence of a central network entity in CR, users must be able to determine and control sensing schedules. CR users can decide on an on-demand sensing schedule or using aperiodic sensing, as opposed to a periodic sensing, triggered by spectrum sharing operations such as opportunistic transmission and spectrum availability. A spectrum sensing control method, which provides the settings of sensing and transmission intervals, results in higher spectrum access performance.
Studies affirm that MAC protocols can be classified into three categories: random access, time slotted, and hybrid protocols, which are a combination of the two approaches. All three are detailed next:

i. Random access—CR MAC protocols
The random access approach does not require time synchronization, and is generally based on the CSMA/CA scheme.

ii. Time slotted MAC protocols
The time-slotted approach requires network-wide synchronization, enabling time to be divided into slots for both control and data channels. CR MAC protocols also define slotted beaconing periods for CR users. The protocol uses rendezvous channels (RCh) to obtain control information and also backup channels (BC) to provide alternative spectrum bands in case a PU is detected. Communication rendezvous enables CR users to communicate by using a control channel for both control and data transmission. Superframes in the C-MAC protocol are employed for each channel and are composed of the data transfer period (DTP), the beacon period (BP) and the quiet period (QP). Because BPs and QPs of multiple channels are non-overlapping, the connectivity information is immediately updated (when beacons are transmitted) and accurate sensing is carried out during QPs. CR users use the rendezvous channel to obtain inter-channel synchronization, neighborhood discovery, and spectrum management utilization.

iii. Hybrid protocols
These protocols adopt control signaling over synchronized time slots and random channel access schemes for data transmission. Multiple predefined periods (control and data channels) constitute a superframe, which is shared with all network users. Each control and data transmission period employs random channel access.

6 Spectrum Mobility for Cognitive Radio Networks

A typical scenario in cognitive radio networks is that where PU uses its spectrum portion and CR tries to maintain the communication link using other vacant portion. The process of switching bands or channels is called spectrum mobility or spectrum handoff. Some situations when spectrum handoff should be performed are: (1) PU is detected, (2) the CR user loses its connection, or (3) QoS requirements are not achieved [12].

One of the main goals of spectrum mobility is to manage CRN in order to assure RF/front end transitions and minimize any performance degradation during a spectrum handoff.

Next, the main features required for spectrum mobility in the CRN are described:

- Spectrum handoff: The front end of every CR user switches the spectrum band physically and reconfigures parameters (e.g., operating frequency, modulation type).
- Connection management: Available channels should always be managed in order to improve CR performance with a specific QoS requirement.

As defined previously, spectrum mobility events can be detected as a link failure caused by user mobility as well as PU detection. Furthermore, quality degradation of the current transmission also initiates spectrum mobility. When spectrum mobility events are detected through spectrum sensing or neighbor discovery, the spectrum mobility procedures are triggered. Figure 5 illustrates the functional blocks for spectrum mobility in CRNs.

a. Spectrum handoff
Spectrum handoff is organized in two well-defined strategies, they are:

- Reactive spectrum handoff: Spectrum switching decision is performed automatically as a reaction of any link failure.
- Proactive spectrum: Spectrum switching decision is anticipated based on predictions of PU activity.

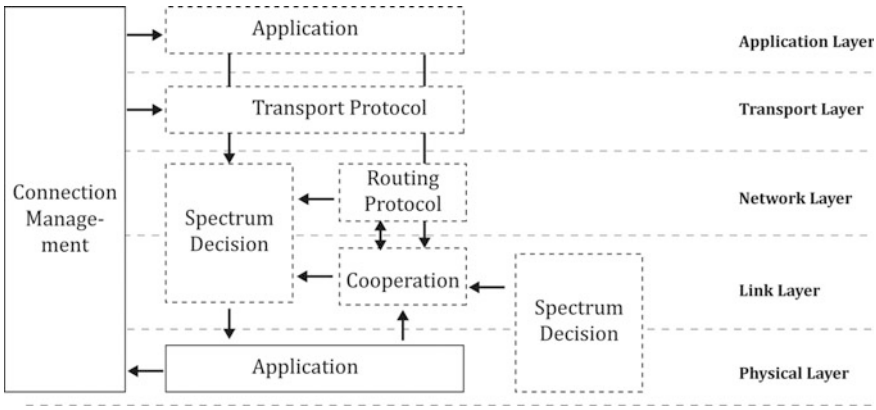

Fig. 5 Spectrum mobility structure for cognitive radio networks [12]

b. Connection management
With the information obtained from PU activity, such as QoS requirements (latency, throughput), CR users can predict specific spectrum handoff optimizing based on protocol stack features and error control schemes, it is done in order to provide intelligence to CR. In some cases, cross layer solutions could take advantage of this function so that application demands and low layer features are coordinated in order to improve QoS [12].

7 Conclusion

The main goal of a cognitive radio network in a white-space scenario is to maximize licensed spectrum usage by secondary subscribers. However, it should be done considering two important conditions: assuring Primary User operation without interference and optimizing secondary user's throughput. To this end, this paper presented a cognitive radio framework that facilitates the understanding of management functionalities common to most cognitive radio network project.

This paper described in detail the four main management functions of CR. Spectrum sensing is used to allocate cognitive radio to an unused portion of the spectrum. Spectrum mobility is employed to vacate specific spectrum bands when PU is detected. Spectrum decision consists of selecting the most appropriate band in accordance with specific QoS requirement. Finally, spectrum sharing consists of coordinating different cognitive radio users in order to take advantage of available bands and prevent collisions in overlapping portions.

References

1. Dahrouj H, Al-naffouri TY, Alouini H. Elsawy MS (2015) Virtualized cognitive network architecture for 5G cellular networks. IEEE Commun Mag 53(7):78–85
2. McHenry M (2003) Spectrum white space measurements. New Am Found Broadband Forum, Meas
3. Maguire GQ, Mitola J (1999) Cognitive radio: making software radios more personal. IEEE Pers Commun 6, 13–18
4. Federal Communications Commission, (2003) Et docket-322
5. Cui S, Sayed AH, Quan Z (2008) Optimal linear cooperation for spectrum sensing in cognitive radio networks. IEEE J Sel Topics Signal Proces 2(1):28–40
6. Tong L, Swami A, Chen Y, Zhao Q (2007) Decentralized cognitive MAC for for opportunistic spectrum access in ad hoc networks a POMDP framework. IEEE J Sel Areas Commun 25(3):589–600
7. Mishra SM, Brodersen R, Cabric D (2004) Implementation issues in spectrum sensing for cognitive radios. In: 38th Asilomar conference signals, systems and computers, Pacific Grove, CA, pp 772–776
8. Kay SM (1998) Fundamentals of statistical signal processing: detection theory. Prentice-Hall, Englewood Cliffs, NJ
9. Tkachenko A, Brodersen RW, Cabric D (2006) Experimental study of spectrum sensing based on energy detection and network cooperation. In: ACM 1st workshop on technology and policy for accessing spectrum (TAPAS)
10. Cochran D, Enserink S (1994) A cyclostationary feature detector. In: 28th Asilomar conference on signals, systems, and computers, Monterrey- CA, pp 806–810
11. Haykin S (2005) Cognitive radio: brain-empowered wireless communications. IEEE J Sel Areas Commun 23:201–220
12. Lee W-Y, Chowdhury KR, Akyildiz IF (2009) CRAHNs: cognitive radio ad hoc networks. Ad Hoc Netw 7:810–836
13. Lee W-Y, Vuran MC, Shantidev M, Akyildiz IF (2006) NeXt generation/dynamic spectrum access/cognitive radio wireless networks: a survey. Comput Netw J 50:2127–2159
14. Ramchandran K, Wild B (2005) Detecting primary receivers for cognitive radio applications. In: IEEE DySPAN, pp 124–130
15. FCC (2003) Notice of inquiry task force report. ET Docket
16. Mishra SM, Brodersen RW, Cabric D (2004) Imlementation issues in spectrum sensing for cognitive radios. In: IEEE conference on signals, systems and computers, Asilomar, pp 772–776
17. Whitt W, Sriram K (1986) Characterizing superposition arrival processes in packet multiplexers for voice and data. IEEE J Sel Areas Commun 4(6):833–846
18. Mousavinia A, Amirpour H, Shamsi N (2013) A channel state prediction for multi-secondary users in a cognitive radio based on neural network. In: 2013 international conference on electronics, computer and computation (ICECCO), Ankara, pp 200–203
19. Yin SX, Hong W, Li SF, Yin L (2011) Spectrum behavior learning in cognitive radio based on artificial neural network. In: 2011-MILCOM military communications conference, Baltimore, MD, pp 25–30
20. Taj MI, Akil M (2011) Cognitive radio spectrum evolution prediction using artificial neural networks based multivariate time series modelling. In: Wireless conference 2011-sustainable wireless technologies (European wireless), 11th European, Vienna, Austria, pp 1–6
21. Neel J (2006) Analysis and design of cognitive radio networks and distributed radio resource management algorithms. PhD Dissertation, Virginia Polytechnic Institute and State University

Part III
Cognitive Technologies Applied to Optical Networks

Optical Amplifier Cognitive Gain Adjustment Methodology for Dynamic and Realistic Networks

Uiara Celine de Moura, Miquel Garrich, Amilcar Careli Cesar, Jacklyn Dias Reis, Juliano Oliveira and Evandro Conforti

Abstract Optical amplifiers are essential devices in optical networks to recover the signals degraded from passive optical components attenuations such as fiber span and optical switches. However, optical amplifiers, usually based on erbium-doped fiber, are also the main noise contributors, reducing the signal quality. Given that noise depends on the amplifiers' operating point, it is desirable to find their best operating point which may lead to the lowest degradation of the optical signal. In this work, we evaluate our proposed cognitive methodology for optical amplifier gain adjustment, relied on case-based reasoning. Realistic scenarios are considering, exploring networks with different number of amplifiers and span lengths per link. The results show an optical signal-to-noise ratio improvement when the cognitive methodology is applied for most cases, demonstrating the methodology robustness for networks with different characteristics in terms of topology and size.

1 Introduction

The current growth of end-users' services and applications, such as mobile Internet, high-resolution videos, cloud-based services, and the Internet of Things increases traffic heterogeneity and high-bandwidth demands. To account for these needs, optical networks are evolving toward a reconfigurable and flexible optical layer, enabling the transmission of different data rates and modulation formats. However, such traffic and network heterogeneity poses additional requirements at the control and management plane [1].

U.C. de Moura (✉) · M. Garrich · J.D. Reis · J. Oliveira
Optical Technologies Division, CPqD Foundation, Campinas, SP, Brazil
e-mail: umoura@cpqd.com.br

A.C. Cesar
Department of Electrical and Computer Engineering, São Carlos School of Engineering, University of São Paulo, São Carlos, SP, Brazil

U.C. de Moura · E. Conforti
Faculty of Electrical and Computer Engineering, Department of Communications, University of Campinas, Campinas, SP, Brazil

A. Paradisi et al. (eds.), *Cognitive Technologies*, Telecommunications and Information Technology, DOI 10.1007/978-3-319-53753-5_9

The evolution from traditional quasi-static wavelength division multiplexed (WDM) networks towards flexible and dynamic optical networks contains contributions from two sides [2]. On the transponder side, enhanced configurations include: a dynamic rerouting demonstration with bit-rate or modulation format adaptation aiming at minimize the spectrum utilization [3]; a method for optical link survivability by acting on the transmitter launch power and bit-rate, and on the receiver digital signal process for linear/nonlinear impairments compensation, based on the status of the optical signal-to-noise ratio (OSNR) and the bit error rate (BER) [4]; an optical spectral shaping optimization based on genetic algorithm for fiber nonlinearities mitigation in high baud-rate transmission systems [5] and in unrepeated links [6]; and a flexible transmitter/receiver architecture that adapts its modulation formats and symbol rate according to the BER information [7]. On the network side, wavelength selective switches (WSSs) and optical amplifiers are the key equipments because they provide routing and amplification directly in the optical domain, respectively. Recent proposals include: WSSs configuration using global equalization strategies to improve network performance [8]; power budget strategies that combine the control of amplifiers and WSSs jointly with routing and wavelength assignment (RWA) obtaining OSNR improvements in meshed network scenarios [9]; a dynamic gain equalization [10] and a local adaptive gain control technique [11–13], both aiming at end-to-end performance improvements. All these strategies apply adaptive schemes to maintain performance and service continuity under dynamic scenarios.

The concept of cognitive networks has been recently proposed to address the increasing variety of technologies and proposals that enable flexible networking [14]. A cognitive network, well known in radio and wireless technologies [15], perceives current conditions and plans, decides, acts, and learns from these adaptations to use them in future decisions, considering end-to-end goals [16]. In [17], the authors introduce and discuss the technologies and techniques that will enable a cognitive optical network to observe, act, learn, and optimize its performance and [18] presents the architecture concepts and proposals for future cognitive networks. In addition, [19] presents a control plane structure to coordinate the cognitive optical network elements and [20, 21] present a Fuzzy controller applied to cognitive optical networks that defines new routes based on new connections demand considering physical layer penalties. Further initiatives include cognitive applications to reduce the connection blocking probability by improving the performance of the light-path calculation algorithms [22]; to introduce a cognitive control and management system with an architecture on demand scheme to minimize complexity and to better handle environmental unpredictability [23]; to build a quality of transmission estimator for classifying light-paths [24–29]; to dynamically adjust the modulation formats to satisfy quality of transmission requirements improving failure restoration time [30]; and to reconfigure/design virtual topologies [31–33]. Finally, [34, 35] review the cognitive applications developed so far in optical networks. Therefore, cognitive approaches and techniques applied to optical network are viable candidates to manage complexity and to permit efficient utilization of available resources [15].

In this context, we present our global cognitive methodology [36] that adjusts the operating points of the optical amplifiers along a light-path in a dynamic

optical network aiming to optimize the connections' performance along the time. The cognition relies on case-based reasoning (CBR) to learn from previous lightpath establishment. Also in [36], we demonstrate the methodology performance in a five-node meshed network testbed, showing its learning capability in terms of optical OSNR improvements along the time and its suitability for diverse amplifier types. Additionally, in [1], we extend the analysis to different and real network topologies, exploring different characteristics in terms of graph density, but considering fixed 100-km fiber span links with two amplifiers each. In this work, we perform additional analysis, such as on the network size and on the amplifiers' operating points, considering three real networks in realistic scenarios, ranging span lengths and number of amplifiers between nodes. The results shown an OSNR improvement when the cognitive methodology was applied for most cases when comparing to other methodologies, demonstrating that the proposed methodology can be applied for networks with different characteristics.

2 Optical Amplifiers

In this section, we review some fundamental concepts of optical amplifiers and report a set of experimental characterization results to support these fundamental concepts. This will provide the background to elaborate advanced gain control schemes capable to exploit relevant amplifier characteristics while accounting on their implications on signal quality in end-to-end systems.

Optical amplifiers are key elements in optical transmission systems and have contributed to the success of optical data transport together with low loss transmission fibers, compact laser diodes, and high speed photodiodes [37]. They are responsible for compensate attenuations due to passive devices and components in optical networks. Transparent to data rate and modulation format, optical amplifiers made possible WDM transmission and increased the repeater spacing. However, the fundamental process of spontaneous emission generates noise, that degrades the signal-to-noise ratio (SNR). The figure of merit related to this SNR degradation is the amplifier noise figure (NF) and it is defined as [38]

$$NF = \frac{SNR_{in}}{SNR_{out}} \tag{1}$$

where the SNR is referred to the electric power generated when the optical signal is converted into an electric current [38]. A simple expression for NF can be obtained by considering an ideal detector whose performance is limited by shot noise only [38]

$$NF = \frac{2n_{sp}(G-1)}{G} \tag{2}$$

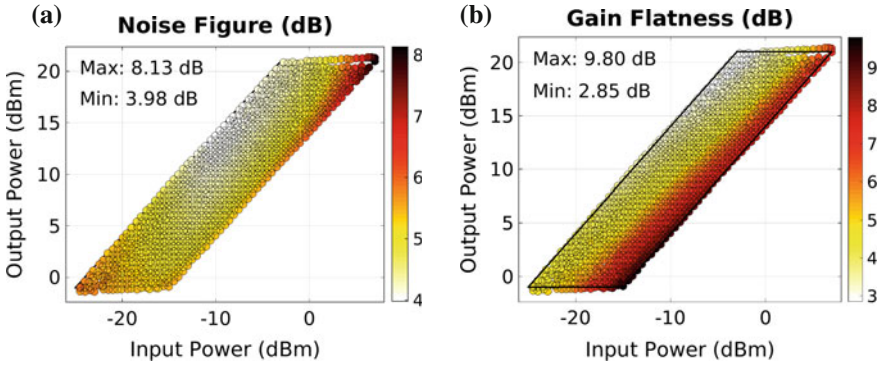

Fig. 1 **a** NF and **b** GF dependence with the optical amplifier operating point inside the power mask obtained experimentally via characterization process [40]

where n_{sp} is the spontaneous emission (or population-inversion) parameter and G is the amplifier gain [38]. The NF can also be expressed in terms of the noise power at the amplifier output (P_{ASE}) in a bandwidth $\Delta\nu$ [39]

$$NF = \frac{P_{ASE}}{h\nu\Delta\nu G} + \frac{1}{G} \tag{3}$$

where h is the Planck's constant and ν is the channel frequency.

Figure 1a shows the NF values obtained experimentally using (3) in an experimental characterization process [40] for an erbium-doped fiber amplifier (EDFA) designed to work with a minimum total input power of −25 dBm, a maximum total output power of +21 dBm, and gain varying from 14 to 24 dB. These values define the amplifier operating region, referred as power mask [41]. This experimental characterization was performed using 40 flat and non-modulated C-band channels and is detailed in [40].

Other characteristic of the optical amplifiers is that they do not provide the same gain for all channels. Thus, signals with different frequencies on the spectrum experience different gains when passing through an optical amplifier. Figure 1b shows the experimental characterization of the gain flatness (GF) calculated as the difference between the maximum and minimum channel gains, in dB, for the same amplifier in Fig. 1a. The uneven amplification along the optical spectrum characterized by the GF can accumulate in a cascaded setup of optical amplifiers. To overcome this impairment, gain flattening filters (GFFs) can apply a static attenuation to different frequencies reducing the gain disparity at a nominal amplifier gain.

Figure 2a shows the OSNR at the amplifier output, also evaluated on the experimental characterization process, considering an input signal without noise. Different from the NF, the OSNR can not be used to estimate the amplifier performance because it depends on the input noise.

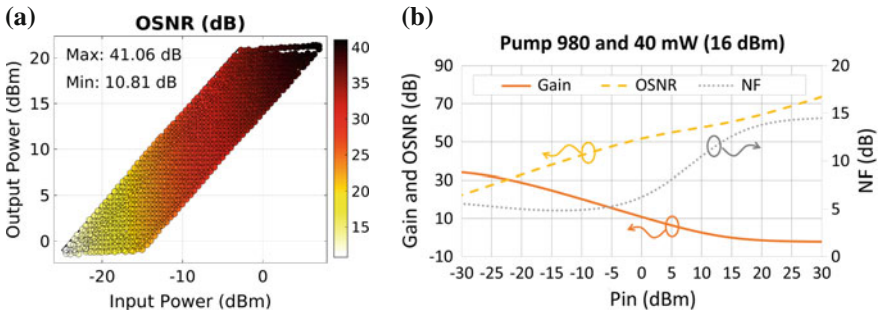

Fig. 2 **a** Experimental ONSR obtained via characterization [40] considering an input power without noise and **b** simulated gain, ONSR and NF for a single channel at 1530 nm in an optical amplifier with 14 m of EDF and 40 mW (16 dBm) of co-propagating pump power at 980 nm

Note that in Fig. 1a NF presents a high degradation for high input powers, while OSNR in Fig. 2a presents the best (higher) values in this same region. It is important to recall that NF is defined in terms of the electrical SNR, not the optical SNR (OSNR). Moreover, according to [39], as the signal level increases (at the input), the inversion carrier population is depleted, thus both the inversion parameter (n_{sp}) and the NF (which is directed related to n_{sp} in (2)) will increase. In addition, Fig. 2b helps to validate the experimental results, presenting simulation results considering a single channel (1530 nm) and a 14 m EDF pumped (co-propagating) with 40 mW (16 dBm) at 980 nm. Is this simulation, the channel input power was extrapolated to 30 dBm to see the behavior of gain, NF and OSNR at such a high input power. The same behavior obtained experimentally is observed in Fig. 2b, which is the NF increase (degradation) and the OSNR improvement with the input power increase. We believe that the inversion depletion caused by the high input power reduces the spontaneous emission (noise) and these two factors (high input power and low noise) are sufficient to improve the output OSNR.

Conventionally, the amplifiers are classified into three categories, according to their position in a straight line scenario. The first amplifier, placed right after the transmitter, is called booster (B) amplifier. It is used to rise the launch power on the optical fiber and its working region is characterized by high input and output power levels. The inner amplifiers along the optical fiber are called line (L) amplifiers. They are used to compensate previous and forward fiber losses and are, usually, composed of two-stage EDFAs forming a high-gain amplifier. The last amplifier, placed right before the receiver, is called preamplifier (P) and it is used to improve the signal for reception and its working region is characterized by low input and output power levels. We will adopt this same amplifier nomenclature in our networks, even though the signal is not necessary generated and received in a single link at a meshed optical network.

3 Advanced Control Techniques for Optical Amplifiers

Nowadays, the optical amplifiers work in a fixed gain (FG) condition, in which their gains are set to compensate passive device attenuations inherent in fiber spans, multiplexers, dispersion compensated fibers, and wavelength selective switches. Observing NF (Fig. 1a), GF (Fig. 1b) and OSNR (Fig. 2a) dependence on the amplifiers' operating point, it is important to search the amplifier best operating point which may lead to the lowest degradation for the optical signal [1]. Considering light-paths composed of several amplifiers, this search would be unaffordable, since the number of gain combinations to evaluate grows exponentially with the number of amplifiers. Thus, local adaptive heuristics aiming the amplifier control in this scenario have been proposed and applied in straight line scenarios [11–13]. Although these techniques do not guarantee a global optimal result, as they try to find the best amplifier operating point, they end up improving end-to-end performance [1].

In this section, we will describe two gain control heuristics for optical amplifiers. First, we will review a local heuristic named adaptive gain control (AdGC) [11] that relies on the characterization of the amplifier to perform stand-alone search for its best operating point in terms of amplifier gain. Second, we will describe a global cognitive methodology [1, 36] that exploits a database with network history to improve amplified gain configurations. Both schemes will be compared with the FG condition, where the gains remain constant during all the time. It is important to point out that all these amplifier control techniques try to maintain the amplifiers operating points inside their power masks to avoid unknown performance in terms of NF and GF for operating points outside the power mask.

3.1 Adaptive Gain Control

The adaptive gain control (AdGC) is a heuristic described in [11] that adjusts the amplifier operating point automatically, in terms of its set point gain, aiming to provide the best trade-off between its NF and GF (OSNR is not consider because its dependence on the noise power at the amplifier input). By not considering any overall performance to adjust the amplifiers, the AdGC is essentially a local approach, although it attempts to achieve a better end-to-end performance in terms of OSNR/BER even adjusting each amplifier based on its individual performance.

Figure 3a depicts a high-level AdGC flowchart, in which power mask information (PM Info) is a static database and refers to the experimental characterization process outcome [40]. The AdGC process is composed of three steps: The "Pin Measurement" step monitors the amplifier total input power (Pin) and, when there is a change on its value, the "Gain Search" step queries PM Info for operating points with the same current Pin. These points are plotted in an objective space, illustrated in Fig. 3b, with NF and GF as the axis (scaled from zero to one). Each point in the objective space refers to a gain value depicted on the right side color bar. Finally, the "Apply

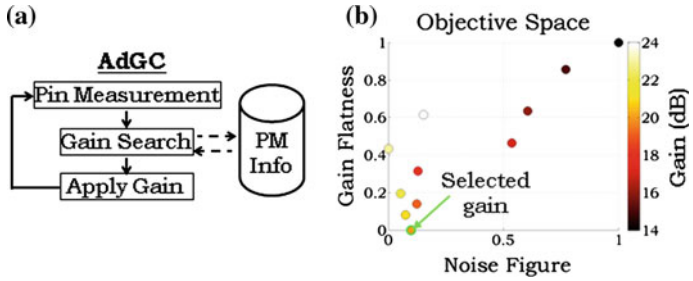

Fig. 3 **a** AdGC flowchart and **b** objective space highlighting the selected gain applied to the amplifier [1]

Gain" step selects a gain (indicated in Fig. 3b with the minimum Euclidean distance from the origin), and applies it to the amplifier.

The AdGC impact over a cascaded of amplifiers was evaluated in terms of system GF and NF, and received OSNR and BER [11], with additional adjustments considering weights applied to amplifiers' NF and GF parameters to guarantee signal performance maintenance in terms of BER measurements. In [42], AdGC was applied in dynamic and meshed optical networks, demonstrating a blocking probability reduction when performance restrictions were considered. Additionally, a demonstration of the AdGC methodology as a primitive cognitive approach, considering the launch power impact on BER measurements, was presented in [13], maintaining suitable BER values for up to 6 dB of attenuation penalties in an experimental testbed with different modulation formats and bit-rates.

3.2 Amplifier Cognitive CBR

The amplifier cognitive CBR (AcCBR) methodology [1, 36] is a global heuristic that uses case-based reasoning (CBR) to optimize the connections' OSNR. It applies cognition for amplifier set point gain adjustments in dynamic and meshed optical networks. CBR is a combination of reasoning and learning, exploring prior experience to solve future problems [43]. In this context, prior experience comes from previous connections condition and performance information dynamically stored in a database (DB).

AcCBR flowchart is depicted in Fig. 4 and it is applied for each new connection request. For a meshed network, AcCBR assumes that the connections between two nodes are performed through light-paths (LP) composed of links (set of amplifiers and fiber spans between two nodes). Moreover, AcCBR considers a fixed channel power at the input of all links. This fixed channel power is achieved by channel attenuation capability at the nodes and its importance is explained further up. Before establish the LP, but considering that it is already established in terms of channel load and total power increase at each link, AcCBR comprises the CBR process, which is

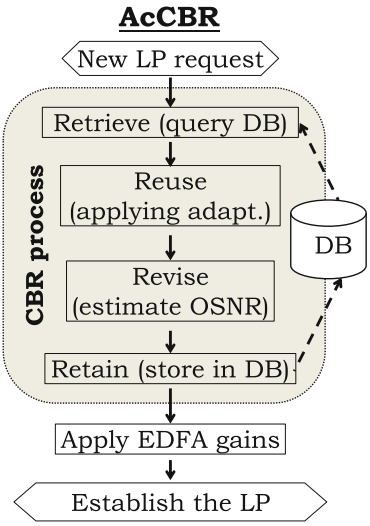

Fig. 4 AcCBR flowchart [1]

divided into four steps, highlighted in Fig. 4 and following detailed, together with the AcCBR methodology itself.

1. *Retrieve*: this step queries the DB for similar previous connections in terms of the following LP features:

- number of links (or nodes);
- total input powers for each link, within a margin of $\pm\mu^{Pin}$ dB;
- total fiber losses for each link, within a margin of $\pm\mu^{FO_{Loss}}$ dB;
- number of amplifiers for each link.

2. *Reuse*: this step is responsible to propose a new gain combination (as a vector of gains, G_{new}) for the amplifiers along the LP and depends on the following *retrieve* outcomes:

Retrieve outcome 1: for no similar LPs in DB (or when DB is empty because it is the first connection), the *reuse* step considers the current amplifiers' gains along the LP as G_{new}.

Retrieve outcome 2: for one similar LP in the DB, the *reuse* step defines G_{new} by randomly changes in ± 1 dB a certain percentage ($\kappa\%$) of the amplifiers in this similar LP to explore future improvements.

Retrieve outcome 3: for two similar LPs in the DB, the *reuse* defines G_{new} according to

$$G_{new} = G_H + \frac{G_H - G_L}{\mid G_H - G_L \mid}, \tag{4}$$

where G_H and G_L are amplifiers' gain vectors of the LP with the higher and lower OSNRs, respectively. By doing so, G_{new} explores the direction of OSNR improvement provided by these two similar LP cases in the DB.

Retrieve outcome 4: for three or more similar LPs in the DB, *reuse* step applies (4), and considers one of the following alternatives to define G_{new}:

- *A*lter the gains of $\kappa\%$ (the same κ defined on the *Retrieve outcome 2*) amplifiers not modified until now in the set of similar LPs by ± 1 dB with probability α;
- *M*odify the gains of $\kappa\%$ amplifiers that have different gain values in the set of similar LPs with probability μ;
- *U*se the outcome of (4) without any modification with probability υ.

Note that these alternatives attempt to address the classical well-known exploration and exploitation trade-off in evolutionary algorithms [44] and the condition $\alpha + \mu + \upsilon = 1$ must hold.

3. *Revise*: this step estimates the OSNR at the end of the LP considering the *reuse* outcome G_{new}. This estimation considers the component models described in Sect. 5 (NF dependence on amplifier's operating point, but not on the channel frequency; and gain dependence on channel, in order to simulate the accumulated tilt effect along a cascade of amplifiers) and the OSNR calculation described in [1] and replied here

$$OSNR^{CH} = \frac{G^{CH,path} P_{in,link}^{CH,path}}{(G^{CH,path} NF^{CH,path} - 1) h \nu^{CH} \Delta\nu^{CH}} \tag{5}$$

where $G^{CH,path}$ and $NF^{CH,path}$ are the channel gain and NF along the LP, $P_{in,link}^{CH,path}$ is the channel input power at the LP first link, h is the Planck's constant, ν^{CH} is the channel frequency and $\Delta\nu^{CH}$ is the optical channel band in which signal and noise were measured.

4. *Retain*: as the final step in the CBR process, *retain* stores in DB the new LP information in terms of number of links, total input powers and total fiber span losses for each link, G_{new} and OSNR estimation, disregarding the latter value, to serve as input for future decisions. If it is the first connection, DB is created during the *retain* step.

Finally, AcCBR adjusts the amplifiers' gains along the LP according to the best case in DB after the *retain* step in terms of OSNR (which might not be the one just stored, associated to G_{new}) and establishes the new LP [1].

The restriction of a fixed input channel power in each link is important to maintain a null total link gain for the channels, preventing that the amplifier gain adjustments by the methodologies (also AdGC) impact another links not involved on the current LP.

AcCBR is restricted to transparent optical networks and should be applied together with the RWA. Thus, every time a new LP is established, causing changes in the amplifiers total input power, AcCBR adjusts the amplifiers' set point gain based on global performance. Moreover, changes in the amplifiers input power, caused by

different channel loads along the time, leads to different cases to be stored in DB, diversifying its content and improving AcCBR experience to solve new problems [1].

On the other hand, AcCBR is not restrict to one amplifier technology, and may be applied to any amplifier, such as Raman or hybrid amplifiers, since it has an automatic gain control (automatic pump power adjustments to achieve the configured gain) and has been characterized in terms of NF and GF under its power mask [1].

4 Network Topologies

In our previous work, we performed experiments considering a five-node network available at CPqD laboratory, in which we demonstrated the cognition process by showing OSNR improvements over time [36]. Additionally, AcCBR benefits were also explored for different, larger, and real network topologies [1]. However, all these demonstrations consider links with a fixed 100 km length span and two amplifiers.

In this work, we consider three real networks from [45] with different features and sizes (in terms of distance), as shown in Fig. 5. Biz Networks (Fig. 5a), from Indonesia (already considered in [1]); Tata (Fig. 5c), from India; and China Telecom (Fig. 5e), from China. For these networks, we assume the real distances between nodes, calculated using latitude and longitude information also presented in Fig. 5 for each network graph.

To define the number of amplifiers per link, we consider its total loss, which depends on the fiber optical loss in dB/km. In our simulations, we consider standard single mode fiber (SSMF) with 0.2 dB/km. The number of amplifiers per link follows the rule: for links with fiber losses between 1 and 11.5 dB, we consider one amplifier placed before the optical fiber. This single amplifier must have a gain variation from 17 to 27 dB, to also compensate the node loss experimented by the signal when passing from one link to the following. For links with fiber losses between 11.5 and 32 dB, we consider two amplifiers, with gains varying from 14 to 24 dB each. For losses above 32 dB, we consider the addition of one amplifier for each fiber loss interval of 27 dB. The inner amplifiers must also have a gain variation from 17 to 27 dB. Total link loss (left y axis) and number of amplifiers per link (right y axis) are also presented in Fig. 5 for the three networks.

We also avoid span losses higher than 20 dB for total link losses higher than 200 dB (or 1000 km). In other words, if after applying the previous rule, there are still span lengths with losses higher than 20 dB for a link with more than 200 dB of total loss, we proceed adding line amplifiers to this link until it presents spans losses lower than 20 dB. This is done to minimize performance degradation due to low signal powers at the amplifiers input.

As in [1], we assume bidirectional links (directed graphs). The density of a directed graph $G(V, E)$, where V is the set of vertices (nodes) and E is the set of edges (links), is defined as the current number of edges divided by the total possible number of edges: $D = \mid E \mid / (\mid V \mid (\mid V \mid -1))$, $D \in (0, 1]$ [46]. Density indicates the

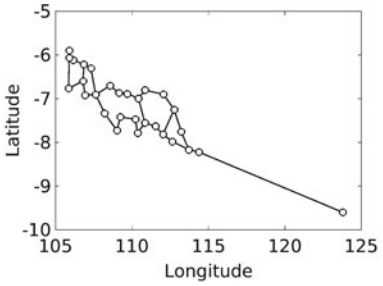

(a) Biz Networks graph

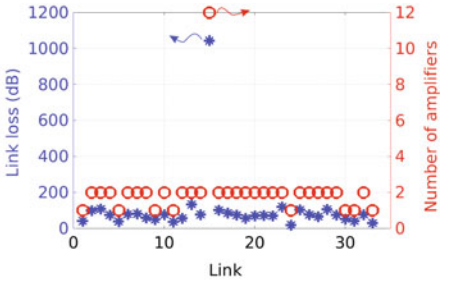

(b) Biz Networks: link distances and number of amplifiers

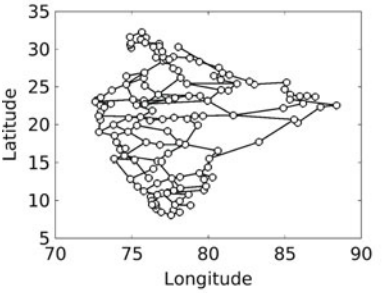

(c) Tata network graph

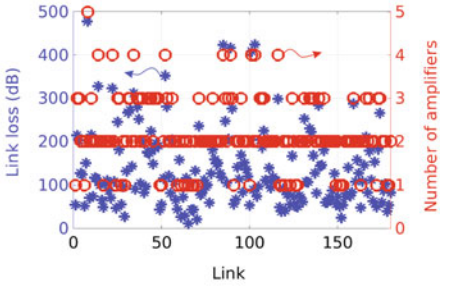

(d) Tata network: link distances and number of amplifiers

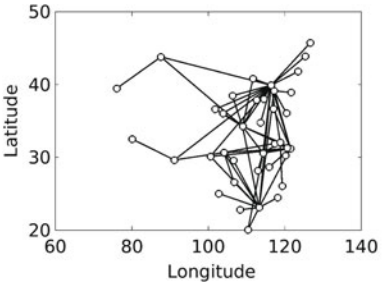

(e) China Telecom network graph

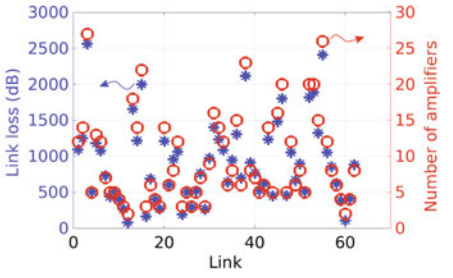

(f) China Telecom network: link distances and number of amplifiers

Fig. 5 Real networks: Biz Networks, small size network, from Indonesia, **a** graph and **b** distances and number of amplifiers per link; Tata, midsize network, from India, **c** graph and **d** distances and number of amplifiers per link; China Telecom, big size network, from China, **e** graph and **f** distances and number of amplifiers per link

graph connectivity, measuring how close a graph is to its corresponding complete graph [1].

Table 1 summarizes the networks' parameters in terms of number of links and nodes, density, distance, link losses, and number of amplifiers per link (amp/link), considering minimum, maximum, mean and standard deviation values. Biz Networks is the smallest network, with distances from 18.63 to 133.95 km, and just

Table 1 Networks' parameters

	Biz networks	Tata	China telecom
Links	66	360	124
Nodes	29	143	38
Density	0.0813	0.0177	0.0882
Min. distance (km)	18.63	12.03	80.45
Max. distance (km)	1,044.47	477.94	2,564.26
Mean distance (km)	102.29 ± 171.16	133.85 ± 87.64	911.97 ± 567.47
Min. loss (dB)	3.73	2.41	16.09
Max. loss (dB)	208.89	95.59	512.85
Mean loss (dB)	20.46 ± 34.23	26.77 ± 17.53	182.39 ± 113.49
Min. amp/link	1	1	2
Max. amp/link	12	5	27
Mean amp/link	2.06 ± 1.82	2.16 ± 0.78	9.61 ± 6.25

one link with 1,044.47 km, which increases mean and standard deviation distances to 102.29 ± 171.16 km (Not considering this link, mean and standard deviation reduce to 72.85 ± 26.23 km). It presents a ring topology, with 29 nodes and 66 links, which leads to a density of 0.0813. Tata is a midsize network with a more uniform distance distribution, with a mean of 133.85 ± 87.63 km (from 12.03 to 477.94 km). It presents the highest number of links and nodes, 360 and 143, respectively, forming interconnected rings. Although, due to the high number of nodes, it presents the lowest density (0.0177). Finally, China Telecom is a big size network, with link distances from 80.45 to 2,564.26 km. It presents a low number of nodes (38) considering its area, with 124 links, resulting in a density of 0.0882, forming a hub topology. Due to this characteristic, China Telecom presents the smallest number of links per LP, as will be seen.

5 Computer Simulation Models and Assumptions

The component models considered on the computer simulations are the same adopted in [1], i.e., for optical amplifiers, we consider NF dependence on operating point, but not on the channel frequency. On the other hand, we consider the channel gain information. As discussed in [1], there is a NF interval higher than 1 dB along the C-band channels, which would cause problems on the ONSR estimations. However, experimental OSNR measurements also presented in [1] are consistent with the estimated values obtained not considering NF per channel. For the optical fiber, we consider the same attenuation for all C-band channels. Again, we do not investigate nonlinear effects, since we consider that channel optical power does not exceed 0 dBm at the optical fiber input. Finally, the nodes are WSSs that act to route the channels and attenuate them to guarantee the channel power target at the input of the first amplifier on the link.

Channel OSNR at the end of the LP is estimated using (5), the same equation used on the *revise* step on AcCBR methodology. The component's models and OSNR calculation are important not only for the simulations, but also when applying AcCBR experimentally, since the cognitive methodology estimates the OSNR on the *revise* step, before applying the proposed new gains.

We also consider four different amplifiers models, described as follows:

- Model 1: it is an EDFA amplifier with a 14 m EDF stage, co-propagating pump power up to 600 mW at 980 nm, and no GFF. Its minimum total (considering all channels) input power is −25 dBm, maximum total output power is +21 dBm, and the gain varies from 14 to 24 dB. Its NF and GF dependence on operating point is presented in Fig. 1a and b, respectively;
- Model 2: it is an EDFA amplifier with one stage of EDF and up to 300 mW and 980 nm co-propagating pump. Its minimum total input power is −30 dBm, maximum total output power is +14 dBm, and the gain varies from 14 to 24 dB. Its NF and GF dependence on operating point is presented in Fig. 6a and b, respectively. Its internal optical circuit is unknown in terms of EDF length and GFF presence. Although, low GF values around the 19 dB gain-diagonal indicate the GFF presence (see Fig. 6b);
- Model 3: it is also an EDFA amplifier with one stage of EDF but with up to 600 mW and 980 nm co-propagating pump. Its minimum total input power is −25 dBm, maximum total output power is +21 dBm, and the gain varies from 14 to 24 dB. Its NF and GF dependence on operating point is presented in Fig. 6c and d. Its internal optical circuit is also unknown in terms of EDF length and GFF presence. Again, it is possible to infer the GFF presence by the low GF values around the 19 dB gain-diagonal;
- Model 4: it is an EDFA amplifier with two stages of EDFs (7 m each) and a GFF between them. Both stages with one co-propagating 980 nm pump with up to 300 and 600 mW for first and second stage, respectively. Its minimum total input power is −28 dBm, maximum total output power is +24 dBm, and the gain varies from 17 to 27 dB. Its NF and GF dependence on operating point is presented in Fig. 6e and f, respectively.

For all the amplifiers, the pump power varies according to the amplifier operating point.

Table 2 (second column) presents the amplifier classification adopted in this work according to the number of amplifier in a link (first column) in terms of B (booster), L (line) and P (pre) amplifiers. We will evaluate two cases in terms of amplifier models, both considering model 4 for the line amplifier. The first case (column three) considers model 1 for both pre and booster, while case 2 (column four) considers model 3 for booster and model 2 for preamplifier.

The simulation accomplished for all networks was developed in MATLAB® and consists in generating a traffic with 1,000 connections and 500 erlang (load) based on a Poisson process in an ad hoc dynamic demand and solving a traditional RWA problem. We made the same assumptions as in [1], considering a classical optical

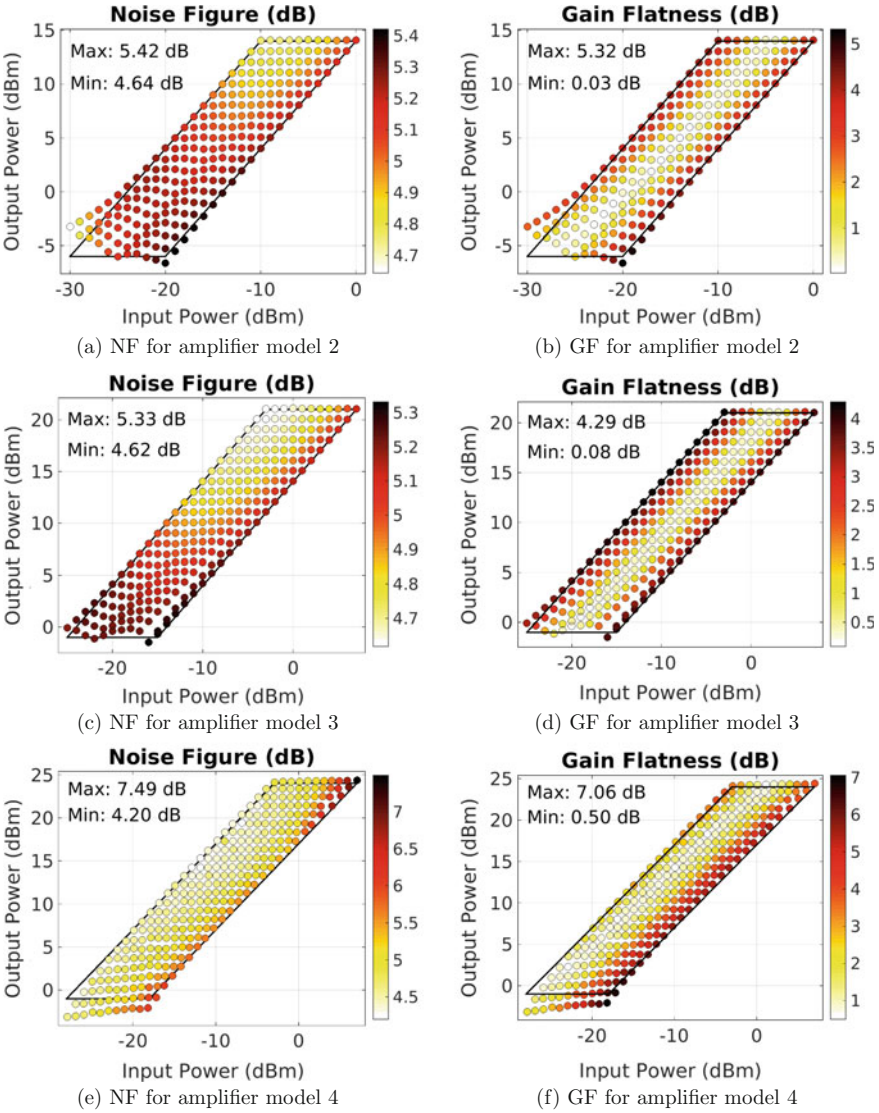

(a) NF for amplifier model 2
(b) GF for amplifier model 2
(c) NF for amplifier model 3
(d) GF for amplifier model 3
(e) NF for amplifier model 4
(f) GF for amplifier model 4

Fig. 6 NF and GF dependence with the amplifier operating point for amplifier models 2, 3, and 4 obtained experimentally using the characterization process described in [40]

circuit-switched and transparent network, with wavelength continuity constraint, i.e., the LP must have the same wavelength available in all links; a non-grooming scenario, in which the signals do not share the same channel even if there is available band; the availability of 40 C-band channels free of noise and spaced of 100 GHz to establish the connections; Dijkstra algorithm [47] to find the LP with the lowest

Table 2 Amplifiers model and classification per link

Number of amplifiers	Amplifier classification	Case 1	Case 2
1	L	L4	L4
2	B-P	B1-P1	B3-P2
≥3	B-L-P	B1-L4-P1	B3-L4-P2

loss; and *first-fit* to wavelength assignment in unidirectional connections (Simplex). The WSS attempts to achieve a channel power of −25 dBm at the links input during all the simulation.

These simulations were repeated 10 times for each network, for each amplifier gain control conditions (FG, AdGC and AcCBR), and for each case described on Table 2. We also consider four different initials DB sizes, starting from zero and sequentially increasing. The OSNRs of all the connections presented in the network were estimated each time a connection was established, which corresponds to the moment in which the methodologies (AcCBR or AdGC) were applied. Thus, it was possible to consider the impact of the methodologies also on the connections already established on the network.

For all the amplifier gain controls (FG, AdGC, and AcCBR), the simulations start with the amplifiers gains adjusted to compensate fiber span and WSSs losses, corresponding to the FG condition.

Regarding the AcCBR methodology, since previous works [1, 36] consider links with a fixed 100 km, good performance was achieved considering a margin $\pm\mu^{FO_{Loss}}$ of ±1 dB. Now that we are considering links with different span lengths, this margin was changed to ±2 dB. Moreover, previous works alter just one amplifier along the LP. In this work, as we have higher number of amplifiers in a single LP, it would take too long to diversify the LPs on DB. Thus, we decide to set κ (defined on the *reuse* step in Sect. 3) as 50.

6 Results and Discussions

Figures 7, 8, 9, 10, 11, 12, 13, 14, 15, 16, 17 and 18 summarize all the results. Figures 7, 9, 11, 13, 15 and 17 present estimated mean and standard deviation OSNR considering all the connections established in the network during 10 repetitions of a RWA simulation (1000 connections and 500 erl) considering the three amplifier gain control conditions (FG, AdGC, and AcCBR). In these figures, AcCBR OSNRs (mean and standard deviation) are plotted as a function of the DB size, while FG and AdGC OSNRs (continuous and dashed lines for mean and standard deviation, respectively) are plotted as a straight line, just to serve as a reference for the AcCBR results.

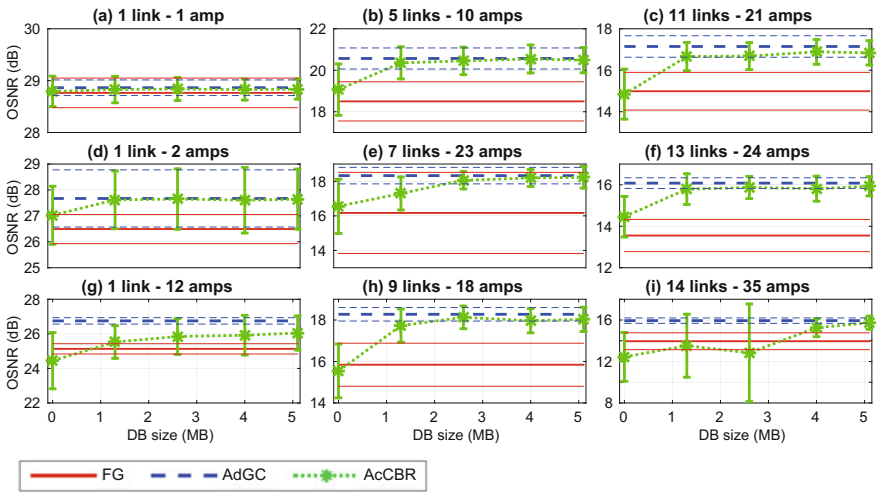

Fig. 7 Biz Networks simulation results with amplifiers B1-L4-P1 (case 1). Mean and standard deviation OSNR at the end of the LP per DB size for 10 repetitions of a RWA with 1000 connections and 500 erlang

Moreover, OSNR values vary from LP to LP, depending on its characteristic in terms of number of links and amplifiers, presenting values from around 29 dB for links with 1 amplifier and 1 link (see Fig. 7a), to 15 dB, for LPs with 14 links and 24 amplifiers (see Fig. 7i). Thus, we divided the results into LPs' number of links and amplifiers to better visualize the OSNR values, selecting nine LPs for each network.

Figures 8, 10, 12, 14, 16 and 18, present the amplifiers' operating points evolution with time inside the power mask for each amplifier gain control conditions: first column stands for FG, second column for AdGC, and the last column for AcCBR. These operating points were obtained each time a connection was established and for all the amplifiers along the LP. The time, corresponding to a single simulation (one of the ten repetitions), is mapped into the dot colors and their values are indicated on the right side color bar. White dots in AcCBR gain control are the operating points evaluated by the cognitive methodology, but not applied on the network by presenting worst performance in terms of OSNR. For AcCBR, amplifier operating points were obtained just for the highest DB size simulation. Also, in these figures, the first row (a–c) corresponds to line amplifiers in links with one amplifier; second row (d–f), to booster amplifiers in links with two or more amplifiers; third row (g–i), to line amplifiers in links with three or more amplifiers; and fourth row (j–l) to preamplifiers in links with two or more amplifiers. China Telecom does not present links with one amplifier (see Table 1). That is why Figs. 16 and 18 just present three rows (a–i), starting from booster amplifier model in links with two or more amplifiers.

It is important to mention that a single LP has several operating points in Figs. 8, 10, 12, 14, 16 and 18. As an example, imagine a LP with three links: the first one with one amplifier (a line), the second with two amplifiers (a booster and a preamplifier)

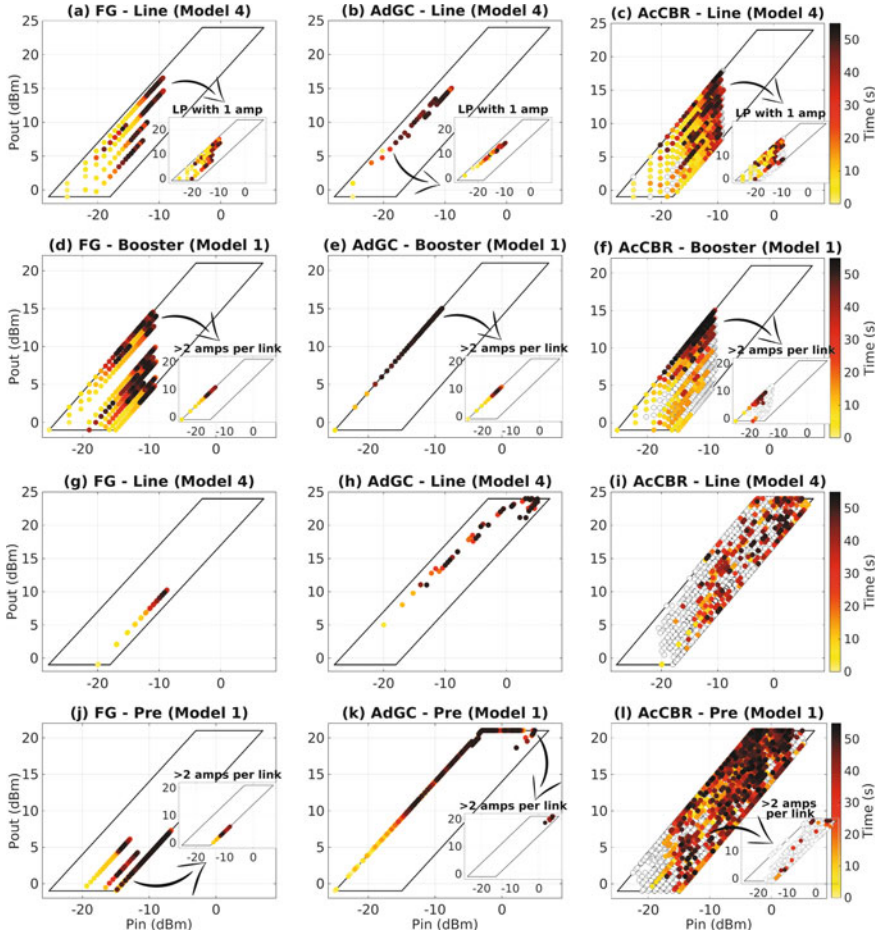

Fig. 8 Operating point evolution with the time inside the power mask for Biz Networks considering amplifiers models B1-L4-P1 (case 1) considering **a** FG, **b** AdGC and **c** AcCBR (max DB size) operating point evolution for line amplifiers in links with one amplifier; **d** FG, **e** AdGC and **f** AcCBR (max DB size) operating point evolution for booster amplifiers in links with two or more amplifiers; **g** FG, **h** AdGC and **i** AcCBR (max DB size) operating point evolution for line amplifiers in links with three or more amplifiers; **j** FG, **k** AdGC and **l** AcCBR (max DB size) operating point evolution for preamplifiers in links with two or more amplifiers

and the third link with three amplifiers (a booster, a line and a preamplifier). For this single LP, we will have one operating point in line (first row, a–c), corresponding to the single line amplifier on the LP first link; two operating points in booster (second row, d–f), corresponding to the booster amplifiers on the LP second and third links; one operating point in line (third row, g–i), corresponding to the line amplifier on the LP third link; and also two operating points in preamplifier (fourth row, j–l), corresponding to the preamplifiers on the LP second and third links.

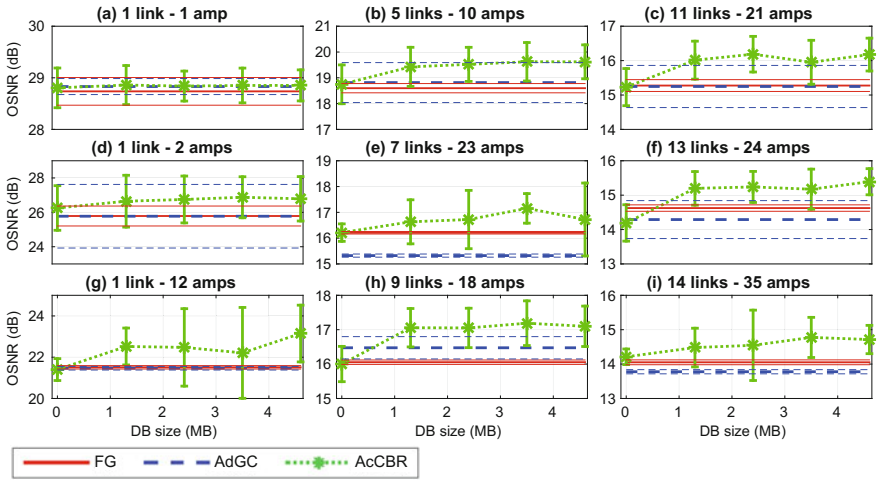

Fig. 9 Biz Networks simulation results with amplifiers B3-L4-P2 (case 2). Mean and standard deviation OSNR at the end of the LP per DB size for 10 repetitions of a RWA with 1000 connections and 500 erlang

Moreover, the maximum total input power for the first amplifiers on the link is approximately −9 dBm, which corresponds to the maximum channel load (40 channels) with −25 dBm each. This is why the operating points for line amplifiers in links with one amplifier (indices (a–c) in Figs. 8, 10, 12 and 14) and for booster amplifiers (indices (d–f) in Figs. 8, 10, 12 and 14 and indices (a–c) in Figs. 16 and 18) do not surpass this value.

On the power masks presented in Sects. 2 and 5 (Figs. 1, 2 and 6), the total input power variation was achieved by increasing/decreasing the channels power since all the characterization were performed considering a fixed 40 channels load. On the other hand, on the power masks presented in this Section, for the first amplifiers on the links, the total input power variation is caused by different channel loads. For additional amplifiers on the links, the total input power variation is due to both, channel load and channel power variations. Thus, we must be careful when comparing these figures, specially with Fig. 2, which presents OSNR values that are strongly dependent on the noise input.

Biz Networks results in terms of OSNR are shown in Figs. 7 and 9 for amplifiers models in case 1 (B1-L4-P1) and 2 (B3-L4-P2), respectively. This network presents LPs with up to 17 links and 40 amplifiers. The high number of links for such a small network is due to its ring topology, and the high maximum number of amplifiers is due to the presence of a single long link with 12 amplifiers, while all the others present up to two amplifiers (see Table 1). Biz Networks results for amplifier operating point evolution are presented in Figs. 8 and 10 considering amplifiers models in case 1 (B1-L4-P1) and 2 (B3-L4-P2), respectively.

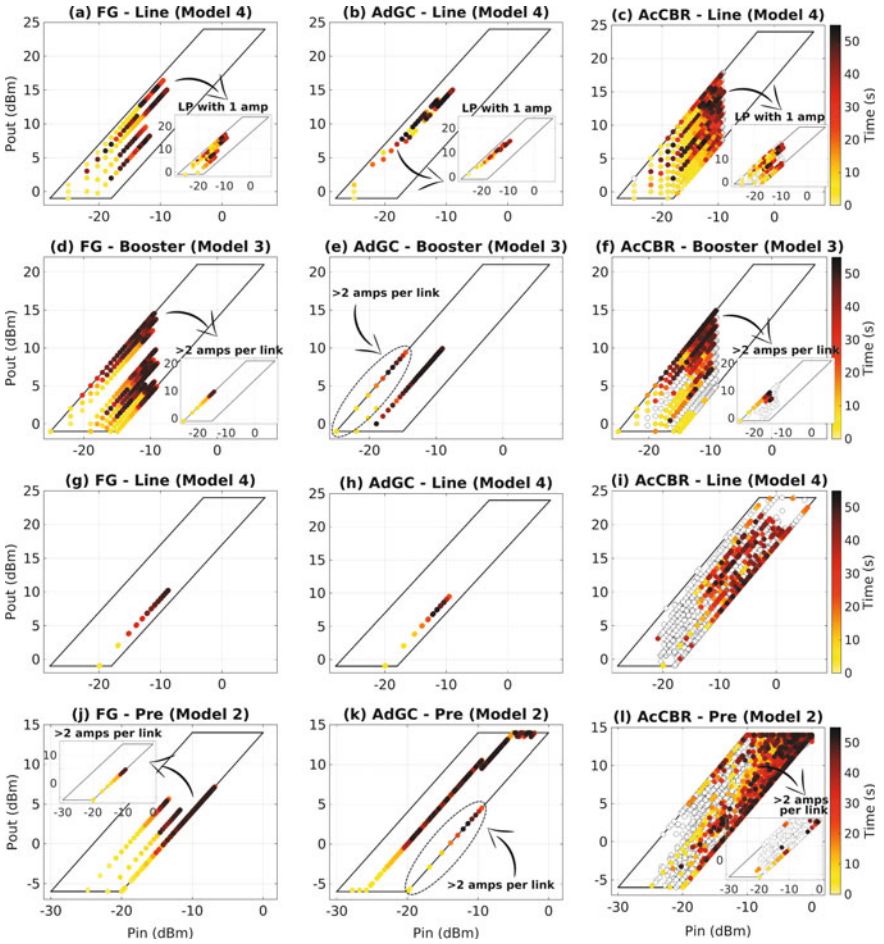

Fig. 10 Operating point evolution with the time inside the power mask for Biz Networks considering amplifiers models B3-L4-P2 (case 2) considering **a** FG, **b** AdGC and **c** AcCBR (max DB size) operating point evolution for line amplifiers in links with 1 amplifier; **d** FG, **e** AdGC and **f** AcCBR (max DB size) operating point evolution for booster amplifiers in links with two or more amplifiers; **g** FG, **h** AdGC and **i** AcCBR (max DB size) operating point evolution for line amplifiers in links with three or more amplifiers; **j** FG, **k** AdGC and **l** AcCBR (max DB size) operating point evolution for preamplifiers in links with two or more amplifiers

Figure 7a stands for LPs with one link and one amplifier. In this case, all methodologies present almost the same OSNR (around 28.8 $\pm$ 0.25 dB). Inset graphs in Fig. 8a–c can help our analysis. While the main graphs in Fig. 8a–c correspond to single amplifier links in LP with any number of links, the insets stand for line amplifiers in LPs with just one link and one amplifier, corresponding to the same scenario presented in Fig. 7a. From these operating points, we observe that FG (in Fig. 8a) presents different gains according to the respective link span loss. AdGC sets the

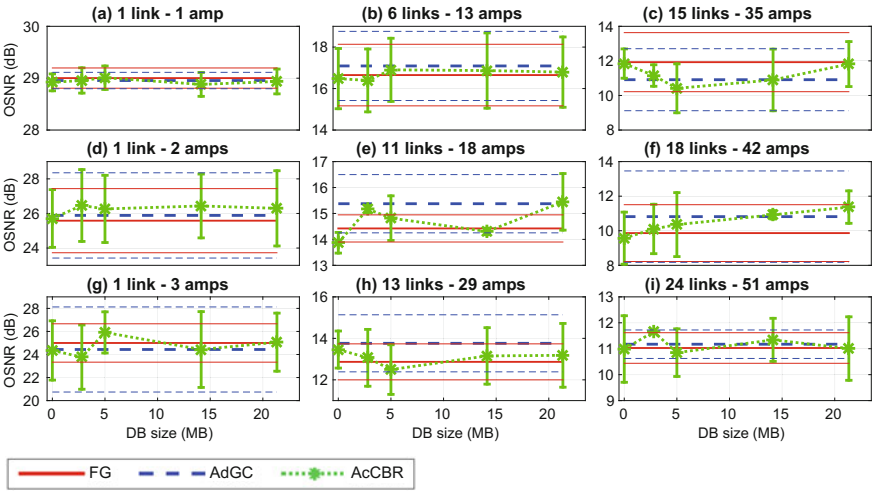

Fig. 11 Tata simulation results with amplifiers B1-L4-P1 (case 1). Mean and standard deviation OSNR at the end of the LP per DB size for 10 repetitions of a RWA with 1000 connections and 500 erlang

gain to the best trade-off between NF and GF, as presented Fig. 6e and f, which corresponds to a gain around 25 and 26 dB (see Fig. 8b). Finally, AcCBR (in Fig. 8c) presents an operating point distribution similar to the FG condition.

To complete our analysis, we will refer to Fig. 2 just because it presents only one amplifier as in Fig. 7a. For a single amplifier, Fig. 2 shows that the OSNR hardly changes with the amplifier gain for the same total input power. Thus, it is expected and consistent with the results presented in Fig. 7a, where the three methodologies present the same OSNR performance.

For the other Biz Networks LPs results in case 1 presented in Fig. 7b–i, FG presents the worst OSNR performance while AdGC presents the best one and AcCBR performance depends on the DB size. For an empty DB, AcCBR presents almost the same performance as in FG, and as the DB increases and the methodology obtains more experience, AcCBR reaches the AdGC performance (also considering the standard deviation). AcCBR improves mean OSNR (from minimum and maximum DB size) in approximately 1.4, 2.0, 0.6, 1.7, 1.5, 1.6, 2.5, and 3.3 dB for 5/10, 11/21, 1/2, 7/23, 13/14, 1/12, 9/18, and 14/35 link(s)/amps, respectively. Note that even for LP with 14 links/35 amps (Fig. 7i), in which AcCBR presents a low mean OSNR and a high standard deviation for a DB size near 2.5 MB, for higher DB (near 4 and 5 MB), it presents a high mean OSNR and a small standard deviation, showing the AcCBR convergence with DB size increasing.

These results can also be complemented by Fig. 8. In FG condition, comparing booster amplifiers operating point evolution in Fig. 8d with their respective optical performance presented in terms of NF and GF in Fig. 1 for amplifier model 1, we see that booster amplifiers present diverse operating points (in Fig. 8d) with

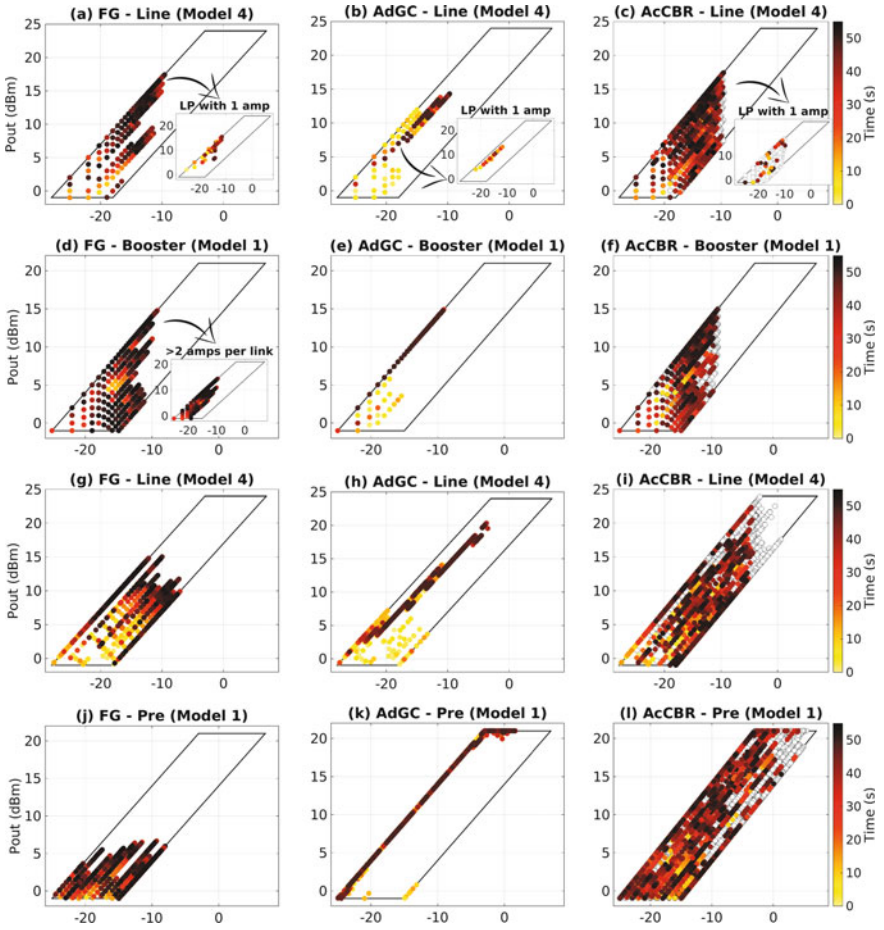

Fig. 12 Operating point evolution with the time inside the power mask for Tata considering amplifiers models B1-L4-P1 (case 1) considering **a** FG, **b** AdGC and **c** AcCBR (max DB size) operating point evolution for line amplifiers in links with one amplifier; **d** FG, **e** AdGC and **f** AcCBR (max DB size) operating point evolution for booster amplifiers in links with two or more amplifiers; **g** FG, **h** AdGC and **i** AcCBR (max DB size) operating point evolution for line amplifiers in links with three or more amplifiers; **j** FG, **k** AdGC and **l** AcCBR (max DB size) operating point evolution for preamplifiers in links with two or more amplifiers

different NF and GF performances (comparing with Fig. 1). Moreover, inset on Fig. 8d extracts the operating points for booster amplifiers in links with more than two amplifiers (>2 amps per link). In this case, booster amplifiers are set to a fixed 24 dB gain. For Biz Networks, just one link has more than two amplifiers. Thus, the line amplifiers on the third row refer to this link with 12 amplifiers (1B+10L+1P). Comparing the line amplifiers in Fig. 8g with their corresponding optical performance depicted in Fig. 6e and f for amplifier model 4, it is possible to observe that

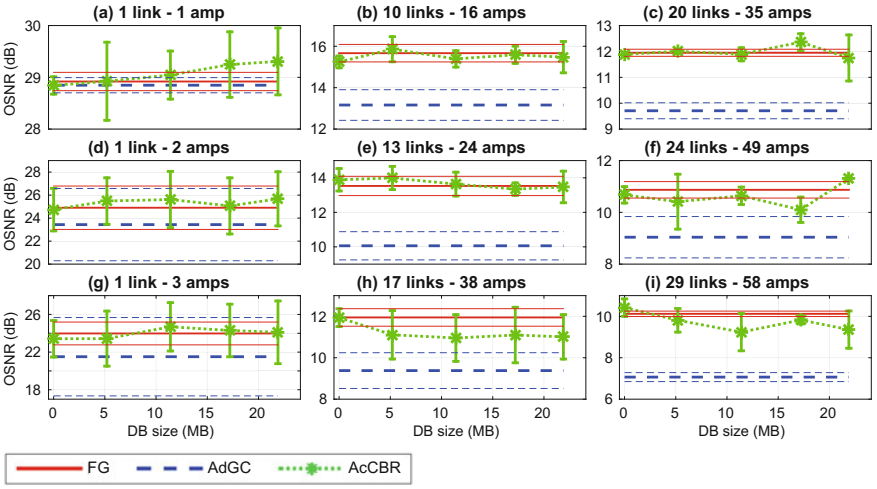

Fig. 13 Tata simulation results with amplifiers B3-L4-P2 (case 2). Mean and standard deviation OSNR at the end of the LP per DB size for 10 repetitions of a RWA with 1000 connections and 500 erlang

all line amplifiers in FG are set to 18 dB, which is not the best NF and GF region (this gain is set to compensate fiber and WSS losses). Finally, still in FG condition, comparing Fig. 8j with its corresponding optical performance in Fig. 1 also for amplifier model 1, preamplifiers are set to three different gains (14, 16 and 19 dB), which do not correspond to the best operating region in terms of NF and GF. Again, inset on Fig. 8j also extracts the operating points for preamplifiers on the link with more than two amplifiers (>2 amps per link). In this case, preamplifiers gains are set to 14 dB. Thus, we can conclude that, in FG condition, in which the gains of the amplifiers are set to compensate fiber span and passive component losses, a good system performance is not guaranteed since the amplifiers may not be on its best operating points.

Still on Fig. 8, to find the amplifiers (individual) best operating point, AdGC is applied. AdGC increases booster and preamplifier gains to its maximum value (see Fig. 8e and k, respectively), which corresponds to the best region in terms of NF and GF for amplifiers model 1 (Fig. 1). This higher booster gain also increases the total input power on the forward amplifiers, as can be observed on Fig. 8h and k for line and preamplifiers, respectively, in which AdGC is searching for their best operating points as their total input power increases. In fact, for Biz Networks, case 1, this local search provided by the AdGC has succeeded in finding the best gain combination providing the best system performance in terms of OSNR. Insets of Fig. 8e and k extract the amplifiers operating points for the link with more than two amplifiers (the single link with 12 amplifiers in Biz Networks). For this link, although booster amplifier presents the same operating points as in FG condition, as the line amplifiers (Fig. 8h) present a higher gain compared to FG, the total input power on

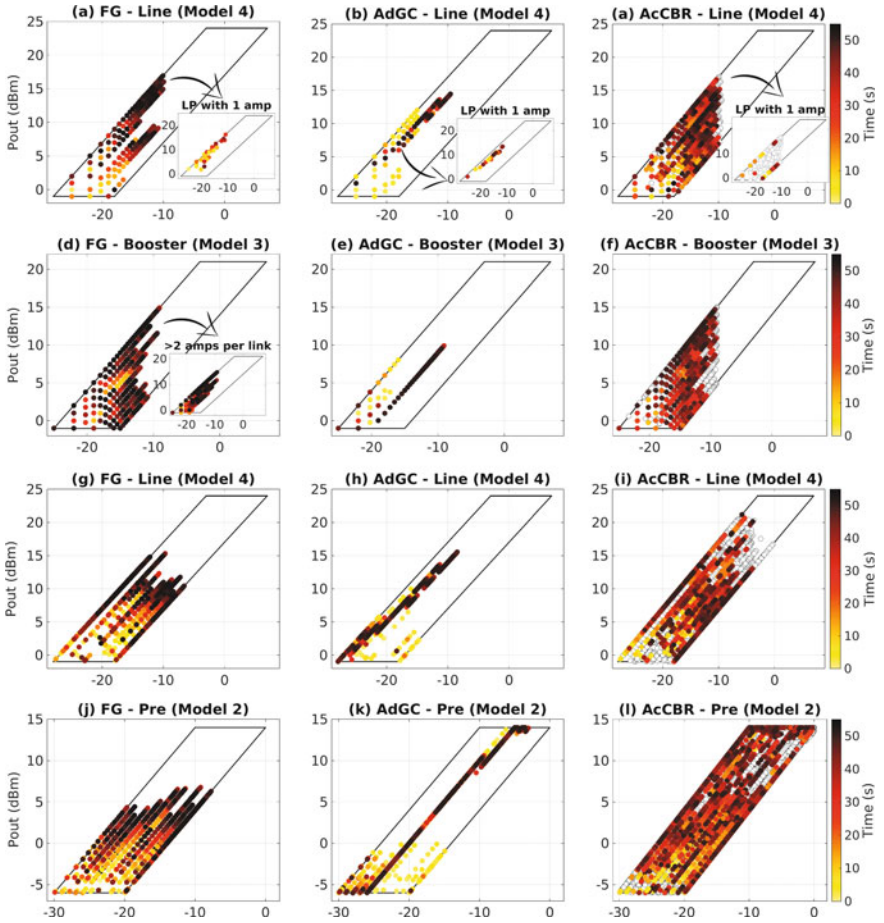

Fig. 14 Operating point evolution with the time inside the power mask for Tata considering amplifiers models B3-L4-P2 (case 2) considering **a** FG, **b** AdGC and **c** AcCBR (max DB size) operating point evolution for line amplifiers in links with one amplifier; **d** FG, **e** AdGC and **f** AcCBR (max DB size) operating point evolution for booster amplifiers in links with two or more amplifiers; **g** FG, **h** AdGC and **i** AcCBR (max DB size) operating point evolution for line amplifiers in links with three or more amplifiers; **f** FG, **g** AdGC and **h** AcCBR (max DB size) operating point evolution for preamplifiers in links with two or more amplifiers

the forward line amplifiers is increasing, until it reaches the preamplifier with high total input power. This high input power at the preamplifier leads to a better OSNR, even presenting the worst NF performance (see Fig. 1) as already discussed in Sect. 2.

Finally, to find the best combination, AcCBR is applied (Fig. 8f, i and l), trying to explore all possible operating points on the power mask while using the gain combination that provides the best OSNR performance achieved so far. Observe the high number of operating points used and evaluated by AcCBR in Fig. 8f, i and l. It

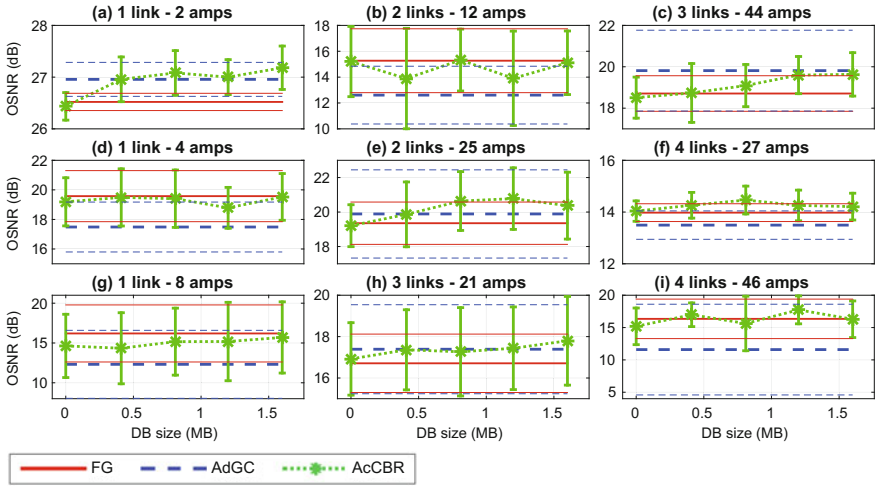

Fig. 15 China Telecom simulation results with amplifiers B1-L4-P1 (case 1). Mean and standard deviation OSNR at the end of the LP per DB size for 10 repetitions of a RWA with 1000 connections and 500 erlang

is important to point out that the evaluation of all possible operating points inside the power mask does not mean that the AcCBR will achieve the best performance. For AdGC, the operating points on the power mask refer to the best configuration obtained in this methodology for each amplifier individually. For AcCBR, on the other hand, even with a full evaluated power mask, it is not guaranteed that the best combination was tested.

Other important result that must be evaluated for Biz Networks in case 1 is the number of similar cases obtained during the AcCBR procedure (*retrieve* step) as a function of the DB size. This result is presented in Table 3 in terms of mean and standard deviation of similar cases for all the LPs evaluated in Fig. 7. As DB size increases, the number of similar cases also increases. But it is important to observe that just LPs (a), (d), and (g) present a significant amount of similar cases that helps the AcCBR to improve OSNR. But note also that the standard deviation in these three cases are too high, which means that some LPs do not have a high number of similar cases probably due to their total input powers or fiber losses. The other LPs remain with mean similar cases near zero. It is not consistent with the results presented in Fig. 7, where the OSNR improves with the DB size for all the cases. This result discrepancy can be explained by taking into account that, according to Fig. 5b, Biz Networks has just three kind of links: with 1, 2, and 12 amplifiers. Thus, since all LPs are composed of a combination of these links, when AcCBR attempts to optimize single link LPs (Fig. 7a, d and g), it ends up optimizing larger LPs that share these single link LPs.

Figure 9a shows OSNR results for LP with 1 link and 1 amplifier for Biz Networks in case 2 (amplifiers models B3-L4-P2). As the line amplifier model is the same as

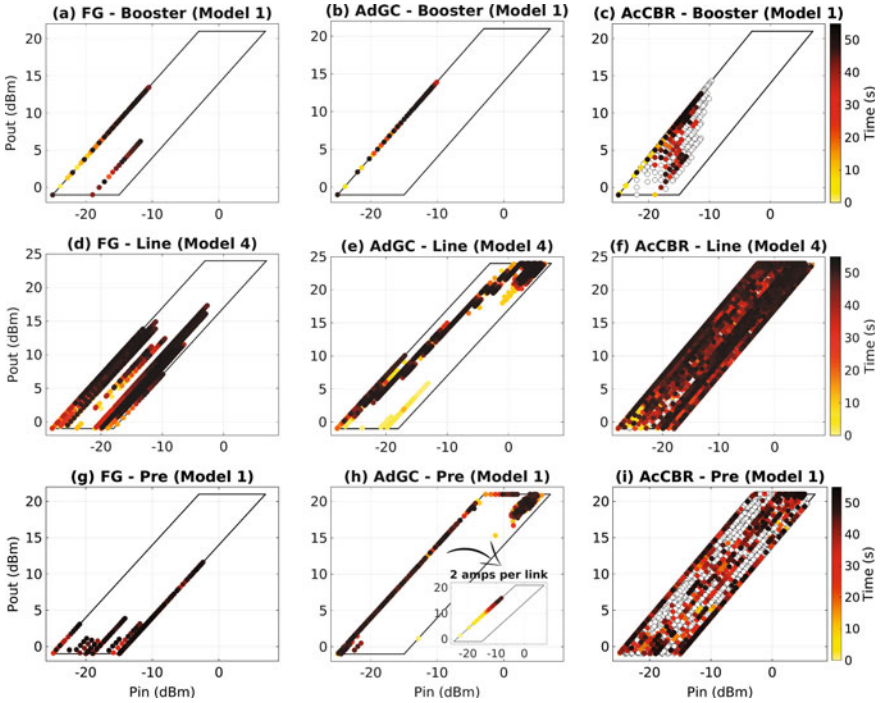

Fig. 16 Operating point evolution with the time inside the power mask for China Telecom considering amplifiers models B1-L4-P1 (case 1) considering **a** FG, **b** AdGC and **c** AcCBR (max DB size) operating point evolution for booster amplifiers in links with two or more amplifiers; **d** FG, **e** AdGC and **f** AcCBR (max DB size) operating point evolution for line amplifiers in links with three or more amplifiers; **g** FG, **h** AdGC and **i** AcCBR (max DB size) operating point evolution for preamplifiers in links with two or more amplifiers

in case 1 (model 4), the OSNR behavior is also the same, i.e., all methodologies presenting the same performance, with mean OSNR near 28.8 ± 0.25 dB. Also, the line amplifier operating points presented on Fig. 10a–c are on the same power mask region as for amplifier models B1-L4-P1 (Fig. 8a–c) for the three gain controls. Figure 10a–c insets extract the line amplifier operating points for LPs with a single amplifier, which corresponds to the same scenario presented in Fig. 9a.

Figure 9b–i present the mean and standard deviation OSNR for other LPs for Biz Networks in case 2. For all these LPs, AcCBR presents the best performance already on the first nonempty DB case (around 1.3 MB), improving the performance for higher DBs in most cases. FG and AdGC performances depend on the LP characteristic. For LPs with 11 links/21 amps (Fig. 9c), 1 link/2 amps (Fig. 9d), and 1 link/12 amps (Fig. 9g), FG and AdGC present the same mean OSNR performance; for LPs with 5 links/10 amps (Fig. 9b) and 9 links/18 amps (Fig. 9h), AdGC presents a better performance; and for LPs with 7 links/23 amps (Fig. 9e), 13 links/24 amps (Fig. 9f) and 14 links/35 amps (Fig. 9i), FG presents a better performance. The mean OSNR

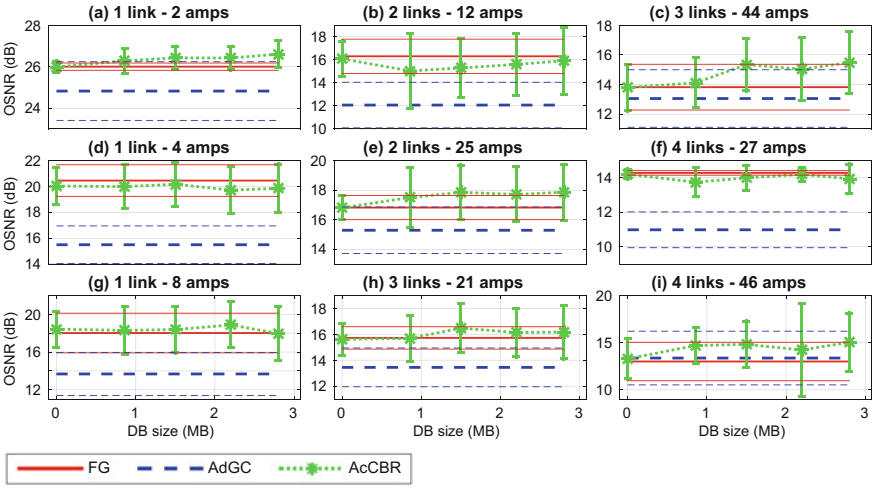

Fig. 17 China Telecom simulation results with amplifiers B3-L4-P2 (case 2). Mean and standard deviation OSNR at the end of the LP per DB size for 10 repetitions of a RWA with 1000 connections and 500 erlang

improvements were around 0.9, 1.0, 0.5, 0.5, 1.2, 1.8, 1.0, and 0.5 dB for 5/10, 11/21, 1/2, 7/23, 13/24, 1/12, 9/18, and 14/35 links/amps, respectively, from an empty DB to the maximum DB size in AcCBR.

Also, complementing the analysis with Fig. 10, which presents the operating point evolution for Biz Networks in case 2, we start with LPs with 1 link and 2 amplifiers (Fig. 9d), in which AdGC and FG present the same mean OSNR performance. Comparing Fig. 10e and k, which stands for booster and preamplifier (respectively) in AdGC condition with Fig. 10d and j, which also stands for booster and preamplifier (respectively) in FG condition, considering just the case with two amplifiers per link, AdGC presents very different gain distributions. Even with these differences in operating points, they present the same mean OSNR performance. We believe that these differences cause the high standard deviation presented in AdGC methodology in Fig. 9b.

In LPs with the link with 12 amplifiers (1/12, 7/23 and 14/35 links/amps), AdGC presents a worse (or the same for 1 link/12 amps) performance compared to FG. To better understand these results, we also recall to Fig. 10. For FG, Fig. 10d, g and j, considering just the case with more than two amplifiers per link (>2 amps per link), the amplifiers present the same operating points as for Biz Networks case 1 since the amplifiers gains are set to compensate passive losses. The unique difference is between preamplifiers models, since amplifier model 2 presents smaller output and input powers than model 1.

On the other hand, when AdGC is applied to LP with the link with 12 amplifiers (>2 amps per link), the gains in booster, line and preamplifiers are set as in FG in Fig. 10e, h, and k, respectively. It occurs because the AdGC and AcCBR maintain

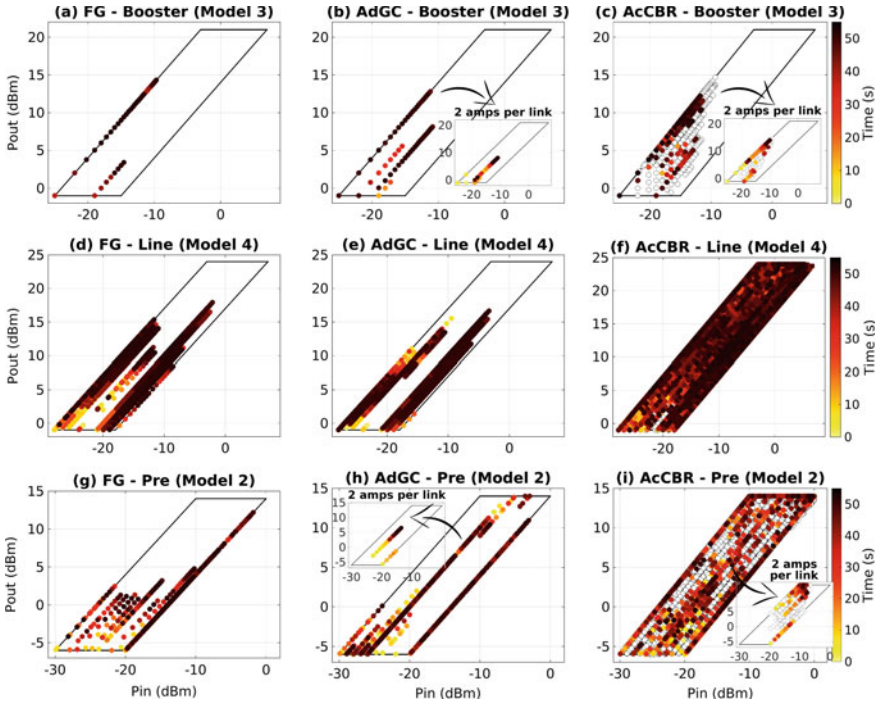

Fig. 18 Operating point evolution with the time inside the power mask for China Telecom considering amplifiers models B3-L4-P2 (case 2) considering **a** FG, **b** AdGC and **c** AcCBR (max DB size) operating point evolution for booster amplifiers in links with two or more amplifiers; **d** FG, **e** AdGC and **f** AcCBR (max DB size) operating point evolution for line amplifiers in links with three or more amplifiers; **g** FG, **h** AdGC and **i** AcCBR (max DB size) operating point evolution for preamplifiers in links with two or more amplifiers

the operating points inside the power mask, since this is the region where the amplifier performance is well known. For LPs with the link with 12 amplifiers, AdGC calculates the gains of the line amplifiers to a higher value than the FG due to its better performance (see Fig. 6e). Thus, as in Biz Networks case 1, this increase in line amplifier gain also increases the input power of the forward line amplifiers, until it reaches the preamplifier with a high input power. However, preamplifier model 2 does not support such a high total input power and AdGC does not apply the new gains for all the amplifiers in LP. In this case, the gains remain unchanged, i.e., they will remain as in FG, which corresponds to the initial condition for all the simulations.

Note that the previous explanation does not answer why AdGC performance is worse than FG, just that it should be the same. In fact, this is true for the LP with 1 link/12 amps (Fig. 9c). In the other LPs (7 links/23 amps and 14 links/35 amps), which present links with one or two amplifiers (besides the link with 12 amplifiers), AdGC might have changed previously the amplifier gains of these links. Thus, the

Table 3 Similar cases (mean $\pm \delta$) for Biz Networks with amplifiers B1-L4-P1 (case 1)

Link/amp	DB0	DB1	DB2	DB3	DB4
(a) 1/1	1.5 ± 1.8	32.6 ± 21.9	48.1 ± 35.7	57.1 ± 40.9	59.3 ± 47.5
(b) 5/10	0.2 ± 0.4	3.1 ± 4.0	5.4 ± 6.0	9.0 ± 10.6	11.6 ± 11.4
(c) 11/21	0.0 ± 0.0	0.2 ± 0.6	0.2 ± 0.5	0.3 ± 0.8	0.9 ± 1.1
(d) 1/2	3.1 ± 3.5	107.5 ± 79.5	154.7 ± 118.9	187.3 ± 152.1	229.5 ± 185.1
(e) 7/23	0.0 ± 0.0	0.6 ± 0.8	1.0 ± 1.1	1.8 ± 2.2	0.7 ± 1.1
(f) 13/24	0.0 ± 0.0	0.1 ± 0.3	0.4 ± 0.7	0.1 ± 0.3	0.2 ± 0.5
(g) 1/12	0.5 ± 0.9	13.4 ± 8.7	26.2 ± 11.6	40.6 ± 17.4	42.5 ± 19.6
(h) 9/18	0.0 ± 0.0	0.1 ± 0.3	1.5 ± 2.1	1.4 ± 2.1	1.2 ± 2.7
(i) 14/35	0.0 ± 0.0	0.0 ± 0.0	0.0 ± 0.0	0.0 ± 0.0	0.0 ± 0.0

Table 4 Similar cases (mean $\pm \delta$) for Biz Networks with amplifiers B3-L4-P2 (case 2)

Link/amp	DB0	DB1	DB2	DB3	DB4
(a) 1/1	1.1 ± 1.7	33.5 ± 19.9	46.6 ± 26.2	49.1 ± 28.2	55.9 ± 29.9
(b) 5/10	0.1 ± 0.3	1.9 ± 2.5	3.6 ± 3.8	3.7 ± 4.1	5.2 ± 5.4
(c) 11/21	0.0 ± 0.0	0.1 ± 0.4	0.2 ± 0.6	0.2 ± 0.7	0.4 ± 0.8
(d) 1/2	3.0 ± 3.3	73.5 ± 55.5	104.8 ± 75.3	138.4 ± 112.1	177.7 ± 136.3
(e) 7/23	0.1 ± 0.3	0.7 ± 1.1	0.5 ± 0.8	1.8 ± 2.5	1.1 ± 1.8
(f) 13/24	0.0 ± 0.0	0.1 ± 0.2	0.1 ± 0.5	0.1 ± 0.3	0.1 ± 0.3
(g) 1/12	0.3 ± 0.6	6.2 ± 2.7	6.8 ± 4.1	8.4 ± 3.3	8.5 ± 3.0
(h) 9/18	0.1 ± 0.2	0.1 ± 0.3	0.5 ± 1.3	0.9 ± 1.6	0.3 ± 0.6
(i) 14/35	0.0 ± 0.0	0.0 ± 0.0	0.0 ± 0.0	0.0 ± 0.0	0.0 ± 0.0

combination of the gains provided by FG on the link with 12 amplifiers, and the gains provided by AdGC on the other links resulted in a worst end-to-end performance compared to the pure FG condition.

Table 4 presents the similar cases obtained on the *retrieve* step during the AcCBR methodology for each LP in Fig. 9. Note that, just as in Biz Networks case 1, the LP with more similar cases with the maximum DB size was 1 link/2 amps, followed by 1 link/1 amps. LPs with 1 link and 12 amps present fewer similar cases at the maximum DB size when compared to the previous case (with amplifiers models B1-L4-P1). This is because of the high total input power applied to preamplifier model 2. Thus, just as in AdGC, AcCBR cannot increase the line amplifiers total output power to not surpass the preamplifier maximum total input power, this restriction reduces the possible gain combinations obtained in AcCBR and, consequently, the number of similar cases.

Moreover, even with some LPs with almost zero similar cases, the cognition behavior was observed for all LP cases in Fig. 9, once the optimization of single link LPs (Fig. 9a, d and g) provides the optimization of larger LPs, just as in Biz Networks previous case (with amplifiers models B1-L4-P1).

Summarizing the results for Biz Networks in case 1 and 2, independent on the LP characteristic and amplifier models, AcCBR always improves the mean OSNR values with the DB size, presenting a cognitive behavior for all evaluated LPs. It also presents a best or near best performance when compared to FG and AdGC for high DB for most LPs.

Tata results in terms of OSNR are shown in Figs. 11 and 13 for amplifiers models in case 1 (B1-L4-P1) and 2 (B3-L4-P2), respectively. Tata presents LPs with up to 34 links and 68 amplifiers. The maximum number of amplifiers is exactly twice the maximum number of links because Tata presents a mean of around two amplifiers per link with a small standard deviation (see Table 1). Tata results for amplifier operating point distribution is presented in Figs. 12 and 14 for amplifiers models in case 1 (B1-L4-P1) and 2 (B3-L4-P2), respectively.

Figure 11a stands for LPs with 1 link and 1 amplifier. In this case, as in Biz Network, all methodologies present around the same OSNR performance, near 29 dB, a little higher than the Biz Network results (around 28.8 $\pm$ 0.25 dB). This difference on the mean OSNR can be explained by comparing the amplifiers operating point for LP with 1 amplifier, presented in Fig. 12a–c, with the Biz Networks results presented in Figs. 8a–c and 10a–c, where we observed that there are higher operating points on Biz Networks results. This behavior is due to the higher probability to have a connection between two neighbor nodes in Biz Networks than in Tata, which is a bigger network, with five times more nodes and links than Biz Networks. Thus, the higher mean and low standard deviation for Tata compared to Biz Networks in LPs with 1 link and 1 amplifier maybe is due to the fewer points to calculate mean and standard deviation. AdGC, as expected, present the same operating point distribution, around the gain of 26 dB, since the amplifier model is the same for all cases.

Figure 11b–i present the mean and standard deviation OSNR for other LPs in Tata case 1, in which FG and AdGC mean OSNR performances depend on the LP, different from Biz Networks results in case 1 (Fig. 7b–i), in which AdGC presents a better performance than FG for all LPs. To understand this difference in AdGC behavior between these two networks in case 1, we recall to Fig. 12. First, lets analyze the FG condition in Fig. 12a, d, g, and j. Comparing with the same subfigures in Fig. 8, we observe that there are more set point gains in Tata, specially for line (d) and preamplifiers (j). This occurs because Tata presents almost five times more links than Biz, thus, presenting a more variety in span losses which require different setpoint gains in FG condition. This operating point dispersion in Tata for FG condition leads to a worse OSNR performance when comparing to Biz Networks LPs with the same number of amplifiers, i.e., Fig. 11d with Fig. 7d for LPs with two amplifiers, Fig. 11e with Fig. 7h for LPs with 18 amplifiers, and Fig. 11c with Fig. 7i for LPs with 35 amplifiers.

Comparing AdGC condition (b), (e), (h), and (k) on both networks in Figs. 8 and 12, we observe that AdGC optimizes all the amplifiers to their best set point gain (according to the best trade-off between NF and GF) in Biz Networks, while in Tata, at the beginning of the simulations (clearer dots), the amplifiers set point gains are more dispersive, as in FG condition. This occurs because as there are LPs with high number of links and amplifiers in Tata, the probability that one amplifier ends up out

of the power mask after applying AdGC is higher. Thus, to maintain the operating points inside the power mask, AdGC does not change the current amplifiers' gains, maintaining as in FG for the initial connections or as in AdGC previous gain configurations after some connections. Although AcCBR only applies FG at the beginning of the simulations, as we consider all the connections established on the network to estimate the mean OSNR, there is a degradation on final result. Explaining why AdGC presents a worse performance than FG in Tata (Fig. 11b–i) for some LPs, in which these initial LPs' OSNRs have more impact on the mean OSNR calculation.

Note that Tata has links with up to four amplifiers, and just one link with five amplifiers (see Fig. 5). Thus, one might expected, just as in Biz Networks, if AcCBR optimizes the performance of LPs with single links, it will also optimize LPs with higher number of links. However, observing Fig. 11b–i, there are some LPs that do not present this expected behavior, in which the AcCBR mean OSNR performance oscillates around the FG condition as the DB increase.

Moreover, AcCBR in Tata was performed with a DB size up to 22 MB, while in Biz Networks, DB is up to 5 MB. Thus, comparing similar LPs in Tata (Fig. 11a and d) and Biz Networks (Fig. 7a and d), which stand for LP with 1 link with 1 and 2 amplifiers (with same amplifier models), we observe that up to 5 MB, Tata presents the same behavior as Biz, i.e., mean OSNR improvements with the DB size. After this point, AcCBR converges to its final solution, presenting a small variations in mean OSNR values as DB size increases. We can also note that these LPs have found a considerable number of similar cases on the *retrieve* step, with a lower standard deviation (Table 5). Thus, we believe that the cognitive process works properly for these two LPs. On the other hand, it is not true for LP with 1 link and three amplifiers (Fig. 11g), which, as the most of the LPs in (Fig. 11), presents a mean OSNR oscillation, indicating that there is no convergence. It is also proved by the number of similar cases found on the AcCBR process (Table 5), in which mean value is too close to standard deviation, indicating that for some LPs, the AcCBR was not applied because there were no similar cases to use on the *reuse* step.

Thus, we believe that the noncognitive behavior for the most of the LPs in Fig. 11 is due to the fact that there is no convergence for at least one of the LPs with a single link. Thus, LPs with higher number of links that share this non-optimized single link LP will not be optimized as well. Moreover, it is harder to find similar cases for higher LPs (see Table 5), resulting in the non-application of AcCBR on these LPs.

Figure 11b and f are LPs with a high number of links and amplifiers presenting a suitable AcCBR performance, with mean OSNR improvements as DB size increases, even with a few number of similar cases in Table 5. We believe that it is possible since these LPs might have a considerable number of links with one and two amplifiers, achieving a good performance as single links LPs.

Figure 13a also stands for LPs with 1 link and 1 amplifier for Tata case 2. In this case, FG and AdGC presents almost the same performance as previous case (Tata with amplifiers models B1-L4-P1), while AcCBR presents higher OSNR improvement with DB when compared with all previous cases, reaching values around 29.3 ± 0.6 dB. Note that in Fig. 14c, for LPs with 1 amplifier, the operating points are concentrated on the region with lower gain. Also, in Table 6, despite these LPs

Table 5 Similar cases (mean $\pm \delta$) for Tata with amplifiers B1-L4-P1 (case 1)

Link/amp	DB0	DB1	DB2	DB3	DB4
(a) 1/1	0.1 ± 0.4	15.4 ± 8.8	23.4 ± 13.3	71.7 ± 45.0	80.0 ± 52.2
(b) 6/13	0.0 ± 0.1	0.1 ± 0.4	0.1 ± 0.4	0.7 ± 1.4	0.5 ± 1.2
(c) 15/35	0.0 ± 0.0	0.1 ± 0.3	0.0 ± 0.0	0.0 ± 0.0	0.1 ± 0.3
(d) 1/2	0.1 ± 0.4	13.0 ± 12.2	26.7 ± 20.8	76.3 ± 52.5	82.4 ± 57.4
(e) 11/18	0.0 ± 0.0	0.0 ± 0.0	0.0 ± 0.0	0.1 ± 0.3	0.0 ± 0.0
(f) 18/42	0.0 ± 0.0	0.0 ± 0.0	0.0 ± 0.0	0.0 ± 0.0	0.1 ± 0.2
(g) 1/3	0.0 ± 0.2	2.8 ± 3.6	10.2 ± 8.7	28.7 ± 29.3	37.5 ± 36.3
(h) 13/29	0.0 ± 0.0	0.1 ± 0.3	0.0 ± 0.3	0.1 ± 0.5	0.1 ± 0.8
(i) 24/51	0.0 ± 0.0	0.0 ± 0.0	0.0 ± 0.0	0.0 ± 0.0	0.0 ± 0.0

Table 6 Similar cases (meas $\pm \delta$) for Tata with amplifiers B3-L4-P2 (case 2)

Link/amp	DB0	DB1	DB2	DB3	DB4
(a) 1/1	0.1 ± 0.4	13.2 ± 7.8	27.5 ± 15.4	40.4 ± 21.5	66.8 ± 21.9
(b) 10/16	0.0 ± 0.0	0.0 ± 0.2	0.2 ± 0.5	0.1 ± 0.2	0.1 ± 0.4
(c) 20/35	0.0 ± 0.0	0.0 ± 0.0	0.0 ± 0.0	0.0 ± 0.0	0.0 ± 0.0
(d) 1/2	0.2 ± 0.5	11.5 ± 9.6	28.7 ± 21.3	43.7 ± 32.9	53.1 ± 37.2
(e) 13/24	0.0 ± 0.0	0.0 ± 0.2	0.0 ± 0.2	0.0 ± 0.0	0.1 ± 0.3
(f) 24/49	0.0 ± 0.0	0.0 ± 0.0	0.0 ± 0.0	0.0 ± 0.0	0.0 ± 0.0
(g) 1/3	0.0 ± 0.2	5.0 ± 3.6	12.9 ± 11.1	17.0 ± 11.1	21.4 ± 15.4
(h) 17/38	0.0 ± 0.0	0.0 ± 0.2	0.1 ± 0.3	0.0 ± 0.2	0.1 ± 0.4
(i) 29/58	0.0 ± 0.0	0.0 ± 0.0	0.0 ± 0.0	0.0 ± 0.0	0.0 ± 0.0

present a lower mean number of similar cases compared with the previous case (Tata with amplifiers models B1-L4-P1), they also present the lowest standard deviation, indicating that all LPs find sufficient similar cases and that its DB presents more diverse LPs. Thus, concentrated operating points on Fig. 14c and a mature DB in Table 6 indicate that AcCBR has converged for LPs with 1 link and 1 amplifier in Tata case 2.

Figure 13b–i presents the mean and standard deviation OSNRs for other LPs. Observe that in all these LPs, it seems that AcCBR tries to follow FG mean OSNR performance, which is the best for all cases. Also, observe that LPs with single links (Fig. 13d and g) do not show significant improvements over FG performance. Although, observing Table 6 for these same LPs, there are significant similar cases found for DB4, indicating that the methodology achieves the exploitation and exploration described in Sect. 3 (all the other LPs in Table 6 remain with the number of similar cases near to zero). Thus, as there is no OSNR improvements for single link LPs, it is even harder to improve the performance for higher LPs.

Regarding the operating point distribution in Fig. 14, we also observe, as in Fig. 12 (for Tata case 1), that in FG, all amplifiers (Fig. 14a, d, g, and j) set their gains to compensate fiber and WSS losses. In Fig. 14b, e, h and k, AdGC applies FG condition at the beginning of the simulations to prevent operating points out of the power mask for all the amplifiers. And finally, with AcCBR, the operating points are more distributed because AcCBR is evaluating the gain combinations.

In Biz Networks case 2 (Fig. 9b–i), AdGC presents a worse performance than FG just for LPs that have the link with 12 amplifiers because AdGC applies FG condition to prevent operating points out of the power mask. Now, as AdGC applies FG condition for most of the LPs just at the beginning of the simulations (see Fig. 14b, e, h and k), we observe an AdGC performance degradation for all the LPs in Fig. 13b–i. Recall that this degradation is expected even applying FG just at the beginning of the simulations because we consider all the connections to calculate mean OSNR.

Summarizing Tata analysis, AcCBR OSNR performance was near the best for most of the LPs on both cases (1 and 2). Moreover, even on the cases in which AcCBR degrades the OSNR compared to FG, it is always higher than the AdGC condition. Although, the similar cases values shown on Tables 5 and 6 and the noncognitive behavior (mean OSNR increasing with the DB size) indicate that an in-depth analysis must be performed to evaluate the AcCBR convergence for diverse LPs.

Finally, China Telecom results in terms of mean and standard deviation OSNR are shown in Figs. 15 and 17 for amplifiers models in case 1 (B1-L4-P1) and 2 (B3-L4-P2), respectively. Since China Telecom does not have links with 1 amplifier, these figures start showing LPs with 1 link/2 amps. This network presents LPs with up to 5 links and 77 amplifiers. This low maximum number of links for such a big size network is because of its hub characteristic, with two nodes densely connected. China Telecom results for amplifier operating point distribution inside the power mask are presented in Figs. 16 and 18 for amplifiers models in case 1 (B1-L4-P1) and 2 (B3-L4-P2), respectively.

Note that for all the LPs presented in Fig. 15 in which AdGC mean OSNR is better than FG, AcCBR presents a mean OSNR improvement with DB size, starting with the FG performance and ending up with a similar or better performance than AdGC for the maximum evaluated DB. These cases are: 1 link/ 2 amps, with AcCBR starting with 26.5 ± 0.35 dB (also FG performance) and ending with a mean OSNR higher than AdGC (27.2 ± 0.5 dB for AcCBR against 27 ± 0.4 dB for AdGC); 2 links/25 amps, in which AcCBR starts with 19.2 ± 1.3 dB (also FG performance) and ends again with a mean OSNR a little higher than AdGC (20.5 ± 2 dB for AcCBR against 20 ± 2.5 dB for AdGC); 3 links/21 amps, in which AcCBR starts with 16.9 ± 1.8 dB (near FG performance, 16.8 ± 1.5 dB) and ends again with a mean OSNR a little higher than AdGC (17.9 ± 2.2 dB for AcCBR against 17.6 ± 2.2 dB for AdGC); and 3 links/44 amps, in which AcCBR starts with 18.7 ± 1 dB (near FG performance, 18.8 ± 0.8 dB) and ends with a mean OSNR a little lower than AdGC, but with a lower standard deviation (19.6 ± 1 dB for AcCBR against 19.7 ± 2 dB for AdGC).

For the LPs in which FG presents a better performance than AdGC, mean OSNR in AcCBR remains near FG performance for all DBs, presenting some oscillations around it. Thus, AcCBR does not present a significant improvement for these LPs.

Table 7 Similar cases (meas $\pm \delta$) for China Telecom with amplifiers B1-L4-P1 (case 1)

Link/amp	DB0	DB1	DB2	DB3	DB4
(a) 1/2	0.1 ± 0.3	7.3 ± 5.7	10.2 ± 11.7	15.3 ± 13.8	19.1 ± 13.5
(b) 2/12	0.0 ± 0.2	0.7 ± 1.8	1.5 ± 3.0	2.3 ± 4.8	3.8 ± 6.3
(c) 3/44	0.0 ± 0.0	0.1 ± 0.4	0.1 ± 0.4	0.3 ± 0.6	0.3 ± 0.9
(d) 1/4	0.3 ± 0.6	4.9 ± 4.6	9.0 ± 8.7	13.6 ± 14.1	22.1 ± 17.7
(e) 2/25	0.0 ± 0.0	0.5 ± 1.0	0.7 ± 1.4	0.9 ± 1.7	1.1 ± 2.0
(f) 4/27	0.0 ± 0.1	0.1 ± 0.3	0.2 ± 0.4	0.2 ± 0.5	0.0 ± 0.2
(g) 1/8	0.1 ± 0.3	2.6 ± 2.9	7.7 ± 8.5	9.1 ± 11.6	10.9 ± 14.7
(h) 3/21	0.0 ± 0.2	0.1 ± 0.4	0.4 ± 0.7	0.5 ± 0.7	0.5 ± 0.7
(i) 4/46	0.0 ± 0.2	0.3 ± 0.6	0.2 ± 0.4	0.2 ± 0.4	0.8 ± 1.5

Observing Fig. 16, FG condition sets the gains of the amplifiers to a few gains in booster (Fig. 16a), to several gains in line and preamplifiers (Fig. 16d and g). Pre amplifiers in FG condition presents a low total input power. When AdGC is applied, there are a few operating points set as in FG condition for line and preamplifiers (Fig. 16e and h, respectively) at the beginning of the simulations, except for LPs with two amplifiers per link (inset graph in Fig. 16h). And with AcCBR, the operating points distribute along all possible regions on the power masks for line and amplifiers. Booster amplifier presents an empty region for low gain values, indicating that the AcCBR methodology did not explore all possible operating points for this amplifier. Recall that the exploitable region is limited by the maximum total input power (approximately -9 dBm).

Regarding AcCBR, Table 7 shows that almost all LPs present a nonzero mean of similar cases obtained on the *retrieve* step, indicating that the AcCBR methodology is acting for the most LPs. Thus, the non-optimization achieved for some cases might be due to a non-convergence of the methodology, which needs a bigger DB to improve the performance. Convergence issues versus DB size will be analyzed in-depth in future works.

Figure 17 presents the results for China Telecom with amplifiers models in case 2 (B3-L4-P2). For all LP cases in this figure, AdGC presents a worst performance when compared to FG condition, except for LPs with 4 links/46 amps, in which AdGC presents a slightly better performance than FG. Regarding AcCBR, it always presents a better performance than AdGC and it is possible to observe an OSNR improvement with the DB increase of 0.62 dB for LPs with 1 link/2 amps (Fig. 17a), 1.68 dB for LPs with 3 links/44 amps (Fig. 17c), 1.05 dB for LPs with 2 links/25 amps (Fig. 17e), and 1.75 dB for LPs with 4 links/46 amps (Fig. 17i). For the other cases, AcCBR presents mean OSNR very close to FG performance for all DBs, presenting some oscillations around it and without a significant improvement for these LPs.

Observe in Fig. 18 that, for FG condition, the gain of the amplifiers are also set to a few gains in booster (Fig. 18a) and to several gains in line and amplifiers (Fig. 18d and g). Inset in Fig. 18g shows the operating points for preamplifiers in links with

Table 8 Similar cases (meas $\pm \delta$) for China Telecom with amplifiers B3-L4-P2 (case 2)

Link/amp	DB0	DB1	DB2	DB3	DB4
(a) 1/2	0.2 ± 0.4	6.4 ± 5.2	9.7 ± 7.5	14.9 ± 8.9	15.6 ± 10.8
(b) 2/12	0.0 ± 0.1	1.4 ± 1.8	3.0 ± 3.6	4.2 ± 4.7	6.7 ± 7.3
(c) 3/44	0.0 ± 0.0	0.1 ± 0.4	0.3 ± 0.6	0.5 ± 0.8	0.5 ± 0.7
(d) 1/4	0.4 ± 0.6	11.3 ± 7.3	16.1 ± 12.1	23.4 ± 14.2	24.6 ± 17.6
(e) 2/25	0.1 ± 0.3	0.8 ± 1.1	1.3 ± 1.9	2.1 ± 3.1	2.6 ± 4.3
(f) 4/27	0.0 ± 0.0	0.1 ± 0.3	0.1 ± 0.3	0.2 ± 0.4	0.3 ± 0.6
(g) 1/8	0.2 ± 0.4	4.7 ± 3.5	9.7 ± 6.0	16.3 ± 11.4	20.6 ± 12.1
(h) 3/21	0.0 ± 0.1	0.3 ± 0.5	0.4 ± 0.6	0.5 ± 0.7	0.7 ± 0.8
(i) 4/46	0.0 ± 0.2	0.2 ± 0.4	0.3 ± 0.7	0.1 ± 0.5	0.8 ± 1.5

two amplifiers, in which FG sets a single gain. Considering AdGC, we observe that some operating points in Fig. 18b, e, and h are not on the best trade-off region from amplifiers models 3, 4, and 2, respectively (see Fig. 6), even for the inset graphs in Fig. 18b and h, which stand for booster and preamplifiers in links with two amplifiers. This operating point distribution degrades the OSNR values, as shown in Fig. 17, with AdGC presenting the worst OSNR performance. Finally, AcCBR application explores all the operating points in line and preamplifiers (Fig. 18f and i). Observe that booster (Fig. 18c) and the inset graphs in Fig. 18c and i, which corresponds to booster and preamplifiers in links with two amplifiers, do not have their entire exploitable region evaluated by the AcCBR.

Regarding AcCBR, Table 8 shows that all LPs present a nonzero mean of similar cases obtained on the *retrieve* step, indicating that the AcCBR methodology achieves the *reuse* step for these LPs. Again, some LPs were not optimized by AcCBR because the methodology did not converge, requiring a bigger DB to improve the performance.

Summarizing the results for China, AcCBR OSNR performance was again near the best or the best comparing to the FG and AdGC. Low improvements achieved by AcCBR may be caused by the need for a larger DB, as indicated on the power mask operating point distribution in AcCBR. These demanding a in-depth study on DB size and convergence in future works.

7 Conclusions

This work evaluates a cognitive methodology for optical amplifier gain adjustment, relied on case-based reasoning. We focus on realistic scenarios considering three meshed and dynamic optical networks with different characteristics in terms of size, topology, number of links and nodes, and amplifier models. We also assume different span lengths and number of amplifiers between nodes. The results show an OSNR

improvement when the cognitive methodology is applied for most cases, demonstrating that the proposed methodology can be applied for networks with different characteristics, presenting consistent performance regardless some oscillations and convergence issues, that do not degrade the performance and will be evaluated in-depth in future works.

References

1. Moura U, Garrich M, Carvalho H, Svolenski M, Andrade A, Cesar AC, Oliveira J, Conforti E (2016) Cognitive methodology for optical amplifier gain adjustment in dynamic dwdm networks. J Lightwave Technol 34:1971–1979
2. Reis JD, Garrich M, Pataca DM, Diniz JCM, Rozental VN, Carvalho LHH, Magalhes EC, Moura U, Gonzalez NG, Oliveira JRF, Oliveira JCRF (2014) Flexible optical transmission systems for future networking. In: Telecommunications network strategy and planning symposium (networks), 2014 16th international, pp 1–6
3. Cugini F, Meloni G, Paolucci F, Sambo N, Secondini M, Gerardi L, Poti L, Castoldi P (2012) Demonstration of flexible optical network based on path computation element. J Lightwave Technol 30:727–733
4. Franciscangelis C, Carvalho LHH, Reis JD, Parahyba VE, Simes FD, Pataca DM, Rosa ES, Rozental VN, Oliveira JRF, Gonzalez NG, Oliveira JCRF (2014) Network survivability field trial over brazilian legacy optical fiber links through advanced transponder reconfiguration. In: 2014 the European conference on optical communication (ECOC), pp 1–3
5. Carvalho LHH, Franciscangelis C, Duarte UR, Rozental VN, Reis JD, Fideles FB, Suzigan GJ, Simes FD, Parahyba VE, Gonzalez NG, Bordonalli AC, Oliveira JCRF (2014) Multidimensional optimization of optical spectral shaping for fiber nonlinearities mitigation in high baud-rate systems. In: 2014 the European conference on optical communication (ECOC), pp 1–3
6. de AS Diniz C, Garrich M, Suzigan GJ, Assine JS, Reis JD, de Oliveira JRF, Mello DAA (2015) Embedded system for optical spectral optimization based on a genetic algorithm. In: Microwave and optoelectronics conference (IMOC), 2015 SBMO/IEEE MTT-S international, pp 1–4
7. Choi HY, Liu L, Tsuritani T, Morita I (2013) Demonstration of ber-adaptive wson employing flexible transmitter/receiver with an extended openflow-based control plane. IEEE Photon Technol Lett 25(2):119–121
8. Magalhães E, Garrich M, Carvalho H, Magalhães M, González N, Oliveira J, Bordonalli A, Oliveira J (2014) Global wss-based equalization strategies for sdn metropolitan mesh optical networks. In: European conference on optical communications (ECOC)
9. Wang X, Fei Y, Razo M, Fumagalli A, Garrich M (2015) Network-wide signal power control strategies in wdm networks. In: 2015 international conference on optical network design and modeling (ONDM). IEEE, pp 218–221
10. Nascimento VV, de Oliveira JC, Ribeiro VB, Bordonalli AC (2011) Dynamic gain equalization for erbium doped fiber amplifiers based on optoceramic sinusoidal filter cascade. Microw Opt Technol Lett 53(3):623–626
11. de Moura UC, Oliveira JR, Oliveira JCR, Cesar AC (2013) Edfa adaptive gain control effect analysis over an amplifier cascade in a dwdm optical system. In: Microwave and optoelectronics conference (IMOC), 2013 SBMO/IEEE MTT-S international. IEEE, pp 1–5
12. Barboza DA, Bastos-Filho CJ, Martins-Filho JF, de Moura UC, de Oliveira JR et al (2013) Self-adaptive erbium-doped fiber amplifiers using machine learning. In: Microwave optoelectronics conference (IMOC), 2013 SBMO/IEEE MTT-S international. IEEE, pp 1–5

13. Oliveira JR, Caballero A, Magalhães E, Moura U, Borkowski R, Curiel G, Hirata A, Hecker L, Porto E, Zibar D et al (2013) Demonstration of edfa cognitive gain control via gmpls for mixed modulation formats in heterogeneous optical networks. In: Optical fiber communication conference. Optical Society of America, pp OW1H–2
14. Zervas GS, Simeonidou D (2010) Cognitive optical networks: need, requirements and architecture. In: 2010 12th international conference on transparent optical networks (ICTON). IEEE, pp 1–4
15. Mahmoud QH (2007) Front matter. Wiley, pp i–xxxii
16. Thomas RW, Friend DH, DaSilva L, Mackenzie AB et al (2006) Cognitive networks: adaptation and learning to achieve end-to-end performance objectives. IEEE Commun Mag 44(12):51–57
17. Monroy IT, Zibar D, Gonzalez NG, Borkowski R (2011) Cognitive heterogeneous reconfigurable optical networks (chron): enabling technologies and techniques. In: Proceedings of ICTON, vol 11
18. Wei W, Wang C, Yu J (2012) Cognitive optical networks: key drivers, enabling techniques, and adaptive bandwidth services. IEEE Commun Mag 50(1):106–113
19. Siracusa D, Salvadori E, Francescon A, Zanardi A, Angelou M, Klonidis D, Tomkos I, Sánchez D, Durán R, de Miguel I (2012) A control plane framework for future cognitive heterogeneous optical networks. In: 2012 14th international conference on transparent optical networks (ICTON). IEEE, pp 1–4
20. Tronco TR, Feres MM, César AC, de Lacerda Rocha M (2013) Self-configuration and self-healing for cognitive optical networks. J Microw Optoelectron Electromagn Appl (JMOe) 12:193–205
21. Tronco TR, Garrich M, César AC, Rocha MDL (2016) Cognitive algorithm using fuzzy reasoning for software-defined optical network. Photon Netw Commun 32(2):281–292
22. Rodríguez I, Durán RJ, Siracusa D, de Miguel I, Francescon A, Aguado JC, Salvadori E, Lorenzo RM (2013) Minimization of the impact of the ted inaccuracy problem in pce-based networks by means of cognition. In: 39th European conference and exhibition on optical communication (ECOC 2013). IET, pp 1–3
23. Zervas G, Banias K, Rofoee BR, Amaya N, Simeonidou D (2012) Multi-core, multi-band and multi-dimensional cognitive optical networks: an architecture on demand approach. In: 2012 14th international conference on transparent optical networks (ICTON). IEEE, pp 1–4
24. Jiménez T, de Miguel I, Aguado J, Durán R, Merayo N, Fernández N, Sánchez D, Fernández P, Atallah N, Abril E et al (2011) Case-based reasoning (cbr) to estimate the q-factor in optical networks: an initial approach. In: 2011 16th European conference on networks and optical communications (NOC). IEEE, pp 181–184
25. Jiménez T, Aguado JC, de Miguel I, Durán RJ, Fernandez N, Angelou M, Sánchez D, Merayo N, Fernández P, Atallah N et al (2012) A cognitive system for fast quality of transmission estimation in core optical networks. In: Optical fiber communication conference. Optical Society of America, pp OW3A–5
26. Jiménez T, Aguado JC, De Miguel I, Durán RJ, Fernández N, Angelou M, Sánchez D, Merayo N, Fernández P, Atallah N et al (2012) Enhancing optical networks with cognition: case-based reasoning to estimate the quality of transmission. In: 2012 IEEE international multi-disciplinary conference on cognitive methods in situation awareness and decision support (CogSIMA). IEEE, pp 166–169
27. Caballero A, Aguado JC, Borkowski R, Saldaña S, Jiménez T, de Miguel I, Arlunno V, Durán RJ, Zibar D, Jensen JB et al (2012) Experimental demonstration of a cognitive quality of transmission estimator for optical communication systems. Opt Expr 20(26):B64–B70
28. Jiménez T, Aguado JC, de Miguel I, Durán RJ, Angelou M, Merayo N, Fernández P, Lorenzo RM, Tomkos I, Abril EJ (2013) A cognitive quality of transmission estimator for core optical networks. J Lightwave Technol 31(6):942–951
29. Caballero A, Borkowski R, Zibar D, Monroy IT (2013) Performance monitoring techniques supporting cognitive optical networking. In: 2013 15th international conference on transparent optical networks (ICTON). IEEE, pp 1–4

30. Borkowski R, Caballero A, Klonidis D, Kachris C, Francescon A, de Miguel I, Barroso RJD, Zibar D, Tomkos I, Tafur I (2014) Advanced modulation formats in cognitive optical networks: EU project chron demonstration. In: Optical fiber communication conference. Optical Society of America, pp W3H–1
31. Borkowski R, Durán RJ, Kachris C, Siracusa D, Caballero A, Fernández N, Klonidis D, Francescon A, Jiménez T, Aguado JC et al (2015) Cognitive optical network testbed: EU project chron [invited]. J Opt Commun Netw 7(2):A344–A355
32. Duran R, Fernandez N, de Miguel I, Angelou M, Sánchez D, Aguado J, Jiménez T, Fernandez P, Merayo N, Atallah N et al (2011) Advantages of using cognition when solving impairment-aware virtual topology design problems. In: 2011 13th international conference on transparent optical networks (ICTON). IEEE, pp 1–4
33. Fernández N, Durán RJ, De Miguel I, Aguado JC, Jiménez T, Angelou M, Sánchez D, Fernández P, Merayo N, Atallah N et al (2012) Cognitive algorithm to solve the impairment-aware virtual topology design problem in reconfigurable optical networks. In: 2012 IEEE international multi-disciplinary conference on cognitive methods in situation awareness and decision support (CogSIMA). IEEE, pp 170–173
34. Tomkos I, Angelou M, Barroso RJD, de Miguel I, Toledo RML, Siracusa D, Salvadori E, Tymecki A, Ye Y, Monroy IT (2012) Next generation flexible and cognitive heterogeneous optical networks. The future internet. Springer, pp 225–236
35. de Miguel I, Durán RJ, Jiménez T, Fernández N, Aguado JC, Lorenzo RM, Caballero A, Monroy IT, Ye Y, Tymecki A et al (2013) Cognitive dynamic optical networks [invited]. J Opt Commun Netw 5(10):A107–A118
36. Moura U, Garrich M, Carvalho H, Svolenski M, Andrade A, Margarido F, Csar AC, Conforti E, Oliveira J (2015) Sdn-enabled edfa gain adjustment cognitive methodology for dynamic optical networks. In: 41th European conference and exhibition on optical communication (ECOC 2015). IET
37. Agrell E, Karlsson M, Chraplyvy AR, Richardson DJ, Krummrich PM, Winzer P, Roberts K, Fischer JK, Savory SJ, Eggleton BJ, Secondini M, Kschischang FR, Lord A, Prat J, Tomkos I, Bowers JE, Srinivasan S, Brandt-Pearce M, Gisin N (2016) Roadmap of optical communications. J Opt 18(6):063002
38. Govind PA (2002) Fiber-optic communication systems. Wiley, New York
39. Becker PM, Olsson AA, Simpson JR (1999) Erbium-doped fiber amplifiers: fundamentals and technology. Academic Press
40. Moura UC, Oliveira JR, Amgarten RL, Paiva GE, Oliveira JCF (2012) Caracterizador automatizado de máscara de potência de amplificadores ópticos para redes wdm reconfiguráveis. In: XXX Brazilian symposium on telecommunication, Brasilia, Brazil
41. Lumentum (2015) Multichannel erbium-doped fiber amplifier (EDFA)
42. de Moura UC, Oliveira JR, Cesar AC (2014) Roteamento de tráfego em redes wdm dinâmicas utilizando amplificadores ópticos com controle adaptativo de ganho. In: Anais do MOMAG 2014. IEEE, pp 7–12
43. Lopez De Mantaras R, McSherry D, Bridge D, Leake D, Smyth B, Craw S, Faltings B, Maher ML, Cox MT, Forbus K et al (2005) Retrieval, reuse, revision and retention in case-based reasoning. Knowl Eng Rev 20(03):215–240
44. Črepinšek M, Liu S-H, Mernik M (2013) Exploration and exploitation in evolutionary algorithms: a survey. ACM Comput Surv (CSUR) 45(3):35
45. T. U. of Adelaide (2013) The internet topology zoo
46. B. Hoppe (2009) Webwhompers
47. Dijkstra EW (1959) A note on two problems in connexion with graphs. Numer Math 1(1):269–271

Simulation-Based Optimization of OSNR on Under-Monitored EDFA-Based Optical Links Using Backpropagation Correction

Juliano Siloto Assine, Anderson Bravalheri, Heitor Carvalho, Miquel Garrich, Yue Fei, Xue Wang, Andrea Fumagalli and Juliano Oliveira

Abstract Existing networking infrastructure is often characterized by quasi-static and under-monitored settings. In the challenge to bring up these links into future networking paradigms such as Cognitive Networking (CN), introspection tools are important to feed decision-making algorithms with up-to-date data. The implementation of these tools on the other hand is greatly hindered by heterogeneity in the deployed infrastructure existing in most networks, requiring a greater flexibility provided by software-defined networking (SDN) technologies. In this work, we detail our recently proposed methodology to efficiently estimate and optimize OSNR on EDFA-based links with minimal network interruption. Then we provide clarifications on reported experiments and their methodology along with a detailed description of our experimental testbed. Moreover, we report new results on the simulation of various traffic load scenarios, validating this methodology for links operating under dynamic conditions.

1 Introduction

Optical networks are facing a deep change in traffic requirements: indeed, current Internet services exist in a multitude of different formats each with its own network requirements in terms of bandwidth, routing flexibility, and quality-of-service (QoS) indicators. In contrast, most existing core networks operate on quasi-static gradual allocation schemes and cannot respond quickly to changes [1]. To attend these increasing demands, new networking technologies are constantly deployed alongside existing legacy infrastructure leading to highly heterogeneous systems. In these scenarios, network management, typically performed by human operators, becomes an

J.S. Assine (✉) · A. Bravalheri · H. Carvalho · M. Garrich · J. Oliveira
Optical Technologies Divison, CPqD Foundation, Campinas, SP, Brazil
e-mail: jsiloto@cpqd.com.br

Y. Fei · X. Wang · A. Fumagalli
Open Networking Advanced Research (OpNeAR) Lab, Erik Jonsson School of Engineering and Computer Science, The University of Texas at Dallas, Richardson, TX, USA

A. Paradisi et al. (eds.), *Cognitive Technologies*, Telecommunications and Information Technology, DOI 10.1007/978-3-319-53753-5_10

increasingly complex task usually requiring high operational expenditure (OPEX) [2].

In this context, Cognitive Optical Networks (CONs) are regarded as a promising technology. As stated by de Miguel et al. [3] cognitive networks would surpass current network management processes which act mostly reactively to problems and provide a process able to perceive, learn, and act autonomously. This approach is based on three basic building blocks: the ability to assess the current network state (*Awareness*), the ability to adapt network configurations dynamically (*Adaptivity*) and the capacity to learn from previous states and act based on context (*Cognition*).

Although CONs are very promising in the near future, they require cross-layer capability, which is not possible in traditional optical networking infrastructure. Specifically, traditional networks are characterized by a vertical integration of the control and data planes which impedes fast innovation cycles and short time-to-market of new services and technologies. To overcome this limitation and to allow efficient *adaptability*, the network needs to be controlled in a transparent and unified way [4]. Fortunately, recent approaches on software-defined networking (SDN) decouple these planes providing a common control interface bringing up the network logic and programmability to a centralized point-of-view [5]. These concepts are applicable on optical communications where wavelength division multiplexed (WDM) equipment becomes custom-programmable to achieve improved end-to-end performance while maintaining a competitive cost of service [6].

In the effort to update deployed networks to these new paradigms, long-standing technologies such as Erbium-doped fiber amplifiers (EDFAs) need to be reconsidered in terms of service evolution and planning. EDFAs are traditionally deployed in links with limited monitoring alongside static Gain Flattening Filters. In these conditions, the amplifiers are configured to operate at their nominal gain, ensuring power flatness over a static channel load aiming to attend slowly increasing traffic conditions until full capacity is reached. In dynamic networks, EDFAs may not provide the expected performance using static gain configuration and reconfiguration may pose an even harder challenge when network monitoring is not available.

Optical Signal-to-Noise Ratio (OSNR) is widely used as a performance criterion in optical transmission, with a great role in the construction and deployment of optical amplifiers due to amplified spontaneous emission (ASE) noise. The improvement of OSNR in amplified transmission has been explored heavily by L. Pavel and Y. Pan as an optimization problem [7–10]. In this context, they formulated a framework for channel optimization on general topology WDM network based on pre-emphasis at optical switching nodes [10], they also consider factors such as convergence and stability of the optimization while attaining to link nonlinearity thresholds [11], but their work assumes networks with statically configured optical amplifiers with known spectral gain profile. B. Birand presents a solution to the channel power optimization problem based on monitoring feedback with the focus on minimizing power consumption [12]. This is applied in a mesh topology to configure both channel pre-emphasis and amplifier gains [13] presenting really fast reconfiguration times for channel add and drop scenarios. Their work addresses most of the challenges we discuss here but it requires the use of modern monitoring devices which may be

either not available on deployed scenarios or result in unfeasible capital expenditure (CAPEX) during planning. Furthermore, the optimization procedure used assumes a naive amplifier model with perfect flat gain. Predicting realistic EDFA behavior typically requires solving the nonlinear differential equations, which is not feasible in the operation phase due to the long computational time required. A popular solution relies on the use of previously characterized data such as power masks [14]. U. de Moura proposes an adaptive control methodology to choose amplifier gains by searching the power mask optimizing a scalar function of tilt and noise figures [15], later combined with filter pre-emphasis by Carvalho et al. [16]. Other solutions do not rely on amplifier model but solely on historical data [17].

Most centralized efforts either make unrealistic assumptions about amplifier behavior or depend on network monitoring while distributed approaches usually cannot guarantee global optimization. The ability to control the network depends on whether or not we can observe it, and in our case this is reflected on the per-channel behavior of amplifiers and how well we can measure it, directly or via computational models. In this work, we tackle this problem with the focus on developing physical-layer functionalities to fulfill the Awareness and Adaptivity requirements of CONs. Here we will present an example of how network state can be inferred even on under-monitored networks by providing an adaptable simulation framework leveraging on the fast numerical model proposed in [18]. Furthermore, we use this simulation to implement optimizations in the network, using search methods to improve optical signal-to-noise ratio (OSNR). This proposal is validated with the use of high-fidelity simulation tools and experiments on our metropolitan network testbed, presenting improvements in end-to-end transmission while minimizing network traffic interference.

This chapter is a detailed version of the work done in [19] with an improved description of the methods proposed and a clearer view of the experiments performed. Both the link model and backpropagation correction descriptions are extended to include the computation of noise power and thus, OSNR. Following, we provide an improved background and motivation on the optimization framework used along with a description of the algorithms. Finally we extend the results previously reported with an analysis of simulation performance under different traffic loads, highlighting the applicability in dynamic scenarios.

The rest of this work is organized as follows. In Sect. 2 we propose a simple link model used to compute the WDM spectrum at the input and output of every network device. Section 3 provides a problem formulation of improving prediction and OSNR on end-to-end optical connection. Section 4 proposes a correction technique to improve link prediction and Sect. 5 builds on it to propose a simulation scheme that minimizes network operations under a proposed OSNR optimization strategy. Section 6 describes the comparison of our simulation framework against high-fidelity simulation and Sect. 7 provide the validation experiments used on this framework. Section 8 concludes the paper with our final remarks.

2 Link Modeling

Optical links usually carry an aggregate of WDM signals distributed across the spectrum (represented in decibels by the function $S(f)$), each one with a different power. We can build a simplified description of the optical channels with a set of $S(f)$ samples, where the signal power $P(f)$ will be approximately equivalent to the peak values for each channel frequency f while the noise power $R(f)$ will be approximately the mean value of the closest valleys. Using this description we can easily compute $P(f)$ and $R(f)$ along an optical link, given we can predict the power behavior when optical signals traverse nonlinear elements such as EDFAs.

As pointed, the process of evaluating EDFA behavior is difficult and requires high computation power; in contrast, experimental characterizations can be done relatively easy during production and are good mechanisms for understanding the amplifier behavior. According to the algebraic model presented in [18], we can predict the amplifier behavior using only the total power input P_{in} and the target gain G_{set} based on the interpolation of characterized data. We can also use the noise characterization to build the amplifier noise figure $NF(G_{set})$ [14] and map the input and output of the amplifier as

$$p_{out}(f) = p_{in}(f)\, g(f, P_{in}, G_{set}) \tag{1}$$

$$r_{out}(f) = r_{in}(f)\, g(f, P_{in}, G_{set}) + f\, w\, h\Big(nf(G_{set})\, g(f, P_{in}, G_{set}) - 1\Big) \tag{2}$$

where h is Planck's constant, w is the sampling width used on measurement, $p(f)$, $r(f)$ and $nf(G_{set})$ are equivalent to the aforementioned $P(f)$, $R(f)$ and $NF(G_{set})$ values in linear scale, and $g(f, P_{in}, G_{set})$ represents the amplification profile for the EDFA.

Let us consider now the output prediction of an under-monitored optical link composed of N spans where each span individually is composed of several network elements (*NE*s). Our major goal is to describe in the most accurate way possible how these elements affect a given power spectrum input $S_{in}(f)$ at a given frequency f. Each *NE* can be modeled as a filter for $S(f)$ acting on its value additively. Each span n is composed of (i) one amplifier as previously described, (ii) a composition of fibers and attenuators with attenuation A_n and (iii) shaping filters with combined attenuation profile $F_n(f)$.

At the end of each span n we estimate the signal power $P_{n+1}(f)$ and the noise power $R_{n+1}(f)$ along the spectral frequency f. Each span is composed of (i) an amplifier modeled by the gain function $G_n(f, P_{in}(f), G_{set})$, (ii) a fiber length with attenuation and (iii) a shaping filter with attenuation profile $F_n(f)$, leading to Eqs. (3) and (4).

$$P_{n+1}(f) = P_n(f) + G_n(f, P_n, G_{set_n}) + A_n + F_n(f) \tag{3}$$

$$R_{n+1}(f) \approx Q_n(f) + G_n(f, P_n, G_{set_n}) + A_n + F_n(f) \tag{4}$$

where $Q_n(f) = 10 \log_{10}\left(r_{in}(f) + nf(G_{set}) f\, w\, h\right)$.

3 Problem Statement

Although prediction models can be useful in many occasions, the inherent uncertainty is exacerbated when trying to model a deployed network active for a prolonged time. Prediction errors are increased by component aging, which deteriorate original characteristics, however we can take these inaccuracies into account as long as we can measure them.

Let us consider $\hat{G}_n(f)$, the real amplifier gain at span n. The model uncertainty given by $\hat{G}_n(f) - G_n(f)$ is propagated at each span decreasing the prediction confidence in $P_N(f)$, the signal power at the last span. The prediction error at the end of the link is measured using the real signal power $P_D(f)$ and noise power $R_D(f)$ outputs provided by a deployed optical monitoring device (OPM) or by the receiver itself. This information can improve our prediction along the link, leading us to our first problem:

P1) Find the gain correction factor of each span. As shown in Fig. 1, a correction factor is required to the amplifier gain of each span. Thus a reevaluation of the power at each span is done by applying Eq. (5). Specifically, the problem is formulated as Find $G'_n(f)$ using the information provided by $P_D(f)$, such that $G'_n(f) \approx \hat{G}_n(f) - G_n(f)$.

$$P'_{n+1}(f) = P_{n+1}(f) + G'_n(f) \tag{5}$$

Moreover, a real-time prediction of the link can be used to improve transmission as we can reevaluate the network operating conditions based on any free parameters. Leveraging on this improved prediction, we need now to ensure every channel is above a minimum operational OSNR level at the receiver. Simultaneously, nonlinear per-channel k_1 and total power k_2 thresholds must be preserved along the link. We can model these considerations as an unbounded optimization problem by relaxing k_1 and k_2 thresholds with a penalty method. This leads to

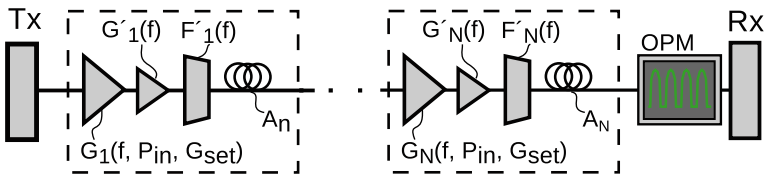

Fig. 1 Representation of an optical link with N spans. (*Tx*: Transmitter; *Rx*: Receiver; *G*: Gain; *f*: frequency; P_{in}: Total input power; G': Gain correction factor; *A*: Attenuation; *OPM*: Optical Power Meter)

P2) Maximize y **using** $x = [G_{set_1}, ..., G_{set_N}]$ **as decision variable** avoiding non-linear effects and ensuring minimum operational OSNR, where

$$y = \sum_f \left(P_n(f) - R_n(f)\right) - c_2 \max\left(k_2, \sum_f P_n(f)\right) - c_1 \max\left(k_1, \max_f\left(P_n(f)\right)\right) \quad (6)$$

4 Backpropagation Correction

In order to find G'_n as stated by P1, we assume each G'_n to be composed of a constant h_n and a polynomial $j_n(f) = w_0 + w_1 f + \cdots + w_d f^d$ thus $G'_n(f) = h_n + j_n(f)$. This distinction ensures G'_n to account for both total power (h_n) and power per-channel ($j_n(f)$) errors distinctly. Let E be the error function defined as

$$E = \sum_f \frac{1}{2}(P_N(f) - P_D(f))^2 \quad (7)$$

We can derive E in respect to j_n to fit the simulation using backward propagation of errors [20]. On each measurement, we update the parameters w_d according to Eqs. (8) and (9) over a number of epochs $t = 0, 1, \ldots, T$ with $w_d(0) = 0$ and $\Delta w_d(0) = 0$

$$w_d(t) = w_d(t-1) + \Delta w_d(t) \quad (8)$$

$$\Delta w_d(t) = \epsilon \frac{\partial E}{\partial w_d(t)} + \alpha \Delta w_d(t-1) \quad (9)$$

where ϵ and α are chosen learning rates and

$$\frac{\partial E}{\partial w_d} = \frac{\partial E}{\partial P_N} \frac{\partial P_N}{\partial P_{N-1}} \cdots \frac{\partial P_{n+2}}{\partial G'_n} \frac{\partial G'_n}{\partial w_d} \quad (10)$$

We assume that the total power change resulting from the addition of G'_n does not affect the model gain at span $n+1$ significantly, therefore

$$\frac{\partial G_{n+1}(f, P_{n+1}, G_{set})}{\partial G'_n} = 0 \longrightarrow \frac{\partial P_n}{\partial P_{n-1}} = 1 \quad (11)$$

Applying Eqs. (7) and (11) to Eq. (10), we finally obtain

$$\frac{\partial E}{\partial w_d} = f^d \sum_f \left(P_n(f) - P_D(f)\right) \quad (12)$$

Simultaneously, we apply the same process for h_n with different choices of ϵ and α where

$$\frac{\partial E}{\partial h_n} = \sum_f \left(P_n(f) - P_D(f)\right) \tag{13}$$

It is possible to apply the same approach to improve the noise prediction. Specifically, noise can be predicted with a separate correction factor by substituting $P_n(f)$ by $R_n(f)$ and $P_D(f)$ by $R_D(f)$ on Eqs. 7 throughout 13. Note that this is possible under the assumption that the amplifiers operate with a noise at the input greater than the ASE introduced by them. That is

$$r_{in}(f) * g(f, P_{in}, G_{set}) \gg (nf(G_{set}) * g(f, P_{in}, G_{set}) - 1) f\, h\, w \tag{14}$$

5 Optimization Based on Simulation

In the effort to solve the optimization problem proposed in Sect. 3, we provided an improved method to evaluate network conditions. Unfortunately, information about channel power alone is limiting in terms of possible optimization approaches. Both the numerical simulation and monitoring do not provide any introspection about the optical phenomenon itself and function topologies of $P_N(f)$ and $R_N(f)$ remain unknown. Typically this kind of black-box optimization is done by heuristics, but blind evaluation of amplifier configurations is undesirable as it may lead to traffic interruption. Circumstances such, where system evaluation is prohibitive, drive the need to use approximation techniques for decision-making [21]. In this section, we will present an optimization scheme which uses our adaptive numerical model presented in Sect. 4 as a proxy for the real system it represents. While the optimization routine may require a very large number of system evaluations, provided by the simulation, the simulation in turn is fed with purposely limited evaluations from the real system, acting only when the ability to emulate the real system is considered to be outside a trusted region. This is not a new concept, it can be found in the literature under the name of Simulation-Based Optimization (SO) with applications in diverse engineering fields such as wing-design [22] and urban traffic control [23]. Although usually used to speed-up complex high-fidelity simulations, where evaluation is prohibitively expensive, in this case we will use it to prevent unnecessary network disruption.

5.1 FANS

In this section, we propose the Feedback Assisted Network Simulation (FANS), a schema to decouple the optimization system evaluation from actual network operation, inspired in the model presented in Fig. 2.

Let x_0 be the current solution where G'_n is known. FANS evaluates if the euclidean distance between x_0 and a new solution x', is below a threshold δ. Then, it is considered to be trained and $P_n(f)$ and $R_n(f)$ are evaluated without querying the real network, assuming

$$|x' - x_0| < \delta \rightarrow G'_n|_{x=x_0} \approx G'_n|_{x=x'} \tag{15}$$

Otherwise, FANS applies x' to the physical network to update G'_n before evaluating the new solution. After updating G'_n, if x' does not represent an improvement, the last best network state (x_{curr}) is reverted. A functional representation of this process is shown in Fig. 3.

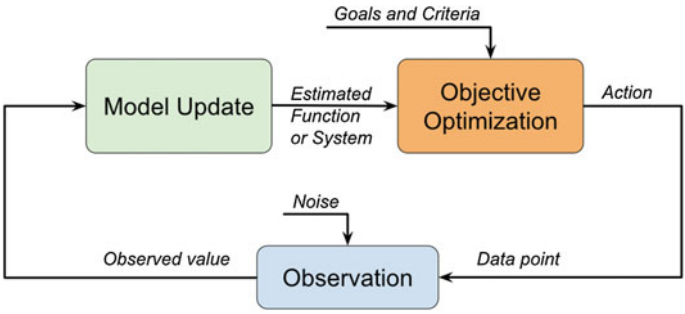

Fig. 2 Decision-making framework. Adapted from Alpcan T. (2013) [21]

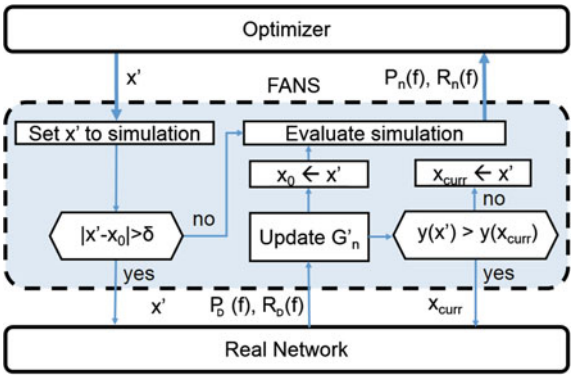

Fig. 3 Functional representation of FANS

Algorithm 1 Optimization

procedure NEIGHBOR(x)
  $p \leftarrow sum(x)$
  $d \leftarrow uniform(-1, 1)$
  $x \leftarrow \frac{x+d}{p}$
  for x_i in x **do**
    $x_i \leftarrow \max\left(\min\left(x_i, f+\right), f-\right)$
  return x
procedure OPTIMIZE(y(x))
  $x \leftarrow x_0$
  $x_{max} \leftarrow x_0$
  for $k : 0 \rightarrow k_{max}$ **do**
    $T \leftarrow \frac{k}{k_{max}}$
    $x_{new} \leftarrow Neighbor(x)$
    if $P(y(x), y(x_{new}), T) \leqslant random(0, 1)$ **then**
      $x \leftarrow NelderMead(x_{new})$
    if $y(x_{max}) \leqslant y(x)$ **then**
      $x_{max} \leftarrow x$
  return x_{max}

5.2 Optimization

The problem in hand presents both a high-dimensional search-space and very non-linear transitions, due those reasons a mixed optimization approach was chosen to run on top of FANS. Simulated Annealing [24] (SA) performs a *global* optimization based on a stochastic search using Monte Carlo sampling.

Each SA step draws a randomized neighbor and tests it for acceptance. Neighbors are chosen based on an uniform random distribution over the euclidean distance (Algorithm 1). In the step FANS usually transitions out of the trusted region reinforcing the global approach of the optimization. Once a new solution is accepted, Nelder–Mead algorithm [25], a simplex-based search procedure, performs *local* optimization. This step usually occurs only using numerical simulation enabling the Nelder–Mead algorithm to perform a large number of evaluations on an approximately linear region. This mixed approach is a slightly modified version of the algorithm first introduced in [26].

6 Validation Using High-Fidelity Models

In order to validate the methodology described in Sect. 4, an optical link, similar to the representation in Fig. 1, was simulated using the algebraic model with and without backpropagation correction. The spectrum for output power feedback was generated with high-fidelity physical-layer models, by the Optisystem® software. Intermediary spectra were also recorded using these models, providing a compara-

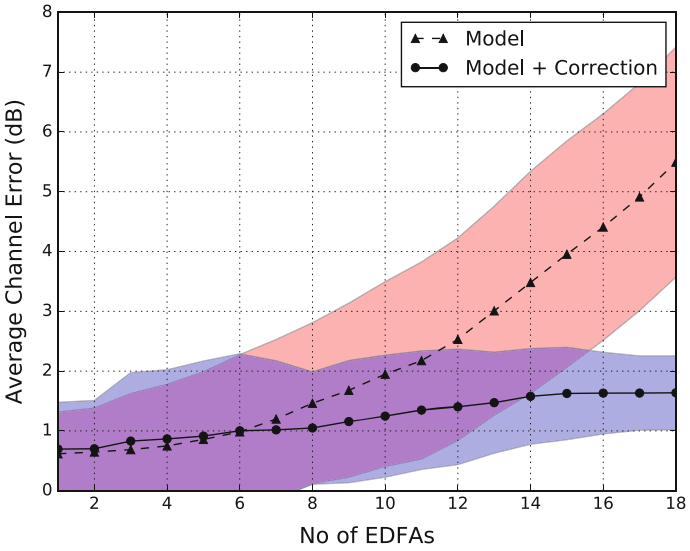

Fig. 4 Prediction error assuming the reference high-fidelity model in a 18 amplifier chain simulation. The *colored areas* around the *lines* represent the standard deviation for the different channels

tive basis for accuracy analysis. A total number of 18 spans composed by one EDFA, one WSS and 100 Km of fiber was selected to highlight the increasing distance impact in the estimation quality.

Figure 4 shows the average prediction error of $P_n(f)$ at each span, calculated from the absolute deviation of the estimated per-channel power and the recorded spectrum from Optisystem®. The first a few spans, up to 6, present similar behavior between the algebraic model and the one using our correction methodology. However, as the original model uncertainty propagates, the error is greatly mitigated by our back-propagation algorithm, reaching a reduction of 65% at the last span.

It is important to notice that the proposed correction mechanism also decreases the estimated spectrum variation. This means that, not only the average output power is corrected, but also the spectrum format gets more precise.

7 Experiments and Results

Experiment tests were carried out using the SDN testbed developed by the Autonomous Network (AN) project funded by the Brazilian Ministry of Communications [27]. This testbed, showed in Fig. 5, consists of an in-lab real network, dimensioned to emulate metropolitan mesh networks with dynamic configuration capabilities. Five nodes are interconnected bidirectionally in a partial-mesh topology using 100 Km of standard single-mode fiber (SSMF). Each node is a broadcast-

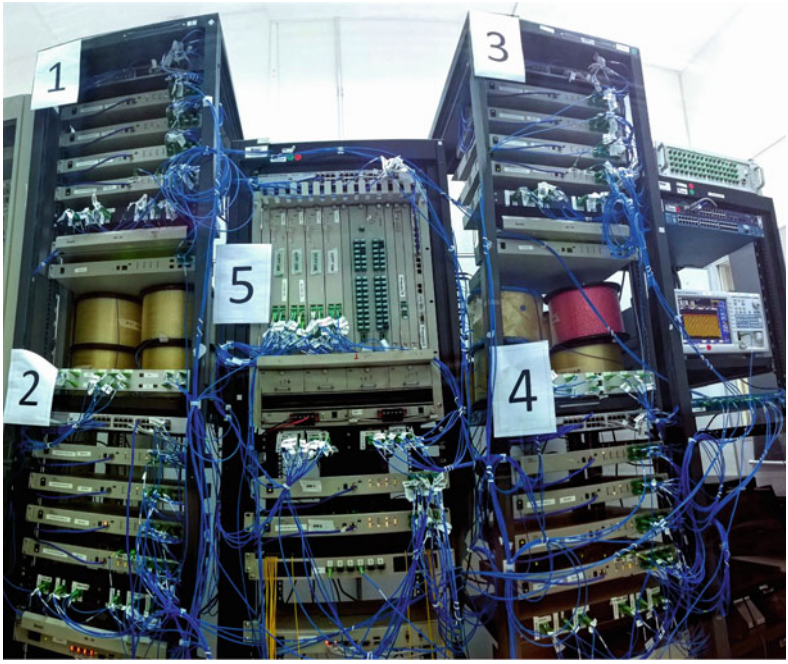

(a) Autonomous network testbed

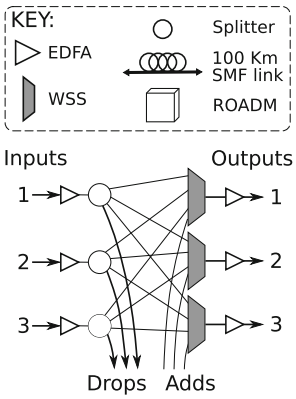

(b) Broadcast-and-select ROADM node

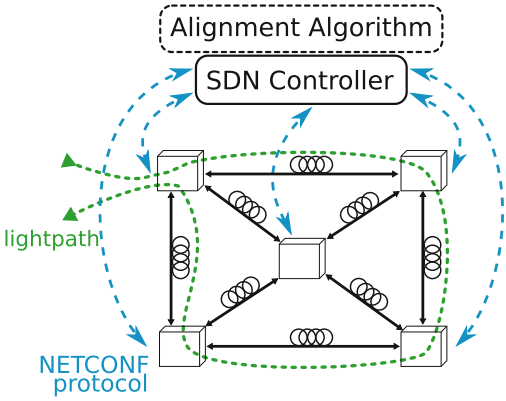

(c) Network schematics

Fig. 5 Experimental setup

and-select ROADM as depicted in Fig. 5, allowing lightpaths to be routed directly in the optical domain. Two EDFAs per link (one at the beginning and one at the end) are used to compensate fiber and node attenuations. Spectral content of the EDFA before the splitter at ROADMs can be tracked connecting its *monitoring* port with

an optical spectrum analyzer (OSA). All equipment is connected to the SDN Controller with NETCONF protocol, using the testbed infrastructure itself, via optical supervisory channel (OSC) with 1.25 Gb/s Ethernet transceivers at 186.2 THz.

We configured a lightpath across four nodes including eight amplifiers due to the network topology. The amplifiers in the testbed do not include GFF and were configured in their nominal gain. No additional attenuation was introduced in the optical switches. As input, a WDM signal with 39 channels from C-band distributed between 192.1 and 196.0 THz was injected in the *add* port of the first node. This number was intentionally selected, because the spacing between each channel permits using the OSA trace for measuring OSNR.

Three experiments were carried out. First, we evaluated the improvement provided by the backpropagation methodology against the original model by examining the average error per channel at every other amplifier in the lightpath on an unequalized scenario. Second, we analyzed the consistency of this method for a dynamic network by comparing the average error per channel under random channel configurations at four different number of present channels. Finally, we tested the applicability of FANS for an optimization application executing the algorithm described in Sect. 5 and comparing the number of function evaluation and the actual number of configurations applied to the network.

Figure 6a shows a comparison between the spectral content estimation every two amplifiers, using a simple algebraic model and the backpropagation methodology described in Sect. 4. The signal, noise power, and the OSNR were computed taking the absolute difference between OSA measurement and estimated values. Results

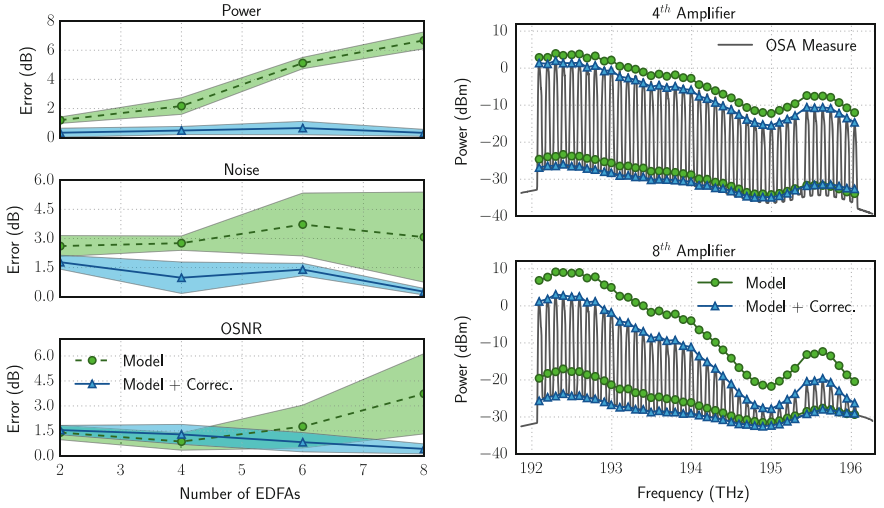

(a) Figures of merit **(b)** Optical spectra

Fig. 6 Comparison of spectrum predictions with correction (*blue*) and without (*green*) in a eight amplifier chain experiment

show significant benefits of using the proposed methodology: the power estimation error diminishes 78% at the fourth node and 95% at the last one, while noise power estimation error decreases respectively 64.5% and 91.5% at the same locations. There is a 50% increasing of OSNR error at the fourth node and a 88.7% decreasing at the network output. Despite of the higher OSNR estimative error in the lightpath beginning, the backpropagation proposal provides an overall more accurate estimative of the spectrum format, as pointed by the qualitative results in Fig. 6. This improvement is obtained thanks to the zero-order term consideration in our correction, which counteracts the spectrum total power uncertainty propagation.

In addition, expected operating conditions were simulated using the same eight-span lightpath topology imposed over the network, the amplifiers were initially configured to the nominal gain and the attenuation profile for each WSS was found by equalizing the per-channel power [16]. On such conditions, the prediction methodology was tested against different channel allocation schemes. Four total configurations of active channels were chosen, for each one, 10 random sets of channels were chosen and simulated. The average prediction errors for all channels on all random sets were registered and average per-channel signal, noise and OSNR errors can be seen in Table 1a–c respectively, where the average error for all measures is mostly around 1.0 dB, showing no evident shortcoming in relation to the number of channels used.

Table 1 Prediction errors under different channel loads

Active channels	Stage			
	2	4	6	8
(a) Power error (dB)				
08	0.72 ± 0.61	0.76 ± 0.63	0.84 ± 0.64	0.79 ± 0.49
16	0.56 ± 0.47	0.45 ± 0.36	0.75 ± 0.65	0.57 ± 0.45
24	0.52 ± 0.44	0.68 ± 0.57	0.55 ± 0.45	0.58 ± 0.50
32	1.46 ± 2.40	0.50 ± 0.40	0.60 ± 0.48	0.55 ± 0.50
39	0.49 ± 0.33	0.49 ± 0.34	0.57 ± 0.48	0.56 ± 0.50
(b) Noise error (dB)				
08	1.35 ± 0.89	1.48 ± 1.14	1.12 ± 0.89	0.89 ± 0.58
16	1.08 ± 0.57	1.03 ± 0.77	1.01 ± 0.74	0.54 ± 0.46
24	1.11 ± 0.58	0.97 ± 0.75	0.70 ± 0.59	0.44 ± 0.30
32	1.44 ± 1.05	0.92 ± 0.64	0.68 ± 0.53	0.38 ± 0.30
39	1.05 ± 0.54	0.90 ± 0.52	0.70 ± 0.57	0.59 ± 0.74
(c) OSNR error (dB)				
08	1.40 ± 1.08	1.31 ± 0.98	0.75 ± 0.64	0.62 ± 0.55
16	1.08 ± 0.69	1.01 ± 0.72	0.85 ± 0.59	0.58 ± 0.48
24	1.02 ± 0.62	0.84 ± 0.60	0.70 ± 0.49	0.60 ± 0.45
32	1.42 ± 1.14	0.87 ± 0.58	0.75 ± 0.54	0.62 ± 0.48
39	0.71 ± 0.43	0.78 ± 0.53	0.68 ± 0.56	0.83 ± 0.72

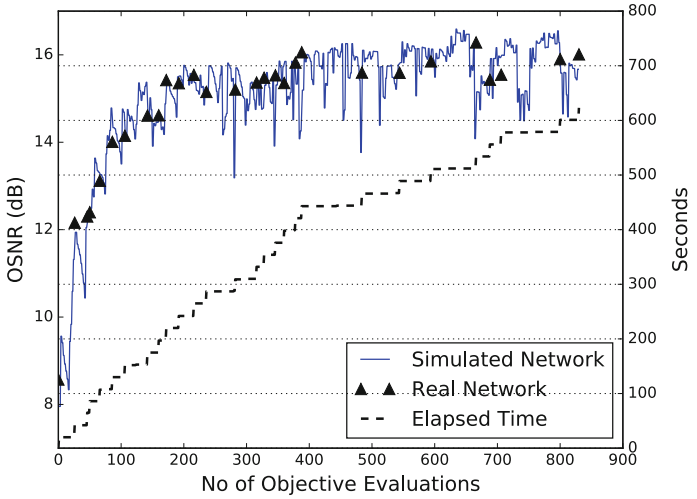

Fig. 7 OSNR change over one optimization run

Finally, a SDN application implementing the algorithm described in Sect. 5 was evaluated in order to validate the proposed methodology. An additional channel-independent attenuation was introduced in order to decrease the minimum output OSNR to approximately 8 dB, thereby, providing a good margin for optimization. Figure 7 shows the evaluation results. A very quick convergence, 80% of the OSNR improvement at the last span is achieved in less than 3 min, with less than 10 network interactions (triangular symbols).

8 Conclusions

We proposed a backpropagation error correction technique with feedback from an SDN-enabled optical network (FANS) to assist an optimization engine. Results showed that FANS greatly reduces simulation error accounting only on monitoring information from the last span. Furthermore, the simulation engine here proposed is applicable for different allocation schemes with little variation in prediction errors, proving it can be employed in links with highly time varying allocation. Finally, a practical application of FANS was shown to improve signal quality with a reduced number of network interactions thanks to FANS' efficient numerical simulation model.

In summary, estimation models can be allied with real-time measurement to enable cognitive technologies in optical communications. Real network behavior may deviate considerably from the original planned conditions throughout time and it is imperative that network management can be able to foresee this behavior trans-

parently and easily adapt to new operating conditions. Here we applied this concept predicting the gain behavior of EDFAs within a margin of measured points using FANS logic. Further works involve improving the network model and the prediction errors over time by learning from previous data.

Acknowledgements Authors thank the financial support of FUNTTEL under the project 100GETH. M. Garrich thanks CNPq (grant 312047/2015-0).

References

1. Woodward SL, Feuer MD (2010) Toward more dynamic optical networking. In: Optoelectronics and communications conference (OECC), 2010 15th, pp 114–115
2. Borkowski R (2014) Enabling technologies for cognitive optical networks
3. de Miguel I, Durán RJ, Jiménez T, Fernández N, Aguado JC, Lorenzo RM, Caballero A, Monroy IT, Ye Y, Tymecki A et al (2013) Cognitive dynamic optical networks [invited]. J Opt Commun Netw 5(10):A107–A118
4. Ahmad I, Namal S, Ylianttila M, Gurtov A (2015) Towards software defined cognitive networking. In: 2015 7th international conference on new technologies, mobility and security (NTMS), pp 1–5. IEEE
5. Kreutz D, Ramos FMV, Verssimo PE, Rothenberg CE, Azodolmolky S, Uhlig S (2015) Software-defined networking: a comprehensive survey. In: Proceedings of the IEEE, vol 103, pp 14–76
6. Gringeri S, Bitar N, Xia TJ (2013) Extending software defined network principles to include optical transport. IEEE Commun Mag 51:32–40
7. Pavel L (2006) Osnr optimization in optical networks: modeling and distributed algorithms via a central cost approach. IEEE J Sel Areas Commun 24(4):54–65
8. Pan Y, Alpcan T, Pavel L (2008) A distributed optimization approach to constrained OSNR problem. In: IFAC proceedings volumes, vol 41, no 2, pp 2895–2900
9. Pan Y, Alpcan T, Pavel L (2010) A system performance approach to OSNR optimization in optical networks. IEEE Trans Commun 58:1193–1200
10. Pan Y, Pavel L (2014) OSNR game optimization with link capacity constraints in general topology WDM networks. Opt Switching Netw 11:1–15
11. Agrawal G (2002) Fiber-optic communication systems. Wiley series in microwave and optical engineering. Tsinghua University Press
12. Birand B, Wang H, Bergman K, Zussman G (2013) Measurements-based power control-a cross-layered framework. In: National fiber optic engineers conference, pp JTh2A–66, Optical Society of America
13. Birand B, Wang H, Bergman K, Kilper D, Nandagopal T, Zussman G (2014) Real-time power control for dynamic optical networks—algorithms and experimentation. IEEE J Sel Areas Commun 32(8):1615–1628
14. Bastos-Filho CJ, Barboza EdA, Martins-Filho JF, de Moura UC, de Oliveira JR (2013) Mapping EDFA noise figure and gain flatness over the power mask using neural networks. J Microw Optoelectron Electromagn Appl (JMOe) 12:128–139
15. De Moura UC, Oliveira JR, Oliveira JC, Cesar AC (2013) EDFA adaptive gain control effect analysis over an amplifier cascade in a DWDM optical system. In: Microwave and optoelectronics conference (IMOC), 2013 SBMO/IEEE MTT-S International, pp 1–5, IEEE
16. Carvalho H, Magalhães EC, Alabarce MG, Gonzalez NG, Nascimento M, Margarido F, Mariote L, Bordonalli A, Oliveira JR (2015) SDN dual-optimization application for EDFAs and WSS-based ROADMs. In: Optical fiber communication conference (Washington, D.C.), p Th3J.4, OSA

17. Moura U, Garrich M, Carvalho H, Svolenski M, Andrade A, Margarido F, Cesar AC, Conforti E, Oliveira J (2015) SDN-enabled EDFA gain adjustment cognitive methodology for dynamic optical networks. In: 2015 European conference on optical communication, pp 1–3, IEEE, sep 2015
18. Fei Y, Fumagalli A, Garrich M, Sarti B, Moura U, Gonzlez NG, Oliveira J (2015) Estimating EDFA output power with an efficient numerical modeling framework. In: 2015 IEEE international conference on communications (ICC), pp 5222–5227, June 2015
19. Assine JS, Bravalheri A, Carvalho H, Garrich M, Fei Y, Wang X, Fumagalli A, Oliveira J (2016) SDN-enabled backpropagation correction for OSNR estimation and optimization in under-monitored EDFA-based optical links. In: ECOC 2016; 42nd European conference on optical communication; Proceedings of, pp 1–3, VDE
20. Rumelhart DE, Hinton GE, Williams RJ (1986) Learning representations by back-propagating errors. Nature 323:533–536
21. Alpcan T (2013) A framework for optimization under limited information. J Global Optim 55(3):681–706
22. Alexandrov NM, Lewis RM, Gumbert CR, Green LL, Newman PA (1999) Optimization with variable-fidelity models applied to wing design. Technical report, DTIC Document
23. Osorio C, Bierlaire M (2010) A simulation-based optimization framework for urban traffic control. Operations Research. (Cited on pages 146 and 153.)
24. Kirkpatrick S, Gelatt CD, Vecchi MP et al (1983) Optimization by simulated annealing. Science 220(4598):671–680
25. Nelder JA, Mead R (1965) A simplex method for function minimization. Comput J 7(4):308–313
26. Wales DJ, Doye JP (1997) Global optimization by basin-hopping and the lowest energy structures of lennard-jones clusters containing up to 110 atoms. J Phys Chem A 101(28):5111–5116
27. Garrich M, Bravalheri A, Magalhes M, Carvalho H, Assine J, Rusa H, Yamamura H, Hooft F, Moura U, Janurio J, Nascimento M, Mariote L, Oliveira J (2016) Pioneering hardware modeling and software design for optical infrastructure in the autonomous network project. In: 2016 international conference on optical network design and modeling (ONDM), pp 1–6, May 2016